

**Nano-indentation and Nano-scale imaging using
atomic force microscopy: from single cell to
single molecule**

DISSERTATION

Submitted in partial fulfillment of the requirements for the
degree of Doktor der Naturwissenschaften
(Dr. rer. nat.)

Orooba Al-Hammood

Faculty of Physics

University of Bielefeld

October 2020

Clarification

I hereby declare on oath that I have written this work by myself and have not used any aids other than those mentioned. I agree with the publication in the university library.

Bielefeld / Baghdad

Sig

(Orooba AL-Hammood)

This work was done under the supervision of Prof. Dr Dario Anselmetti in the workgroup Experimental Biophysics and Applied Nanosciences at the Department of Physics at Bielefeld University and Prof. Dr. rer. nat. Hendrik Milting in the workgroup Heart and Diabetes center North Rhine-Westphalia, Clinic for Thoracic and Cardiovascular Surgery Erich & Hanna Klessmann Institute for Cardiovascular Research and Development, Bad Oeyhausen.

1. Reviewer: Prof. Dr. Dario Anselmetti
2. Reviewer: Prof. Dr. Karsten Niehaus

Acknowledgements

Above all, I am really thankful to my God for blessings, sustenance, providence, protection, and patience during hard times.

First and foremost, I would like to extend my deepest gratitude to my supervisor Prof. Dr. Dario Anselmetti for giving me the opportunity to work on this research, he was always compassionate, knowledgeable, supportive person, and he provided me with endless guidance and helped in a difficult time. Thanks a lot for that!

I would like to extend my thanks, respect and appreciation to Dr. Volker Walhorn for his great efforts to explain things clearly and simply, and throughout my thesis writing period. He provided encouragement, sound advice, good teaching, good accompany, and lots of good ideas.

Also, I would like to express my deep thanks to Dr. KatjaTönsing, Dr. Martina Viefhues, for their help and support.

I sincerely appreciate and thank to the technician Christoph Pelargus and Helene Schellenberg for their support in all possible ways.

Special thanks to Prof. Dr. rer. nat. Hendrik Milting in the Erich and Hannah Klessmann institute for his many good ideas and valuable guidance. Also my deep thanks for Sandra Ratnavadivel and Daniela Baurichter in the Erich and Hannah Klessmann institute for providing human cell lines.

I am deeply thankful to Prof. Dr. Karsten Niehaus, Dr. Hanna Bednarz, and Dr. Tim Steffens in faculty of Biology, Proteome and Metabolome Research for sharing their experimental xanthan data, valuable guidance, and discussion.

It was great luck that I was one of PhD Students in the institute of biophysics and Nanoscience; I am grateful to all member of this institute for everything that they had introduced during my research's time, especially Niklas Biere, Kreft Dennis, Ahmad Humsi and Jenny Fiodorova. Also, graduate students: Dr. Mareike Dieding, Julia Teckentrup.

I sincerely acknowledge the financial support from the Iraqi Ministry of Higher Education and Scientific Research and Al-Nahrain University to cover my cost of living and also support some laboratory fees for this research project which helped me to stay focused.

I would like to thank my friends Dr. Ahamed Al-Hakak, Dr. Omer Abid Kathum, Dr. Mohanad Shukur, Mr. Ahmed Al-Zoubeidi, and Ms. Seba Baderkan for their never-ending support and encouragement which helped me overcome many difficulties.

Finally, I want to introduce special thanks to Germany, the beautiful country in which I lived, felt with safety and gained a lot of things that will help me to manage my future life.

Dedicated

To my father Mr. Nadhim Harbi AL-Hammood and my mother, Ms. Suad Mohammed the reason for my existence in this life, my success was a result of their pray & qualitative support. I spent hard moments without them, I ask God to bless them, and I hope that I will be the girl that they will be proud of.

To my precious diamonds; my brothers and sisters, who were and still are the reason for my happiness, success and pleasure in my life. It would be impossible for me to thank them for their innumerable sacrifices, on which I am standing today.

I dedicate this work.

OROoba

Thesis structure

This thesis included two different parts

1. The first part under the title: **Nano-Mechanical Characterization of ARVC Associated TMEM43 Mutation.**
2. The second part under the title: **Atomic Force Microscopy Study of the Xanthan Secondary Structure**

| Part 1 List of Contents | | |
|--|--|------|
| Index | Subjects | Page |
| | List of contents | V |
| | List of tables | VI |
| | List of figures | VII |
| | List of abbreviations | IX |
| Chapter one: Summary and Introduction | | |
| | Summary | 1 |
| 1.1 | Introduction | 3 |
| 1.1.1 | Atomic force microscopy | 3 |
| 1.1.1.1 | Atomic force microscope working principle | 3 |
| 1.1.1.2 | Operation modes of the AFM | 5 |
| A | Contact Mode | 5 |
| B | Non-contact mode (NC-AFM) | 6 |
| C | Tapping mode | 6 |
| D | AFM-based force spectroscopy | 7 |
| 1.1.2 | Cell elasticity quantification by AFM | 8 |
| 1.1.3 | Arrhythmogenic right ventricular cardiomyopathy (ARVC) | 9 |
| 1.1.4 | Transmembrane protein 43 | 10 |
| 1.1.5 | The mechanical properties of eukaryotic cell | 11 |
| 1.1.5.1 | The cell and nucleus structures | 11 |
| 1.1.5.2 | The cell and cytoplasm structures | 13 |
| 1.1.5.3 | The cell and endoplasmic reticulum(ER) structures | 15 |
| | The main objectives of this study | 16 |
| Part 1 Chapter two: Material and Methods | | |
| 1.2.1 | Cell lines | 17 |
| 1.2.2 | Sustaining cell lines | 17 |
| 1.2.3 | Prepare cell lines for the transfection process | 18 |
| 1.2.4 | Measurement samples | 19 |
| 1.2.4.1 | Estimation of elasticity in HeLa cell lines | 19 |

| | | |
|---|--|----|
| 1.2.4.2 | Induction of ER stress in HEK 293 cell lines | 19 |
| 1.2.4.3 | Estimation of elasticity in HEK 293 cell lines | 20 |
| 1.2.5 | AFM Techniques | 20 |
| 1.2.5.1 | AFM setup | 20 |
| 1.2.5.2 | AFM probe's selection | 21 |
| 1.2.5.3 | Calibration of cantilever spring constants | 22 |
| 1.2.6 | Elasticity Measurements | 24 |
| 1.2.6.1 | Force-indentation curves | 25 |
| 1.2.6.2 | Modeling of cells elasticity | 26 |
| 1.2.7 | Statistics | 27 |
| Chapter three: Results | | |
| 1.3.1 | TMEM43 mutation influences stiffness distributions of HeLa cell line | 28 |
| 1.3.2 | ER stress influences nucleus stiffness of HEK293 cell | 33 |
| 1.3.3 | Stiffness distributions of the fluorescent HEK293 cell lines | 39 |
| Part 1 Chapter four: Discussion | | |
| 1.4.1 | Effect of TMEM43 mutation on entire cell elasticity | 44 |
| 1.4.2 | ER stress affects cell nucleus elasticity | 46 |
| Part 1 Chapter five: Conclusions & Outlooks | | |
| 1.5.1 | Conclusions | 51 |
| 1.5.2 | Outlooks | 51 |
| Part 1 Chapter six: References | | |
| 1.6 | References | 52 |

| List of Tables | | |
|-----------------|---|------|
| No. | Titles | Page |
| 1-1 | Young's modulus measured by AFM on top of HeLa cell line transfected with wild-type (GFP-TMEM43-WT) and mutant (GFP-TMEM43-S358L). | 33 |
| 1-2 | Young's modulus measured by AFM on top of HEK293 cells treated with 0.1% and 0.25% volumes of pharmaceutical inducers. | 37 |
| 1-3 | Mann-Whitney U test results to compare nucleus stiffness of both volumes (0.1% and 0.25%) between DMSO. | 38 |
| 1-4 | Young's modulus measured by AFM on top of the transfected HEK293 cells. | 41 |
| 1-5 | Mann-Whitney U test results for a comparison of the stiffness of different cell types. | 43 |
| List of Figures | | |
| No. | Titles | Page |
| 1-1 | Schematic illustration of an atomic force microscope connected to a computer. | 4 |
| 1-2 | The path of the AFM cantilever raster scanning the tip across a sample surface in, (A) contact mode, (B) non-contact mode and (C) tapping mode | 5 |
| 1-3 | (A) The diagram displays indentation of a soft substrate by an AFM tip of the cantilever. (B) The indentation distance into the sample (δ) by subtracting the cantilever deflection (d) from the piezo-displacement | 9 |
| 1-4 | Structure of a eukaryotic cell | 11 |
| 1-5 | Represents the LINC complex in cardiomyocyte | 13 |
| 1-6 | Fluorescent microscopy images of the cells | 17 |
| 1-7 | Diagram transfection protocol in eukaryotic cells | 19 |
| 1-8 | The image illustrates the AFM setup | 21 |
| 1-9 | Images of silicon nitride DNP10 | 22 |
| 1-10 | The curve appears thermal tune of a contact mode cantilever in the liquid environment. | 24 |
| 1-11 | A diagram explains the typical force-distance curve | 26 |
| 1-12 | Typical force curve obtained from living cells | 28 |
| 1-13 | Elasticity map (A) corresponding topography of (GFP-TMEM43-WT) transfected HeLa cell line (B), Optical fluorescence image (C) and bright-field optical image of the cell (D). Force curve velocity 3.00 $\mu\text{m/s}$, force curve rate 1.5 Hz, 64 pixel \times 64 force curves. Data acquisition time was 60 min. The arrows indicate nucleus (N) and | 29 |

| | | |
|---------------------------|--|-----------------|
| | cytoplasm(C). | |
| 1-14 | Elasticity map (E) corresponding topography (GFP-TMEM43-S358L) transfected HeLa cell line (F), Optical fluorescence image (G) and bright-field optical image of the cell shown in (K). | 30 |
| 1-15 | Histograms represent effects on the elasticity modulus of transfected HeLa cells. | 31 |
| 1-16 | Histograms represent affects TMEM43-S358L on the elasticity modulus of the nuclear zone of transfected HeLa cells. | 31 |
| 1-17 | Histograms represent effects on the elasticity modulus of the cytoplasm area in transfected HeLa cells. | 32 |
| 1-18 | The box plots provide the average median values for elastic responses at different areas of wild-type (GFP-TMEM43-WT) and mutant (GFP-TMEM43-S358L) transfected HeLa cell line. | 33 |
| 1-19 | AFM images of HEK293 cells treated with (Thapsigargin), (Tunicamycin) and (DMSO). | 35 |
| 1-20 | The histograms represent effects doses of Pharmaceutical inducers on the elasticity modulus of the nuclear zone of HEK293 cells. | 36 |
| 1-21 | Box plot represents elastic responses of the nuclear area of HEK293 cells following treatment with a low volume of 0.1% Thapsigargin and Tunicamycin and compare them with DMSO. | 38 |
| 1-22 | Box plot of elastic responses of the nuclear zone of HEK293 cells following treatment with a high volume of 0.25% of Thapsigargin and Tunicamycin comparing them with DMSO. | 39 |
| 1-23 | AFM images of HEK293 cells transfected with (TMEM43-S358L), (TMEM43-WT) and (WT- without TMEM43). | 40 |
| 1-24 | The histograms present the elasticity distributions of the nuclear area in the fluorescent HEK293 cell line. | 41 |
| 1-25 | Box plots of the elastic responses of the nuclear area of GFP-TMEM43-p.S358L HEK293 cells. | 42 |
| List Abbreviations | | |
| 1. | Transforming growth factor | (TGF) β 3 |
| 2. | Atomic force microscopy | AFM |
| 3. | AFM-based force spectroscopy | AFM-FS |
| 4. | Arrhythmogenic right ventricular cardiomyopathy | ARVC |
| 5. | Arrhythmogenic right ventricular cardiomyopathy5 | ARVC5 |
| 6. | Activating transcription factor 6 | ATF6 |
| 7. | Immunoglobulin binding protein | BiP |
| 8. | dilated cardiomyopathy | CDM |
| 9. | The C/EBP homologous protein | CHOP |
| 10. | Contact mode | CM-AFM |
| 11. | The cytoskeleton | CSK |

| | | |
|-----|---|--------------|
| 12. | Young's modulus | E_{Hertz} |
| 13. | The extracellular matrix | ECM |
| 14. | Emery-Dreifuss muscular dystrophy | EDMD |
| 15. | The endoplasmic reticulum | ER |
| 16. | Endoplasmic reticulum stress | ERS |
| 17. | actin filaments | F-actin |
| 18. | Intermediate filaments | IF-s |
| 19. | The inner nuclear membrane | INM |
| 20. | Inositol-requiring protein-1 | IRE1 |
| 21. | the linker of nucleoskeleton and cytoskeleton | LINC |
| 22. | Molecular recognition mapping | MRM |
| 23. | Microtubules | MT-s |
| 24. | Non- Contact mode | NC-AFM |
| 25. | The nuclear envelope | NE |
| 26. | The nuclear pore complexes | NPC |
| 27. | The outer nuclear membrane | ONM |
| 28. | PKR-like ER kinase | PERKS |
| 29. | Position sensitive photodetector | PSPD |
| 30. | Human ryanodine receptor | RyR2 |
| 31. | Sudden cardiac death | SCD |
| 32. | Single-cell force spectroscopy | SCFS |
| 33. | Single-molecule force spectroscopy | SMFS |
| 34. | Scanning probe microscopes | SPMs |
| 35. | Thapsigargin | TG |
| 36. | Transforming growth factor- β | TGF- β |
| 37. | Tapping mode | TM-AFM |
| 38. | Transmembrane protein43 | TMEM43 |
| 39. | Tunicamycin | TUN |
| 40. | unfolded protein response | UPR |
| 41. | Ethylenediaminetera acetic acid | EDTA |
| 42. | Dimethyl sulfoxide | DMSO |

| Part 2 List of Contents | | |
|---------------------------------------|-----------------------------------|------|
| Index | Subjects | Page |
| | List of contents | X |
| | List of tables | XI |
| | List of figures | XII |
| | List of abbreviations | XII |
| Chapter one: Summary and Introduction | | |
| | Summary | 70 |
| 2.1 | Introduction | 71 |
| 2.1.1 | Xanthan gum | 71 |
| 2.1.1.1 | History | 71 |
| 2.1.1.2 | Production of Xanthan Gum | 71 |
| A | Xanthomons (<i>campestris</i>) | 71 |
| B | Biosynthesis of Xanthan Gum | 72 |
| C | Commercial Production Process | 74 |
| 2.1.2 | Chemical structure of xanthan gum | 75 |
| 2.1.3 | Properties of Xanthan Solutions | 76 |
| 2.1.4 | Applications of Xanthan gum | 78 |
| | The main objective of this study | 79 |
| Chapter two: Material and Methods | | |
| 2.2.1 | Xanthan samples | 80 |
| 2.2.2 | measurements samples | 80 |
| 2.2.3 | AFM experiments | 81 |
| 2.2.3.1 | AFM setup | 81 |
| 2.2.3.2 | Cantilevers | 82 |
| 2.2.3.3 | AFM measurements | 82 |
| 2.2.4 | Structural analysis | 83 |
| 2.2.5 | Viscosity measurements | 83 |
| 2.2.6 | Statistics | 84 |

| Chapter three: Results and Discussion | | |
|---------------------------------------|--|-----|
| 2.3.1 | Structure analysis of xanthan | 85 |
| 2.3.1.1 | Structures analysis of xanthan B100 and wxcB | 87 |
| 2.3.1.2 | Structure analysis of xanthan JBL007 | 90 |
| 2.3.1.3 | Structure analysis of acetate-free xanthan | 93 |
| 2.3.1.4 | Structure analysis of pyruvate-free xanthan | 95 |
| 2.3.2 | Specificity of secondary structures | 98 |
| 2.3.3 | Xanthan contour length distributions | 99 |
| 2.3.4 | Correlation between viscosity behavior and structure | 100 |
| Chapter four: Conclusion | | |
| 2.4 | Conclusion | 102 |
| Chapter five: References | | |
| 2.5.1 | References | 103 |
| | Curriculum Vita | 112 |

| List of tables | | |
|----------------|---|------|
| No. | Titles | Page |
| 2-1 | Overview of xanthan samples | 80 |
| 2-2 | Structural and viscosity data of all xanthan samples tested. | 86 |
| 2-3 | Structural and viscosity data of B100 and wxcB samples | 90 |
| 2-4 | Calculated p-values of the Mann-Whitney U-Test for the distributions of the mean heights between JBL007 and other tested samples | 92 |
| 2-5 | Calculated p-values of the Mann-Whitney U-Test for the distributions of the mean heights between Acetate-free xanthan and tested samples. | 95 |
| 2-6 | Calculated p-values of the Mann-Whitney U-Test for the distributions of the mean heights between pyruvate-free xanthan < 0.5 nm and other tested samples. | 97 |

| 2-7 | Calculated p-values of the Mann-Whitney U-Test for the distributions of the mean heights between pyruvate-free xanthan > 0.5 nm and other tested samples. | 97 |
|------------------------|---|------|
| List of Figures | | |
| No. | Titles | Page |
| 2-1 | Transmission electron microscope image of <i>X.campestris</i> | 72 |
| 2-2 | The biosynthesis process for xanthan gum at the inner membrane of <i>Xanthomonas campestris pv. campestris</i> (Xcc) | 73 |
| 2-3 | The steps of producing xanthan gum | 75 |
| 2-4 | The primary structure of xanthan | 76 |
| 2-5 | The image illustrates the AFM-Multimode 8 setup | 81 |
| 2-6 | The Tap300 Al-G monolithic silicon cantilevers | 82 |
| 2-7 | The AFM topography images shows <i>Xanthomonas campestris pv. campestris</i> B100 and wxcB. | 88 |
| 2-8 | The histograms represent the mean values of height of the wild type B100 and the mutant type wxcB samples. | 89 |
| 2-9 | Box plot represents the mean values of height of the B100 and (A, B, C, D) samples. | 90 |
| 2-10 | The AFM topography images show the production strain JBL007. | 91 |
| 2-11 | The histograms represent the mean values of height of the production strain JBL007. | 92 |
| 2-12 | The AFM topography images show of the Acetate-free xanthan. | 93 |
| 2-13 | The histograms represent the mean values of height of the Acetate-free xanthan. | 94 |
| 2-14 | The AFM topography images under an ambient condition show the Pyruvate-free xanthan. | 96 |
| 2-15 | Boxplots of the measured heights [nm] of the different xanthan sample | 99 |
| 2-16 | Boxplots of the measured contour lengths [nm] of the different xanthan samples | 100 |

| List Abbreviations | | |
|--------------------|--|----------------|
| 1. | <i>Xanthomonas campestris</i> | Xcc |
| 2. | Mutant xanthan strain Xcc H21012 | wxcB |
| 3. | Wild type xanthan strain | B100 |
| 4. | Industrial production strain | JBL007 |
| 5. | National Center of the United States Department of Agriculture | USDA |
| 6. | The United States Food and Drug Administration | FDA |
| 7. | Contour length | L _C |
| 8. | Persistence length | L _P |

Summary

TMEM43 is a protein embedded inside the inner nuclear envelope and cytoplasm, which is related to the LINC (linker of nucleoskeleton and cytoskeleton) complex. Studies indicate that the Ser358Leu mutation in the TMEM43 gene lead to arrhythmogenic right ventricular cardiomyopathy type V (ARVC-5) is a distinct form of ARVC, but information about the molecular mechanisms of evolution of these diseases are still limited. Understanding how the Ser358Leu mutation affects the mechanical properties of the nucleus and as a whole in a transfect HeLa cell model may give new insights into the potential molecular mechanisms of these diseases. By using the AFM force spectroscopy mode, the elasticity of the nuclear region and cytoplasm region under native conditions were measured. By means of the Hertz model, the force curve data were analyzed. We found the HeLa cell carrying GFP-TMEM43-pS358L showed a noticeable increase in Young modulus in the nucleus and cytoplasm compared to GFP-TMEM43-WT. Here, our results strongly suggest that the impact of the TMEM43 mutation is not limited to nuclear mechanics but extends to the entire cell.

The endoplasmic reticulum (ER) plays an exceptional role in the folding and maturation of newly synthesized secretory and transmembrane proteins, and maintaining calcium homeostasis. The ER stress is the accumulation of misfolded proteins at the ER, resulting in unfolded protein response (UPR). In this study, we were focused on two-ways. (1) To characterize whether disorder cellular homeostasis that causes ERS is affected the mechanical properties of the nucleus. (2) To create a new control to understand the pathological mechanisms of ARVC5 disease. To accomplish the first goal, the treated HEK293 cell line with two different volumes 0.1% and 0.25% of with pharmacological agents the thapsigargin and tunicamycin, which is a standardized model to induce ER stress were used. After the data analysis, our results revealed a significant increase Young's modulus in the nucleus compared with control (DMSO) volumes a significant increase in Young's modulus in the nucleus compared with control (DMSO) volumes. Here, these results proved that the disorder cellular homeostasis produces dynamic feedback between intracellular and extracellular environments, resulting in a change in the biophysical activity of cells. As for the second aim, the transfected HEK293 GFP-TMEM43-S358L, GFP-TMEM43-WT, and GFP-without TMEM43 were used. The GFP-TMEM43-S358L cells exhibited significantly different stiffness values than the nuclear zone of the transfected HEK293

cell (GFP-TMEM43-WT) and (GFP-WT-without TMEM43) cells. In briefly, the pS358L mutation in the TMEM43 gene affects the structure of physical connections in and cell stimulates a cellular stress response, apoptosis and thus cell death.

1.1 Introduction

1.1.1 Atomic force microscopy

The atomic force microscope (AFM) is a unique and valuable tool which is utilized in the probing of different sample surfaces at nanometer-scale spatial resolution (Jazvinščak Jembrek et al. 2015). It belongs to the family of microscopes that are called scanning probe microscopes (SPMs). The first SPMs were developed in the mid-nineteen eighties by Binnig and Rohrer. Later on, the AFM was developed in 1986 (Binnig et al. 1986). In electron microscopy, high-resolution images are obtained by a thin conductive layer on the surface of the specimen which should be completed under vacuum. But, this method of preparation is not suitable for biological samples (Binnig et al. 1982; Binnig et al. 1986). On the contrary, AFM does not need a conductive coating for the imaging of samples and high-resolution imaging of biological structures. AFM image gives an accurate 3D representation of real space (Stylianou et al. 2019). Interestingly, in the last years; scientists had been recorded a remarkable evolution in the ability of the AFM to quantify interactions between the tip and a region of interest (Wang et al. 2011).

The force microscopy method permits the measurement of inter- and intramolecular forces interaction forces desired to detach the tip from the region of interest, with piconewton resolution (Marrese et al. 2017). Thus, the AFM introduces an accurate description to analyze the morphological and mechanical properties of biopolymer, natural and cancer cells at high resolution in nanometer spatial resolution; these properties contributed to the clarification of many biological and biomedical issues and to provide a suitable explanation for dynamic processes, such as nano-structural changes that are caused by natural growth or medication interactions (Stylianou et al. 2019). On the other hand, these properties had a fundamental correlation with cells' fate and pathophysiological state that will serve in the development of novel diagnostic strategies (Gendelman et al. 2014).

1.1.1.1 Atomic force microscope working principle

The atomic force microscope consists of four main parts (Fig.1-1); the cantilever is made of silicon or silicon nitride, with a sharp tip mounted at the end of the probe, piezo-scanner that controls the position and height of the cantilever, the laser diode and the position-sensitive photo-detector (PSPD) (Aliano et al. 2012). When the tip of the cantilever scans above the surfaces of the biological specimen, the attractive force

between the tip and the features on the surface of the biological specimen causes the cantilever to deflect to the surface, this deflection can be measured by detecting the position of a laser beam that reflects from the free end of the cantilever into quadrant photodiode, whose output signal is collected by a differential amplifier (Gavara 2017). At the same time, a piezoelectric scanner allows a high-resolution positioning in three dimensions of the tip, with nanometer accuracy in the feedback loop that controls the height of the tip over the surface. The feedback loop mechanism acts by monitoring the voltage related to the deflection of the cantilever on the surface and adjusts the Z-piezoelectric subsequently to keep the set point of deflection as described by the user (Gavara 2017). Here, if there is any change in surface topography, the AFM is able to react quickly in maintaining a constant force; thus, decreasing of the sample's damage and preserving tip's sharpness for longer. The design of the AFM helped to obtain an atomic resolution of images for many different surfaces. Moreover, the AFM is able to work with biological samples under their physiological conditions, whether in ambient environments or in liquid solutions (Miller et al. 2016). Thus, the biological samples such as cells can be kept at suitable temperatures in nutrient buffers, even at recommended CO₂ concentrations in which, they kept alive during measurements (Chang et al. 2012).

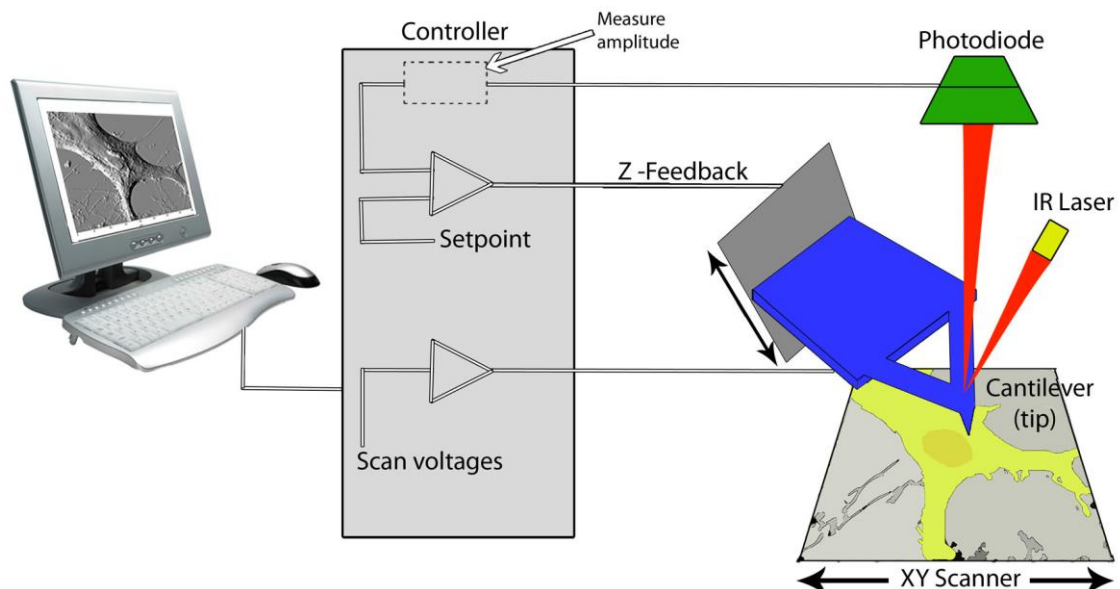


Figure 1-1: Schematic illustration of an atomic force microscope connected to a computer (Taatjes et al. 2013).

1.1.1.2 Operation modes of the AFM

The AFM has different imaging modes that are mainly dependent on how the tip moves over the sample (Duf r ne et al. 2017). It is as follows:

A. Contact Mode

The first AFM imaging mode developed was contact mode (CM-AFM). The basic principle of this mode depends on the forces applied by the AFM on the sample where the interaction between the sharp tip of the cantilever and the sample surface is repulsive (Fig. 1-2A). Here, the tip height is permanently adjusted to preserve a constant deflection (Allison et al. 2010; Dombrowski 2013). A topography image is generated to check the area of interest in the sample by the voltage applied on the piezo during the faster scan. Contact mode is used in different environmental conditions such as liquid, gaseous and ambient. Under ambient conditions, the work of the AFM is occasionally difficult due to the existence of moisture that causes capillary forces between the cantilever tip and sample surface. These forces raise the interaction force between the sample and the tip of the cantilever; thus, interfering with the scanning process. The effect can be manipulated by reducing the tracking force between the tip and sample (Duf r ne et al. 2017; Guo et al. 2013). This is done either by scanning in liquids or in ultrahigh vacuum.

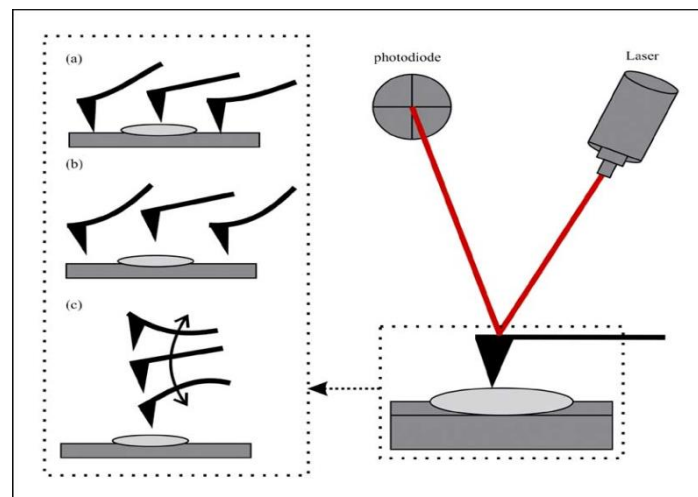


Figure 1-2: The path of the AFM cantilever raster scanning the tip across a sample surface in, (A) contact mode, (B) non-contact mode and (C) tapping mode (Veerapandian and Yun 2009).

B. Non-contact mode (NC-AFM)

NC-AFM is one of the newly developed techniques to improve the performance of atomic force microscope that was developed by Martin et al. 1987, in this mode, the oscillating tip is brought closer to the specimen and begin to tap to the surface of the specimen (Fig. 1-2 B). Unlike the tapping mode, the oscillating tip never touches the surface of the specimen. During scanning, the amplitude of the oscillation can be changed due to attractive van der Waals forces that are acting between the tip and the specimen where these forces are quite small in comparison with the repulsive forces of contact modes (Piner et al. 1999). This small force is beneficial for the study of soft samples such as biological cells in addition; it does not let the surface to be contaminated due to the contact with the tip (Ho and West 1996; Proksch 2006).

C. Tapping mode

The tapping mode (TM-AFM) is known as an oscillation of cantilever's tip-in intermittent contact at the surface of the sample with high amplitude (> 20 nm) (Putman et al. 1994). Therefore, tapping mode is an appropriate method for softer or loosely adsorbed samples more than contact mode. This can lead to deforming of the sample due to the lateral shear forces as well as; it reduces drag between the tip and the sample. This helps to beat the problems associated with adhesion, friction and electrostatic forces (Zitzler et al. 2002; Cleveland et al. 1998). During scanning, the vertically oscillating tip moves toward the sample's surface until it touches or taps the surface briefly thus; leading to a reduction in oscillation amplitude (Fig.1-2 C). This reduction in the amplitude is used for determining and measuring surface features of the sample. The feedback signals adjust the vertical position of the piezoelectric scanner to preserve a constant set-point oscillation amplitude of the tip of the cantilever and thus, constant applied force.

As in contact mode, the adjustments in the vertical position of the piezoelectric scanner are recorded; then, the information will be used to produce high-resolution topographical, amplitude, and phase images. In the liquid environment, tapping mode is a very useful tool for scanning of biological samples such as; cells which are soft in their living conditions as in vivo environment when it compared to dehydrated samples (Vahabi et al. 2013)

D. AFM-based force spectroscopy

AFM force spectroscopy (AFM-FS) is one of the most important AFM mechanisms that complete the micro and nanoscale topographical detail presented by imaging (Ruggeri et al. 2019). As well as, it's the capability to measure the mechanical properties of biological samples under near-physiological condition (Scholl and Marszalek 2018). In particular, force spectroscopy gives vital mechanical information on interesting regions in living cells at high spatial resolution. Currently, quantitative study for nanomechanical properties of cells and tissues, including the elasticity of the cells have a considerable biomedical interest because, some cellular demeanor such as motility, proliferation, differentiation, and aging can appear themselves as changes in the elasticity (Guck et al. 2005; Kumar and Weaver 2009). In this technique, the tip-sample interaction forces are immediately measured as a function of the cantilever deflection. The x and y position of the AFM tip stay static while in the z-direction the tip is driven into repulsive contact with a surface of the specimen and then retracted. The deflection of the AFM tip is spotted as a function of piezoelectric displacement. In one cycle, the tracing and retracting of the specimen are produced what called force-distance curves, which will be explained in detail in the chapter material and methods. The force vs. distance curve is a plot of the deflection of the cantilever versus the extension of the piezoelectric scanner that changes the distance between the specimen and the AFM tip (Ciavarella et al. 2019). These measurements are utilized to acquire nanoscale contacts, van der Waals forces, atomic bonding and single-molecule stretching and rupture forces. Specifically, when the AFM tip is closed to the specimen's surface, in this case; the force should be strong enough to tear the surface of the specimen. The whole process is recognized as leaping in the force curve; the force of specimen surface rupture depends on the depth of the jump that corresponds to specimen thickness, and the force required fracturing of the specimen. Statistically, it is requisite to gather many force-distance curves that are measured at each point on the certain surface area, therefore obtaining a pertinent histogram of the yield threshold forces. AFM force spectroscopy mode consists of several types: Single-molecule force spectroscopy (SMFS), Molecular recognition mapping (MRM) and Single-cell force spectroscopy (SCFS) (Müller et al. 2009). In this work, we focused on experiments that help us to get the mechanical properties of cells using force spectroscopy. Here, the tip of the cantilever is moved to interesting areas of the samples, and Young's modulus is

acquired from the resulting force-distance curves through the application of a mathematical model. It is essential to know applied force, tip geometry and spring constant of the cantilever. Force mapping is a technique which takes advantage of high spatial resolution offered by force spectroscopy; it involves performing of multiple identical force-indentation curves covering the surface of the sample, in the process building a map based on the recorded stiffness values (Jeon et al. 2013).

1.1.2 Cell's elasticity quantification by AFM

Young's modulus (E) is known as the relation between stress and strain of a solid material (often referred to as the material's elasticity with the unit of Pascals). The Young's modulus of living cells differs significantly depending on cell types and mechanism available to measure it. The main reason for this is those elasticity measurements completed by the AFM are based on Hooke's law which proves that the ratio of the stress to the strain equals a constant depending on materials and deformation (Vinckier and Semenza 1998). So, this state that the spring extension (in this case represented the cantilever) is directly proportional to the strain applied to it. This case is suitable for linearly elastic materials. Therefore, choosing an appropriate mathematical application is necessary. For this reason, it is fundamental to unify the method of extraction in Young's modulus from the initial force-distance curve (explain in detail in the chapter method and material section).

Hooke's law is represented by the following equation:

$$\mathbf{F} = -\mathbf{k}\mathbf{d}$$

Where \mathbf{F} is the restorative force exerted by the cantilever, \mathbf{k} is AFM cantilever spring constant and \mathbf{d} is the size of the cantilever deflection. In order to calculate cellular Young's modulus, a force-indentation curve has to be derived from the general force-distance curves that are usually measured on the stiff and compliant surfaces. In the stiff surfaces such as glass, the straight-sloped line applied as a reference line required for force's calibration. In cells that are considered as compatible samples, the force curve exhibits a nonlinear character according to the elastic properties of the cell and the shape of the intending probe (Thomas et al. 2013). In an indentation measurement, the tip of the cantilever rushes towards the cell (z), the force-distance curve consists both of the indentations of the sample (δ) and the cantilever deflection (d , $d = -F/k$) (Fig.1-3). To evaluate the indentation depth of the sample (δ) by subtracting the cantilever

deflection (d) from the piezo-displacement, it is very important to get a force-distance curve on the hard substance such as the glass bottom of the petri dish (Gavara 2017).

There are several models which are suitable for the evaluation of elasticity which can be used in combination with force-indentation curves resulted from AFM scanning. Software like Matlab and origin lab fit the mechanical models of experimental data. In Young's modulus, E can be derived from using these equations by different methods. The most common models used are Hertz-Sneddon, Johnson-Kendall-Robins, and Derjaguin-Muller-Toporov models (Guz et al. 2014).

In our project, the Hertzian theory of elastic contact has been used to assess the elastic properties of cells from force-indentation curves. This model was discussed in chapter material and methods

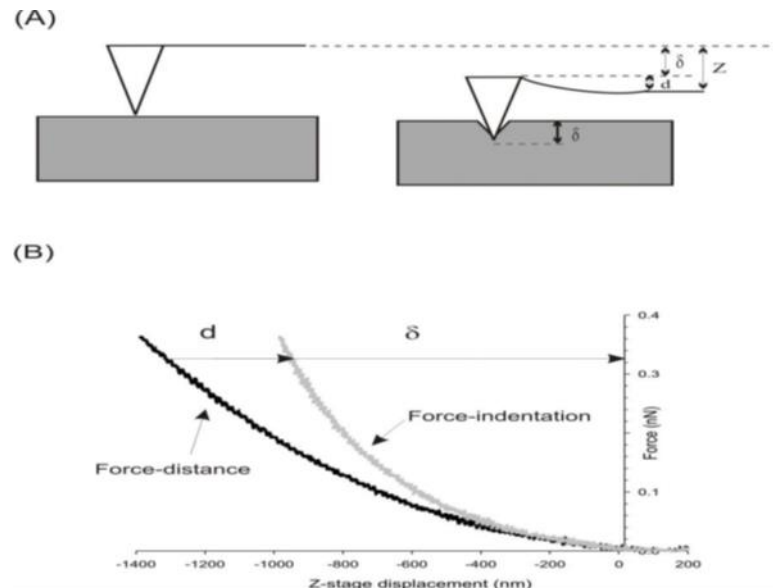


Figure 1-3: (A) The diagram displays indentation of a soft substrate by an AFM tip of the cantilever. (B) The indentation distance into the sample (δ) by subtracting the cantilever deflection (d) from the piezo-displacement (Bowen and Hilal 2009).

1.1.3 Arrhythmogenic right ventricular cardiomyopathy (ARVC):

Frank et al. (1978) was the first who described arrhythmogenic right ventricular cardiomyopathy (ARVC). It is well known as a heart muscle disease which is characterized by a high incidence of life-threatening arrhythmias, fibrofatty replacement of the ventricular myocardium (Pilichou et al. 2016). This leads to palpitations at an early stage, ventricular tachycardia or syncope before sudden cardiac death occurs. The ratio can be about 20% of sudden cardiac death (SCD) cases in young individuals and athletes in Europe. The prevalence of ARVC is estimated to be 1:1000-1:5000

(Srinivasan and Schilling 2018). The SCD is one of the main signs of ARVC (Marcus and Abidov 2012). Currently, most genes which have been identified for these disorders were encoded as desmosomal, sarcomeric, cytoskeletal, and nuclear envelope proteins (McCauley and Wehrens 2009). It is well known that the predominant causes of arrhythmogenic cardiomyopathy are the mutations in genes that encode components of desmosomes. The desmosomes are cell adhesion junctions that particularly abundant in tissues subjected to a high amount of mechanical stress like; heart and skin. Disease-associated with these genes have been estimated in 30-50% of ARVC cases in various infected groups worldwide (Al-Jassar et al. 2013). In addition, the non-desmosomal genes encoding for transforming growth factor (TGF) β 3, human ryanodine receptor (RyR) 2 and the transmembrane protein TMEM43, are also involved under ARVC disease (Herren et al. 2009). In recent years, there were integrative studies of the TMEM43 mutation in order to understand the mechanistic of the molecular pathogenesis of ARVC5.

1.1.4 Transmembrane protein 43

The transmembrane protein 43 (TMEM43) is also called LUMA; generally, is speculated to be a transmembrane protein of the nuclear envelope membrane and it is localized outside the nucleus (Siragam et al. 2014). It is a 43 kDa putative membrane protein of uncertain structure and function and encoded by the TMEM43 gene (Rajkumar et al. 2012; Siragam et al. 2014). In the third TM domain of TMEM43 protein, a single amino acid is replaced the serine 358 with leucine (S358L). The TMEM43 S358L mutation was first recognized in a founder population on the island of Newfoundland in Canadian (Baskin et al. 2013). So, this mutation is undoubtedly an obvious cause of the (ARVC5) diseases. However, the underlying molecular mechanism(s) behind the pathogenesis of ARVC5 is still not understood (Milting et al. 2015). The TMEM43 gene has sequences consistent with a response element for the adipogenic transcription factor PPAR gamma, which may explain the fibrofatty replacement of the myocardium in ARVC (Merner et al. 2008). It is broadly expressed in human tissues, and significantly, it has been appeared to be expressed in the heart (Stroud et al. 2014). On the other hand, the current research confirmed that the TMEM43 protein binds to several structural proteins such as emerin, lamin A/C, SUN2, and β -actin. So, it is an obvious part of the LINC (linker of nucleoskeleton and

cytoskeleton) (Stroud 2018; Padrón-Barthe et al. 2019). The LINC complex plays an exceptional role in supporting the nucleus architecture, where it connects the inner nucleoskeletal lamin A/C network with the cytoplasmic cytoskeleton (Stroud et al. 2014). Thus, these connections provide a mechanism for guiding of the mechanotransduction inside the cell, in order to adapt cellular mechanosensitivity (Jaalouk and Lammerding 2009).

1.1.5 The mechanical properties of eukaryotic cell

The eukaryotic cells possess a highly complex and compact environment (fig. 4). The intracellular environment plays a considerable role in resisting the impact of mechanical forces such as active contraction produced via neighbouring cells or resist by the extracellular matrix (ECM) (Pegoraro et al. 2017). This part will present a brief description of the cellular structures that determine the mechanical properties of cells.

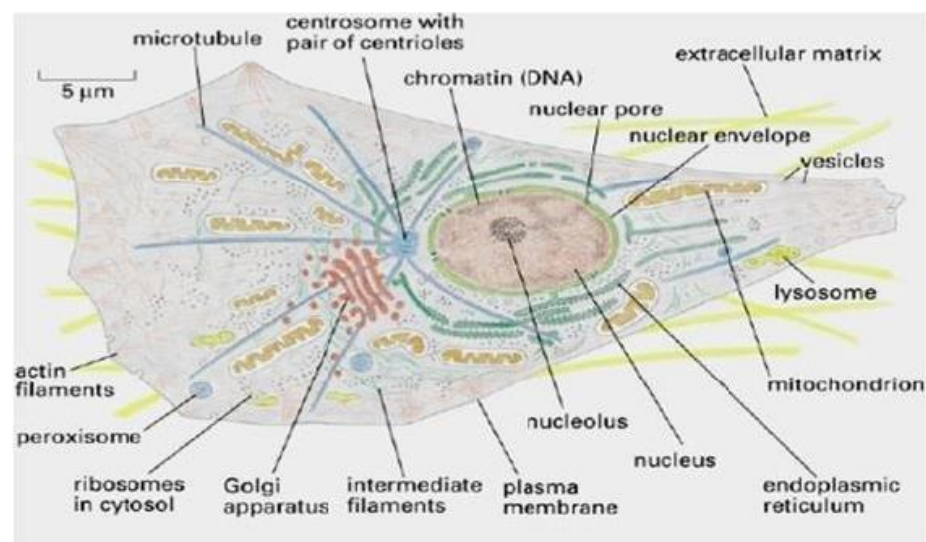


Figure1-4: Structure of a eukaryotic cell (Albert et al. 2003).

1.1.5.1 The cell and nucleus structures

The largest organelle in eukaryotic cells is the nucleus which contains genetic material and transcriptional machinery; their diameters vary depending on the type of cell ranging from 5-20 μm (Zwerger et al. 2011). Structurally, the nucleus consists of two regions; the first region, the nuclear interior contains chromatin (made of histone proteins and DNA, which are negatively charged polyelectrolytes) as a major component of the nuclear architecture; it plays a distinct role in determining the mechanical properties of the nucleus (Bártová et al. 2008). While the second region, the

nuclear contents are delimited by a double membrane called the nuclear envelope (NE). It separates the cell's genetic material from the cytoplasm and consists of two distinct membranes; the outer nuclear membrane (ONM) and inner nuclear membrane (INM) (Fernandez-Martinez and Rout 2009). Both are bounded together by nuclear pore complexes (NPC), but their protein content is various (Guo and Fang, 2014). The nuclear lamina lies in the INM, while the ONM is contiguous with the membrane system of the ER (Starr 2007). It is well known that the nuclear lamina is a meshwork of proteins; consist of type V intermediate, including lamins A and B and lamina-associating proteins. Lamins A including the somatic lamins A and C, it has a fundamental structural role in mechanical properties of the nucleus (Dechat et al. 2010). Stiffness conferred by type (A) lamins is important for nuclear mechanotransduction. Also, they can be found in the interior part of the nucleus, where they form stable structures (Osmanagic-Myers et al. 2015), while type B lamins (lamins B1 and B2) are responsible for the anchoring of the nucleus in the cytoskeleton, and the transmission of forces from in and to outside of the nucleus (Lee et al. 2014). On the other hand, the lamina is related to the cytoskeleton via the LINC complex (fig 5) (Stroud 2018). Hence, being a mediator of dynamic links between the cytoskeleton and chromatin; the lamins have a distinct role in the regulatory processes that occur between the cytoplasm and the nucleoplasm. Over the past two decades, the nuclear composition and organization have gained mounting importance as many mutations in lamins A/C, and other nuclear envelope proteins such as emerin and TMEM43 protein were specified as causing a bewildering number of diseases, among them Emery-Dreifuss muscular dystrophy (EDMD) (Bianchi et al. 2018), dilated cardiomyopathy (CDM) (Sciatti et al. 2018) and arrhythmogenic right ventricular dysplasia (ARVD5) (Milting et al. 2015). Recent data have proven that these mutations cause mechanical stress that leads to a nuclear mechanics disorder, therefore modulating of nuclear elasticity (stiffness/softness), and signalling mechanotransduction. Moreover, these mutations also activate signalling pathways and abnormal control of gene expression (Hu et al. 2018). Together, all of these studies proved that the changes in nuclear structure and composition are highly related to the pathogenic evolution of these diseases.

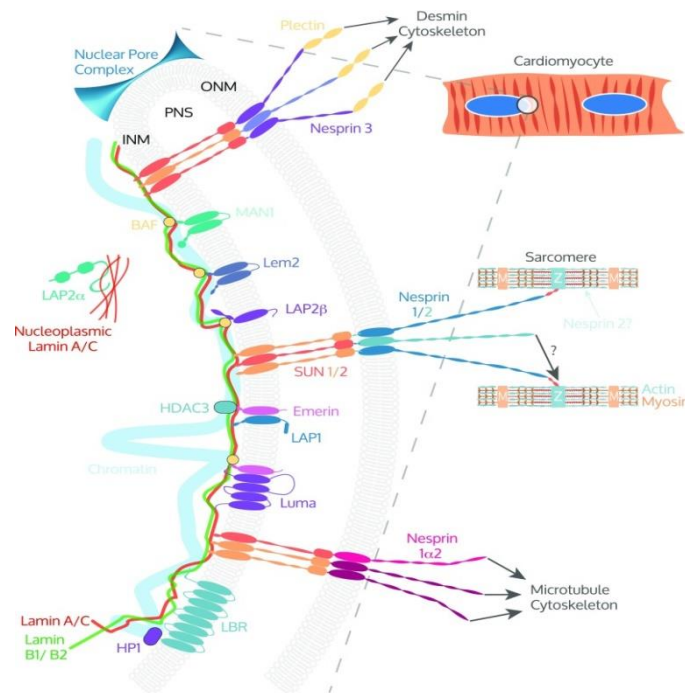


Figure (1-5) the LINC complex in cardiomyocyte

Cardiac myocyte nuclei (blue) in the circled region explaining the nuclear envelope (NE) and the linker between nucleoskeleton and cytoskeleton (LINC) complex. The interaction of SUN1 and SUN2 in the inner nuclear membrane (INM) that interact via their SUN domain with the KASH domain of the Nesprins that reside in the outer nuclear membrane (ONM). The NE links to sarcomere by interacting with the Z-disk (Z) or indirectly through intermediate binding partners(s) via giant isoforms of Nesprins 1 and 2 the Nesprin. The interaction of Nesprin 1 α 2 with kinesin 1, takes place by linking the NE to the microtubule cytoskeleton and indirect link of Nesprin 3 to the desmin intermediate filaments through plectin. Large numbers of proteins are found to be connected with the LINC complex which can interact with lamins or SUN proteins including LAP2 α , Emerin, MAN1, LEM2, Luma, and LAPI and have been established to play an important effect in cardiomyocytes (Stroud 2018).

1.1.5.2 The cell and cytoplasm structures

Cell mechanics have a major role in many biological functions of eukaryotic cells (Fletcher and Mullins 2010). The cytoskeleton (CSK) is the main component of cytoplasm in the form of a contractile filamentous meshwork that extend the whole cell (Gardel et al. 2008). It is well known the cytoskeleton consists of three families of proteins, which gather to take the shape of three main types of filaments: actin filaments (F-actin), intermediate filaments (IF-s), and microtubules (MT-s) (Guo et al. 2013). Although, the mechanical connection between the nucleus, microfilaments of the cytoskeleton, and cell membrane, the biomechanical activity and information transmitted between those structures are still inconspicuous (Frieden and Gatenby 2019). Many experiences proved that both F-actin and the MT-s under compression

could appear integrated mechanical behaviours. Where, the actin filaments exert stress, while microtubules resist compression loads (Manificier et al. 2016). Therefore, the cytoskeleton can be viewed as a tension structure due to tension produced by actin stress fibers, which is the basis for primary and dominant force-generating in the cell (Burrige and Guilly 2016). Actin filaments are defined as monomeric (G-actin) proteins that polymerized to assemble long polar microfilaments (F-actin) with structurally distinctive ends, denoted as the "barbed" end and the "pointed" (Svitkina 2018). In addition, the actin filaments are bound with fibrous bundles of myosin (motor protein) to form contractile structures in cells. The actin-myosin interactions are indicated in the muscle cells by "myofibrils", while in non-muscle cells, they are named "stress fibers" (Akhmanova et al. 2005). The fiber stress (SF) plays a prominent role in organizing of many cellular processes, including movements, cellular mechanotransduction, and apoptosis (Svitkina 2018). Indeed, Actin-myosin interactions have a crucial role for many types of cell movements. The myosin acts as a molecular motor to convert the energy resulting from the adenosine triphosphate (ATP) hydrolysis to mechanical energy, which leads to force generation and movement (Pertici et al. 2018). In more detail, the SF is classified into four various subtypes: ventral stress fibers, dorsal fibers, transverse actin arcs, and perinuclear actin fibers (Maninová and Vomastek 2016). These subtypes form three-dimensional structure are confined by the ventral side of the cell (Tanja Mierke 2017). All of these subtypes, except transverse arcs, are anchored to the extracellular matrix through focal adhesion, which is transmembrane proteins spot-weld such as integrin receptors (Lee and Kumar 2016). In contrast, the perinuclear actin fibers span above the nucleus attached to the nucleus and nuclear envelope via LINC (linker of nucleoskeleton and cytoskeleton) complex (Maninová and Vomastek 2016). Thus, these connections allow the transmission of mechanical cues from intra-and extra-cellular environments by integrin's receptor. These signals are translated into biochemical input through integrin-related signaling pathways. This results in a complex mechanotransduction system for regulating nuclear orientation (Tanja Mierke 2017). On the other hand, the response of cells to remodeling of the ECM microenvironments has a major role in cell behavior. For instance, ECM stiffening in disease states such as fibrosis, which is a prevalent characteristic of ARVD/C diseases (Uitto and Kouba 2000).

1.1.5.3 The cell and endoplasmic reticulum(ER) structures

The endoplasmic reticulum (ER) is one of the most important and largest organelles in eukaryotic cells; it plays a substantial role in calcium storage, translocation of proteins across the membrane, integration of proteins into membrane and lipid synthesis (Schwarz and Blower 2016). Indeed, the ER participates to the output and folding of approximately 30% of cellular proteins. Consequently, it is closely related to the conservation of homeostasis of the cell (Yalcin and Hotamisligil 2013). The disturbance cellular homeostasis may generate dynamic feedback between intracellular and extracellular environments, which relies on biophysical cues responsible for regulating critical cellular behaviors (Cheng et al. 2017). Newly, accumulating evidence indicates that abnormal folding and accumulation of nuclear envelope proteins might cause confusion of ER homeostasis, thus stimulating the ER stress (Buchwalter et al. 2019; Carmosino et al. 2016). This leads to incitement of a range of nuclear envelopathies diseases (Janin et al. 2017). For example, several studies linked ER stress to mutations in lamin A/C and emerin that cause of the DCM and the EDMD respectively (Carmosino et al. 2016; West et al. 2016; Essawy et al. 2019). As previously mentioned, these lamin A/C and emerin proteins form a complex configuration with TMEM43 protein. So, TMEM43 mutation might share common features with the envelopathies diseases. A lot of research showed that the TMEM43 mutation is able to mislocalize either emerin or well-known TMEM43 protein binding partners (Padrón-Barthe et al. 2019). However, so far the TMEM43 mutation was only described mislocalized within the nuclear compartment (Siragam et al. 2014), thus compromising the stiffness of the nuclear envelope (Milting et al. 2015) and also modulate the expression of mechanosensitive genes (Zheng et al. 2019). The excessive expression of a TMEM43 mutation activates cascades mechanosensitive signaling, including NF- κ B signal pathways, which then activate the TGF- β (Zheng et al. 2019). The cross-talk between these signaling leads to increase stress and ECM stiffness, thus increasing expression of A-type lamin, which helps stabilize and protect the nucleus (Isermann and Lammerding 2013). At the cellular level, the transforming growth factor- β (TGF- β) controls many cellular responses, including unfolded protein response (UPR) (Okumura et al. 2017). The UPR is the adaptive response to ER stress. Signaling of the UPR is mediated by three master regulators; inositol-requiring protein-1 (IRE1), PKR-like ER kinase (PERK), and activating transcription factor 6 (ATF6) (Walter et al.

2018). During the normal conditions of the cell, Immunoglobulin binding protein (BiP) also known chaperone (GRP78) is lying in the lumen of the endoplasmic reticulum where it binds to the luminal domains of these master regulators which in-turn keeping them inactive (Pobre et al. 2019). Unlike normal conditions, stress conditions lead to dissociation of Immunoglobulin binding protein from these sensors resulting in their activation (Bravo et al. 2013). However, if the UPR fails to restore ER homeostasis to the original state, the UPR signaling switches from pro-survival to pro-apoptotic effect via the overexpression of the C/EBP homologous protein (CHOP) (Hu et al. 2018). These observations may give evidence that the TMEM43 mutation ultimately causes accumulated cellular stress, thus stimulating apoptosis and cell death.

The main objectives of this study

- A. The TMEM43 protein is located between the INM and ER. It is part of the LINC complex ingredients, which plays a crucial role in mechanosensitive and mechanotransduction. Our research group was demonstrated that the pS358L mutation in the TMEM43 gene causes impairment in the nuclear machine. However, the disease underlying molecular mechanism of the TMEM43 mutation has yet to be clarified. So, the goal of this study was to gain more insights into the disease-causing mechanisms induced by the expression of pS358L at the cellular level.
- B. The endoplasmic reticulum (ER) is the main factory for protein synthesis within cells. Interference with the protein-making system produces cellular stress, which changes the normal functioning of proteins significant for cell survival. So, the main goal of this study was to provide a novel way to understand the crosstalk between the dynamic processes of the ER stress and the biophysical activity at the single-cell level and also how it contributes to the development of the ARVC5 diseases.

1.2 Materials and Methods

1.2.1 Cell lines

In this work, the wild-type and mutant (p.S358L) human TMEM43 tagged at the C-terminus with GFP to generate stably transfected HeLa cell line (cervical adenocarcinoma) was used to study effect mutation of the transmembrane protein 43 (p.S358L) on the elasticity of the cell as a whole. Also, the HEK293 (human embryonic kidney) was used as a model system to evaluate the Nanomechanical properties of the cell nucleus experienced by endoplasmic reticulum (ER) stress to compare the results of these experiments with HEK293 lines which were transfected with the mutant (GFP-TMEM43-S358L) protein.

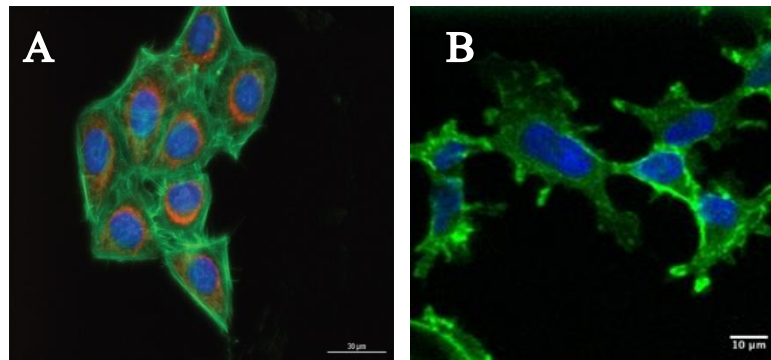


Figure 1-6: Fluorescent microscopy images of the cells, the image (A) describe the characteristics of adherent HeLa cells where the total size of cells=20 microns diameter (cell nucleus ~10-micron diameter) (website of BioTek company), while the Image (B) describe the characteristics of adherent HEK293cells cells where the total size of cells=13 microns (website of Kerfast company).

1.2.2 Sustaining cell lines

The cell lines used in these experiments needed to be sub-cultivated up to twice a week to non- transfected cells to allow them to continue to grow and one time for transfected to prepare samples. Sub-cultivation was performed as follows in a clean cabinet, the culture medium was aspirated from the cell flask, and the cells were washed with 6 mL (for a filter cap T25cm² flasks (Greiner BioOne, Germany) of sterile phosphate-buffered saline (PBS). The PBS was then removed, and 500μL of trypsin-EDTA (PAA Laboratories, Austria) was added to the flask before incubating the cells at 37C and 5% CO₂ for 5 min. Trypsin is a protease which detaches the adherent cells from the

supernatant was then removed, and the cell pellet was re-suspended in 6 mL of fresh media appropriate to the cell type being sub-cultivated. Then an appropriate volume of cell suspension was added to the new flask containing 4 mL of fresh media, and the flask(s) were then incubated at 37°C and 5% CO₂. In this way, prepared cells are ready for use in the further experiment.

1.2.3 Prepare cell lines for the transfection process

First of all, HeLa cell lines cell line were seeded in 25 cm² flasks at 37 °C, 5% CO₂ in Dulbecco's modified Eagle's medium (DMEM) (Life Technologies, Darmstadt, Germany) supplemented with 10% fetal bovine serum (FBS)(PAA Laboratories, Cölbe, Germany), and 1% (w/v) penicillin (100 U/mL) and streptomycin (100 µg/ml) (PAA Laboratories, Austeria). The cells were passaged when confluent. Media replaced every two to three days until cell were 90% confluent prior for transfection.

The HEK 293 cell Lines were maintained in DMEM (Life Technologies, Darmstadt, Germany) containing 10% FBS (PAA Laboratories, Cölbe, Germany) and 1% antibiotics (penicillin and streptomycin) at 37 °C, 5% CO₂. The culture media was changed every two days until the cells were 90% confluent.

In transfection of eukaryotic cells, the reagent Lipofectamin 2000 (Invitrogen, Carlsbad, USA) was used. The liposomes with the attached plasmid DNA is taken up by the cells through endocytosis. For this, the eukaryotic cells were cultivated 24-48 h before transfection in DMEM growth medium to a confluence of 70%. The transfection was carried out according to the manufacturer's instructions. After 24-48 h, cells were analyzed (Fig.1-7). The transfections of cells were prepared at the Erich and Hannah Klessmann institute by Sandra Ratnavadivel and Daniela Baurichter.

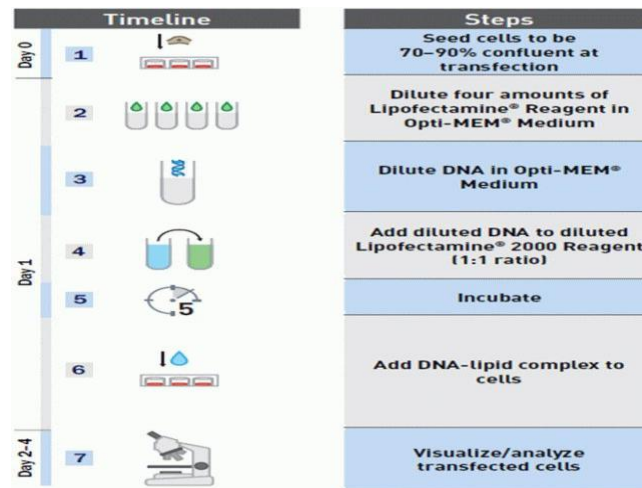


Figure 1-7: The transfection protocol in eukaryotic cells (from Sandra Ratnavadivel thesis).

1.2.4 Measurement samples

1.2.4.1 Estimation of elasticity in HeLa cell lines

The experiment was designed to assess the mechanical mapping of the mutation of the transmembrane protein 43 (p.S358L) which causing ARVC type 5 on the elasticity of the cell nucleus, and cytoplasm using wild-type and mutant (p.S358L) human TMEM43 tagged at the C-terminus with GFP to generate stably transfected HeLa cell line where the HeLa cells were cultivated in DMEM medium under a humidified 5 % CO₂-atmosphere on glass-bottom Petri dish Will-co (WillCo Wells B.V., Amsterdam, Netherlands) for 48 h. After incubation, cells were scanned in perfusion cell in fresh DMEM growth medium in 37 °C. Mechanical mapping was done on non-fixed living cells.

Therefore, these experiments were divided into two groups:

- **Group I:** The HeLa cell lines were transfected with GFP-TMEM43-S358L protein.
- **Group II:** The HeLa cell lines were transfected with GFP-TMEM43-WT protein.

1.2.4.2 Induction of ER stress in HEK 293 cell line

The experiment was designed to assess effect endoplasmic reticulum (ER) stress on the elasticity of the nucleus area using HEK293 cells. Pharmaceutical ER stress inducers tunicamycin and thapsigargin to induce ER were used. Use the dimethyl

sulfoxide (DMSO) (Sigma-Aldrich, Germany) as a solvent for inducers where the concentration of the thapsigargin (2mg/ml) and tunicamycin (1mg/ml). The HEK293 were cultivated in DMEM medium under a humidified 5 % CO₂-atmosphere on glass-bottom Petri dish Will-co for 72h. After incubation, the media has been changed and added two different volumes (0.1% and 0.25%) in each measurement from thapsigargin (positive control), tunicamycin (positive control) and DMSO (negative control) to cells and incubation for 6 hours to induce ER stress. After incubation, Petri dishes were taken out of the CO₂ incubator and placed on the sample stage for AFM experiments. Elastic mapping was done on non-fixed living cells.

1.2.4.3 Estimation of elasticity in HEK 293 cell line

The experiment was designed to assess the effect the mutation of the transmembrane protein 43 (p.S358L) on the elasticity of the nucleus area using HEK293 cells. Using three transfected HEK293cell lines and according to the following divisions:

- **Group I:** The HEK293 lines were transfected with the mutant (GFP-TMEM43-S358L) protein.
- **Group II:** The HEK293 lines were transfected with the wild-type (GFP-TMEM43-WT) protein.
- **Group III:** the HEK293 lines were transfected GFP without TMEM43protein.

All three samples of the transfected HEK293 cell lines were cultured in DMEM medium beneath a humidified 5 % CO₂-atmosphere on glass-bottom Petri dish Willco (Willco wells BV) and grew for 72 h in a cell incubator. After incubation, using AFM the cells were scanned in perfusion cell in fresh DMEM growth medium in 37 °C and elasticity maps were obtained by living cells.

1.2.5 AFM Techniques

1.2.5.1 AFM setup

An Asylum Research MFP-3D (Goleta, CA, USA) was used to capture the total of atomic force microscope (AFM) data. The MFP-3D is an integrated AFM with an inverted optical microscope (Olympus IX 71, Tokyo, Japan) to allow optical microscopy techniques to be completed simultaneously with AFM data capture. Indeed, it is a substantial tool for studying the mechanical properties of biological samples when the sample can be viewed using the optical microscope in order to locate specific cell

areas to acquire mechanical measurements using the AFM. This setup helps the use of fluorescence camera in order to identify cells that have been 'tagged' with specific markers to detect sub-populations of cells with a particular interest.

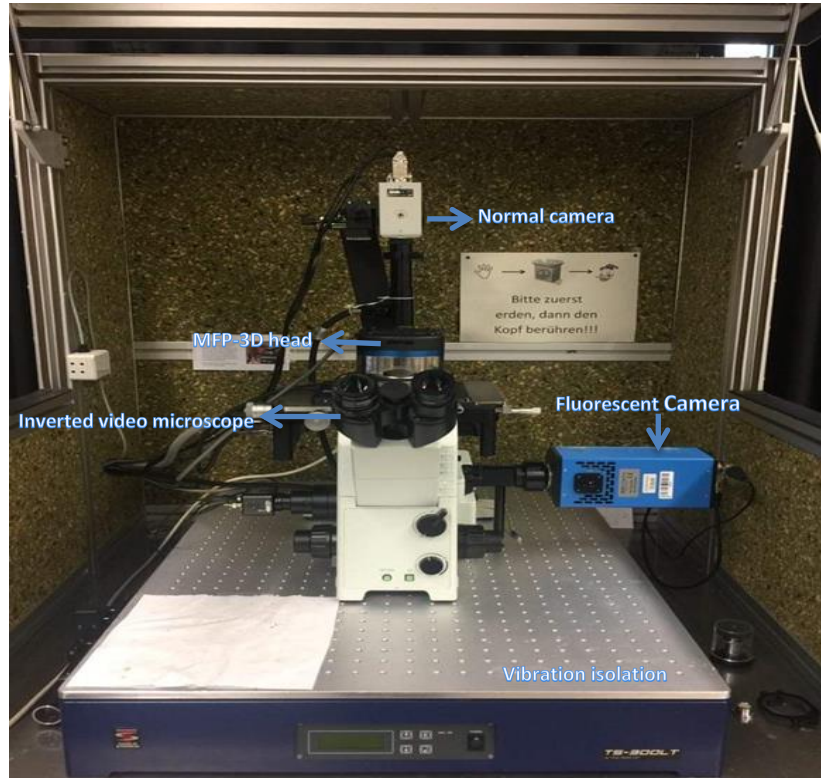


Figure1-8: Image illustrates the AFM setup (from professor Anselmetti lab)

1.2.5.2 AFM probe selection

It is very important to select a suitable tip for force spectroscopy experiments, taking in consideration of the cantilever geometry, tip geometry and spring constant. So, this portion has specific considerations to be addressed when choosing of elasticity measurements on living cells. The type of AFM probe used in this study was soft silicon nitride DNP-10; cantilever D, with spring constant 0.06 N/m according to the manufacturer's instructions (Bruker, Camarillo, USA).

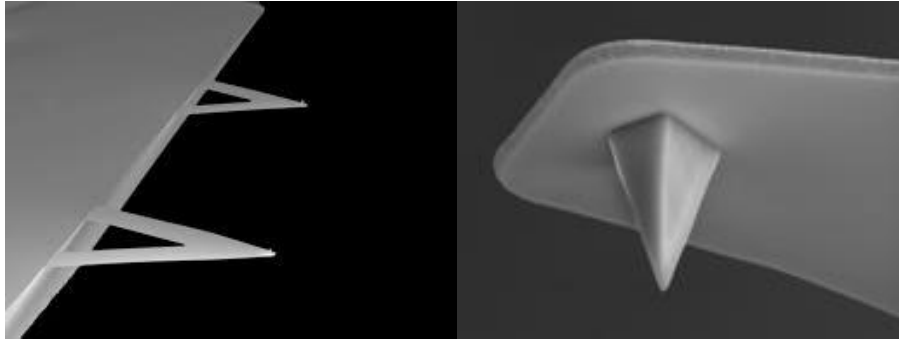


Figure 1-9: Images of silicon nitride DNP10 (Bruker, Camarillo, USA).

1.2.5.3 Calibration of cantilever spring constants

Atomic force microscope (AFM) cantilevers are used in growing applications not only in surface imaging but also force spectroscopy, viscosimetry and the study electrochemistry (Gibson et al. 2003). The use of cantilevers in these applications requires precise knowledge of the physical properties, especially the spring constant (Gibson et al. 2001). In the force spectroscopy experiments, the spring constant of the cantilever must be estimated by calibrating the cantilever. This calibration is necessary to obtain force versus distance information from the force measurement data. The calibration is done by calculating the detection sensitivity of the cantilever via indenting an incompressible surface like a glass slide or mica, in order to measure the voltage response of the position-sensitive photodiode as a function of z scanner displacement. The knowledge of the cantilever spring constant is useful to calculate the force which was being applied to the sample; thus, deduce elastic the modulus of the sample from such force-distance data. There are some corrections which can be applied, such as the position of the optical spot focused on the back of the cantilever that has an effect on the precision of the detection sensitivity of cantilever. These errors that may take place during measurement of the detection sensitivity have an effect on the predestined spring constant of the cantilever (Proksch et al. 2004). The thermal noise method is one of the most well-known methods in calibrating a cantilever to calculate its spring constant using two procedures. The first procedure measures the thermal fluctuations of the cantilever that supply the power spectrum of the cantilever response in unit V^2Hz^{-1} . The second procedure is used to measure a conversion factor to convert this unit into m^2Hz^{-1} , this factor indicate to inverse optical lever sensitivity (InvOLS) with units of mV^{-1} which is usually measured by making contact with a stiff surface, push the free end of the cantilever a known distance and measuring the voltage response of the

detection transducer (usually a position sensitive photodetector) achieved by earning a force curve (Hutter and Bechhoefer 1993; Schäffer 2005). In the thermal noise, the cantilever is treated as a simple harmonic oscillator which can be described by the Hamiltonian:

$$H = \frac{p^2}{2m} + \frac{1}{2}m\omega_0^2x^2 \quad Eq. 1$$

Where m is the mass of the oscillator, p it's momentum, ω_0 is the resonant angular frequency and x is the vertical displacement of the oscillator. By the equipartition theorem each quadratic term x^2 : p^2 in the Hamiltonian has the average value of $\frac{1}{2}k_B T$ where k_B is Boltzmann's constant and T is the absolute temperature. Therefore:

$$\frac{1}{2}m\omega_0^2 \langle x^2 \rangle \quad Eq. 2$$

By substituting $\omega_0^2 = k/m$ into equation 2 the spring constant can be obtained by measuring the mean square displacement $\langle x^2 \rangle$ of the oscillator, or in this case the cantilever, as

$$k = \frac{k_B T}{\langle x^2 \rangle} \quad Eq. 3$$

Here, the spring constant is calculated by measuring the power spectral density of the cantilever displacement, which is represented by a Lorentzian shape figure. The power spectrum is integrated to give $\langle x^2 \rangle$ of the cantilever fluctuations which are also equal to the mean square of the cantilever fluctuations.

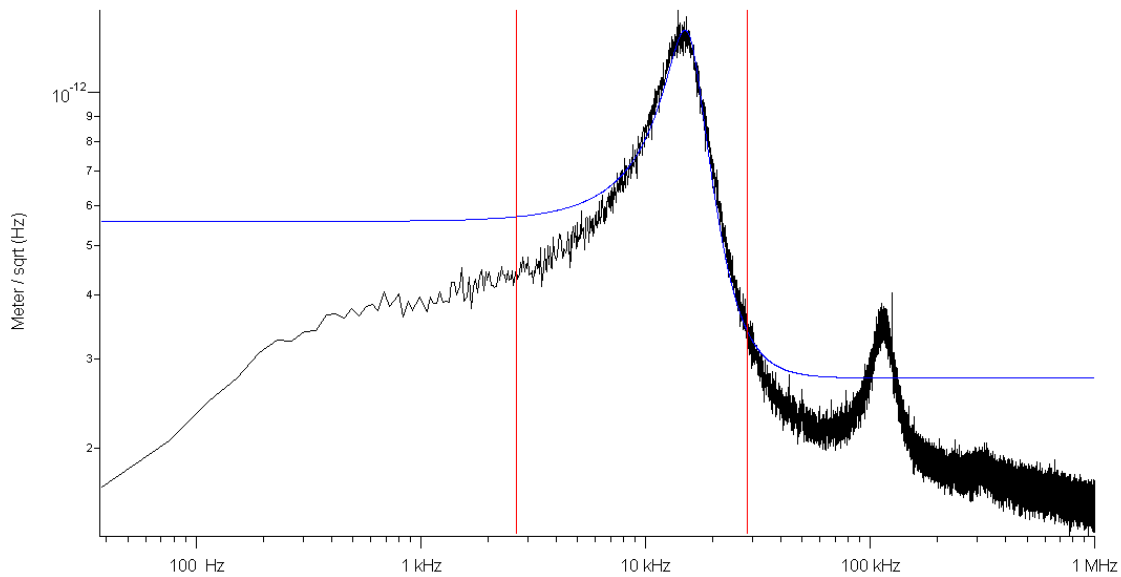


Figure1-10: The curve appears thermal tune of a contact mode cantilever in the liquid environment. The blue line represents the Lorentzian to the first resonant peak.

In this figure, $\langle x^2 \rangle$ represents the area beneath the Lorentzian curve.

1.2.6 Elasticity Measurements

All elasticity measurements were obtained using an (Asylum Research, Goleta, CA, USA) AFM integrated with an inverted optical microscope (Olympus IX 71). The measurements were performed with the living cells in their convenient culture media and temperature, so as to ensure cell viability and stability. The cantilever spring constant, k was calibrated before each experiment by the thermal tune method using the Asylum software, the cantilever sensitivity was calibrated on the bare substrate. All elasticity measurements were made by using silicon nitride probe (DNP-10, Bruker; cantilever D), with a tip radius of 20–60 nm, was attached to a triangular 200 nm-long cantilever with spring constant 0.06 N/m according to the manufacturer's instructions. A new probe was used for each experiment in contact mode. For each experiment, up to 20 cells were indented, and at least four experimental duplicates were completed on each cell line. First, each cell was examined using the inverted optical microscope; then, the cantilever was directed over the regions of interest inside the cells. Exact adjustment of the cantilever position might be accomplished in a proficient by applying offsets to the X and Y scanners. The AFM cantilever must be pulled back from the example surface while moving the example stage to choose a target cell. In Force Spectroscopy mode, a constant indentation velocity of $3 \mu\text{m s}^{-1}$ was used, which was somewhat slow to reduce the hydrodynamic force exerted on the cantilever from the culture media.

This velocity will be sufficient to provide a sudden indentation to allow investigation of the mechanical properties of cells. We have been set the trigger point for deflection because it limits the maximum indenting force to avoid cells damage. The correction for any drift in the deflection signal will be by selection the Relative triggering option. A constant trigger force of 2nN was used throughout the experiments corresponding to indentations 500 nm and 300nm depending on both of the cell line and differences in the elasticity within each cell. Both of the constant indentation speed and trigger force was used throughout to ensure the loading rate that was constant as much as possible so that any loading rate-dependent changes in mechanical properties were kept to a minimum rate. In our experiments, multiple curves were collected on every cell to obtain reliable statistical data (take a large number of force curves can result in changes in cell stiffness due to stress from the AFM probe) (Thomas et al. 2013).

1.2.6.1 Force-indentation curves

Young's moduli are calculated from the force-distance curves. Typically, it is measured on stiff and compliant surfaces, as shown in figure 11, which explains a typical force-distance curve. At the beginning of the indentation, the probe is away from the surface as indicated by point A on fig 11 in which there is no interaction between them. Afterwards, the probe proceeds towards the surface where the forces of attraction between them are generated such as van der Waals, electrostatic or capillary forces. At some tip-sample distance, the attractive forces overcome the cantilever stiffness and the tip leaps into contact with the surface. Accordingly, the tip remains on the surface, and this lead-tin order to increase the loading force on the probe, the deflection of the cantilever also increases; therefore, pressing the sample. Later on, the probe begins to withdraw to its initial position. During the unloading process, the force starts to decline and reaches a point when the probe "jumps off" from the surface. The force of this point is defined by the adhesion force between the tip and the surface. The absence of deformation leads to appears only the adhesion term. Moreover, the maximum deformation of the sample can be assessed where it can be calculated as a distance between the point B on Fig. 1-11 that represents the maximum loading force and the point at which, the tip reaches the surface (jump-to-contact point). At the repulsive area, the curvature of the approaching and withdrawing curves testify that the probe has indented the surface (Codan et al. 2014; Kámán 2015). There are several discretional models of contact mechanics, such as the Hertz model, JRK (Johnson-Roberts-Kendall

model) (Ciavarella et al. 2019; Kontomaris 2018). In our nano-indentation experiments, we used the Hertz model to extract data from the force-distance curves to get Young's modulus.

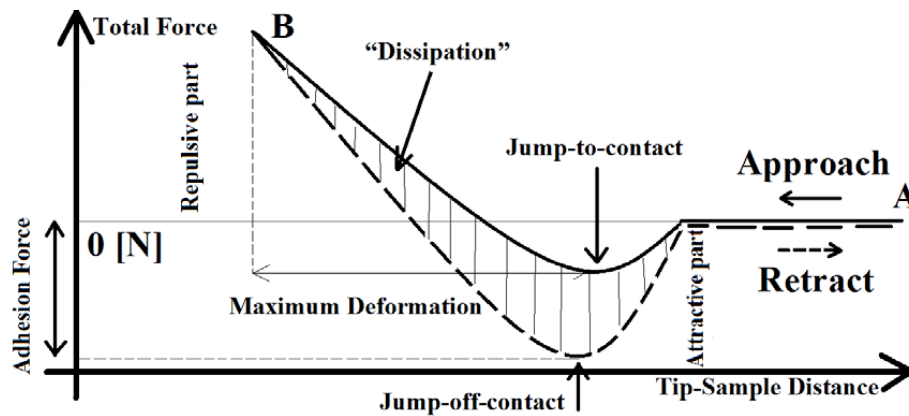


Figure 1-11. A diagram explains the typical force-distance curve, where the fully striped area is not necessarily only the work of the dissipation; some parts can be derived from adhesion work (Kámán 2015).

1.2.6.2 Modeling of cells elasticity

The hertz model is used as a fitting model to determine the elastic modulus (E_{Hertz}) of soft samples by a stiff cone, and it depends on force versus indentation relationships obtained from the elasticity experiments using AFM (Rosenbluth et al. 2006). So, the Hertz model was the most appropriate model in analyzing all data collected from each elasticity measurements for all cell lines, so that the Asylum Research software package was used to supply Young's modulus for each point as calculated by the Hertz model. The accuracy of this model is highly dependent on the localization of the contact point, which was selected manually and was clear on the great majority of curves. In all measurements, we supposed a Poisson's ratio $\nu = 0.5$, as a typical ratio for soft biological material where incompressibility is assumed. For all cells and fit the model to the indentation range of approximately 45–95 % of the collected data, and this leads to avoiding early contact point which tends to be highly variable due to the complication of the cell surface. The geometry of the AFM tip can be of different forms: pyramidal, conical, or parabolic. Therefore, the determination of the equation used will depend on the form of the tip of the cantilever. The indentation data is approximated by the Sneddon's equation (Equation 1) which is a solution of the Hertz model for a conical indenter (Lin et al. 2007).

Conical

$$F = \frac{E}{1 - \nu^2} \frac{2 \tan \alpha}{\pi} \delta^2 \quad \text{Eq. 1}$$

Where F is indenting force, δ is indentation distance, E is Young's modulus of the sample, ν is the Poisson's ratio, and α is semi-opening cone indenter which is calculated from the following equation 2:

$$\alpha = \frac{2 \tan \alpha}{\pi} \delta \quad \text{Eq. 2}$$

1.2.7 Statistics

Force-indentation curves of all living cells used in elasticity experiments were acquired from software for the MFP3D (Asylum Research, Goleta, CA, USA) atomic force microscope (AFM) which was mounted on an inverted optical microscope (Olympus IX 71, Tokyo, Japan). E_{Hertz} were extracted from the force-indentation curves by the fitting of the Hertz model (as shown in the section 4.4.4.2 Modeling cells elasticity). The results are exported to a program Origin Lab (version 9) to get histograms. The statistical histograms data are given as median \pm standard deviation (SD). The Young's modulus values for each group were compared by analysis of variance followed by the Mann-Whitney U test. *P*-values of less than 5% were considered as statistically significant.

1.3 Results

1.3.1 TMEM43 mutation influences stiffness distributions of HeLa cell line

In order to accomplish these experiments, the green fluorescent protein (GFP) as a tag to generate constructs consisting of full-length wild-type (GFP-TMEM43-WT), mutant (GFP-TMEM43-pS358L) TMEM43 in HeLa cells was used. The HeLa cell lines are considered fairly easy to transfect and very receptive to viral vectors. For this reason, it has become a common research tool in transfection experiments all over the world (Holliday and Speirs 2011). The Young's modulus is obtained from the force-distance curves. Fig.1-12 is a typical force curve estimated in living cells. During the indentation measurements of obtaining a force curve, the probe first approached and then withdrew from the surface of the living cells. The approach curve was used for calculation of the cellular Young's modulus. Before the connection of the tip of the cantilever with the cell surfaces, the curve was flat, but upon connection, the curve tends to be bent.

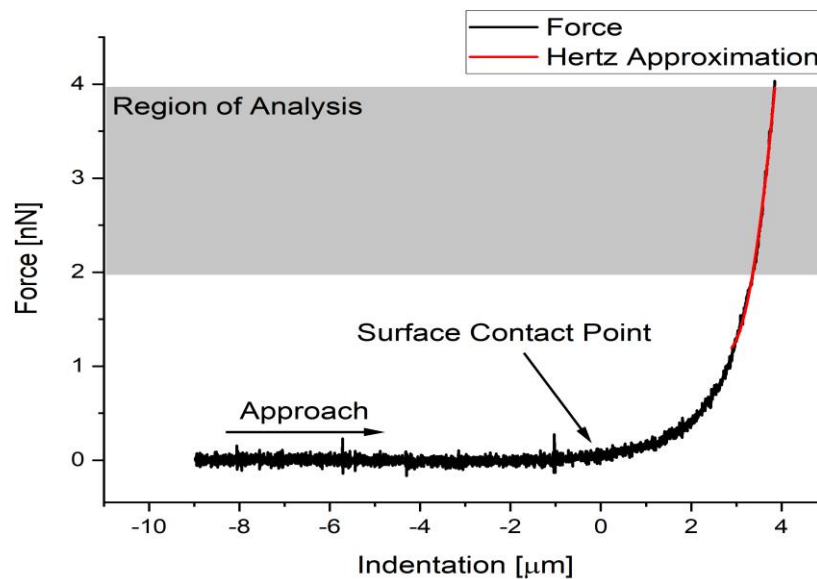


Figure 1-12: Typical force curve obtained from living cells.

The elasticity maps show a stiffness distribution cell after the recording of 64×64 force curves on the cell surface. The data are presented in the form of simultaneous images taken from single transfect (GFP-TMEM43-WT) and (GFP-TMEM43-S358L) cell lines. Those images consist of a bright-field image (Fig.1-13D), fluorescence image (Fig.1-13C), topography image (Fig. 1-13B); the elasticity image (Fig. 1-13A) is congruent to topography image. Both have an identical scale, thus allowing direct comparisons.

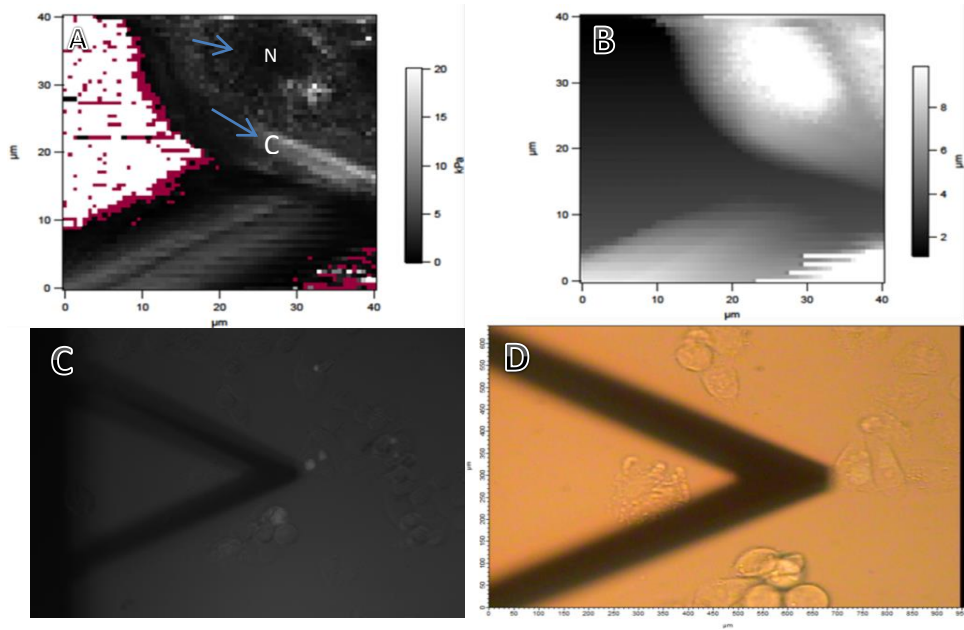


Figure 1-13: Elasticity map (A) corresponding topography of (GFP-TMEM43-WT) transfected HeLa cell line (B), Optical fluorescence image (C) and bright-field optical image of the cell (D). Force curve velocity $3.00 \mu\text{m/s}$, force curve rate 1.5 Hz , $64 \text{ pixel} \times 64$ force curves. Data acquisition time was 60 min . The arrows indicate nucleus (N) and cytoplasm(C).

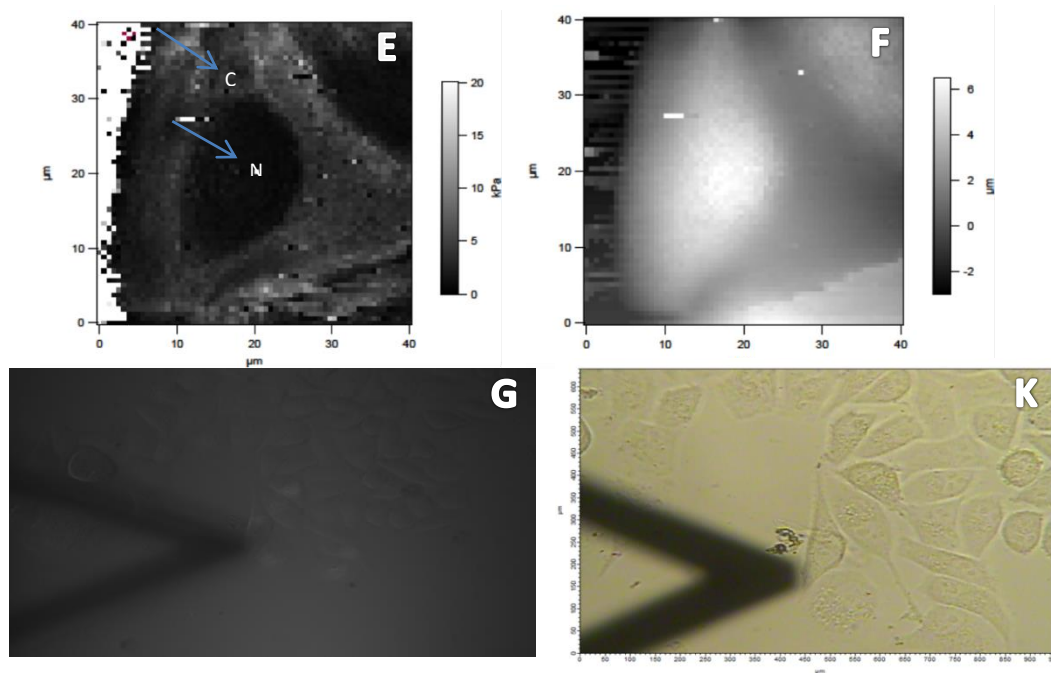


Figure1-14: Elasticity map (E) corresponding topography (GFP-TMEM43-S358L) transfected HeLa cell line (F), Optical fluorescence image (G) and bright-field optical image of the cell shown in (K). Force curve velocity 3.00 $\mu\text{m/s}$, and force curve rate 1.5 Hz, 64 pixels \times 64 force curves. Data acquisition time was 60 min. The arrows indicate nucleus (N), and cytoplasm(C).

We notice that the force maps were variable in (GFP-TMEM43-WT) as a comparison with GFP-TMEM43-S358L) transfected HeLa cells, which is because of cell membrane being highly heterogeneous due to the high levels of lipid rafts (Lingwood and Simons, 2010). In order to make a statistical evaluation of stiffness distributions in local areas, which include the nucleus and cytoplasm of the HeLa cell that were transfected with (GFP-TMEM43-WT) and (GFP-TMEM43-S358L), we analyzed 14-22 different cells bearing the wild-type and mutant plasmid, respectively. Force curves were obtained on the entire cell. The histograms in (Figure15 A and B) of Young's modulus calculated from a set of force curves show the distribution of Young's moduli of (GFP-TMEM43-S358L) (7.8 ± 6.4 kPa) cells and GFP-TMEM43-WT (1.6 ± 0.8 kPa). Obviously exhibits a largest elastic modulus.

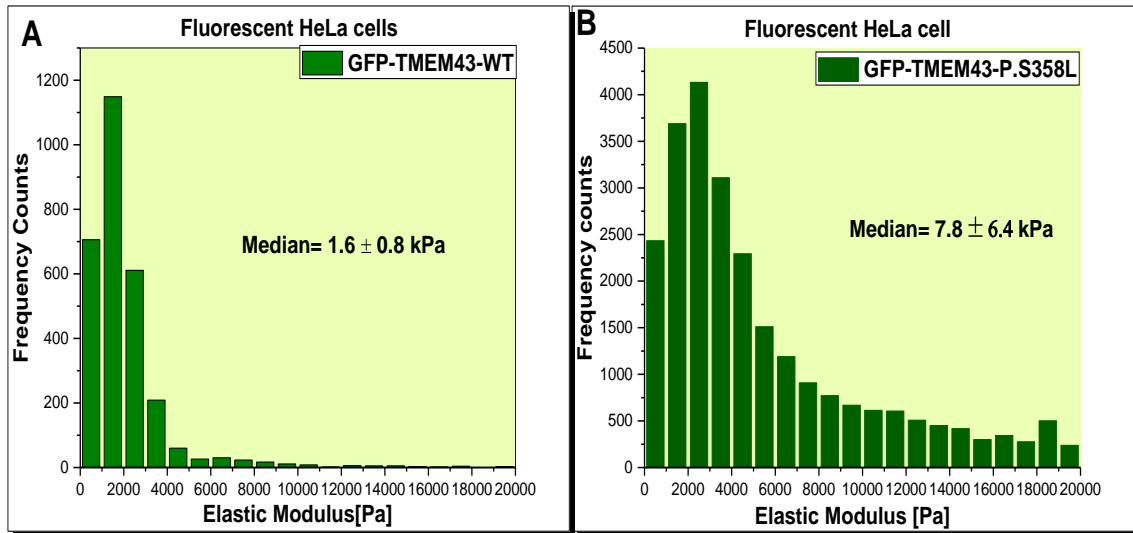


Figure 1-15: Histograms represent effects on the elasticity modulus of transfected HeLa cells, (A) Young's modulus measured on entire wild-type (GFP-TMEM43-WT), (B) Young's modulus measured on entire mutant (GFP-TMEM43-S358L).

Force curves were obtained from the nucleus of HeLa cell line transfected with (GFP-TMEM43-WT) and (GFP-TMEM43-S358L). The histograms (Fig. 1-16 A and B) of Young's modulus clearly show that the elasticity of the cells transfected with (GFP-TMEM43-S358L) was (7.3 ± 6.0 kPa) which is remarkably stiffer than those transfected with (GFP-TMEM43-WT) (2.3 ± 1.4 kPa).

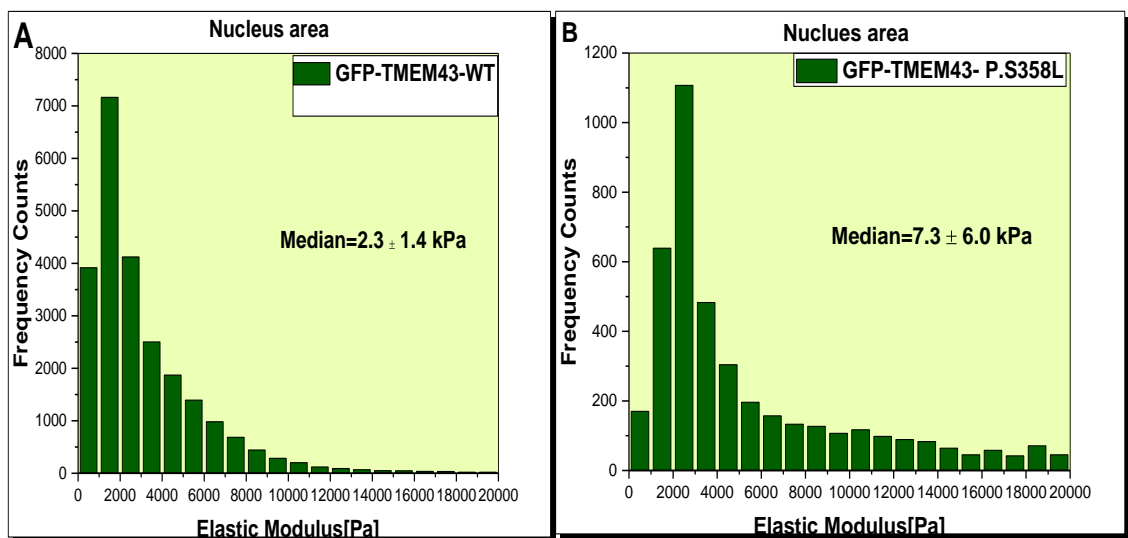


Figure 1-16: Histograms represent effects TMEM43-S358L on the elasticity modulus of the nuclear zone of transfected HeLa cells, (A) The Young's modulus measured on the nucleus of wild-type (GFP-TMEM43-WT) and (B) mutant (GFP-TMEM43-S358L).

Recent reports have shown that the TMEM43 (nuclear membrane protein) is concentrated in the inner nuclear membrane and is also expressed outside the nucleus, including the endoplasmic reticulum (Siragam et al. 2014). For that reason, we analyzed the effect of mutation of TMEM43 in the cytoplasm stiffness. The results in Figure 1-17 (A and B) indicate that Young's modulus in the cytoplasm area of (GFP-TMEM43-S358L) transfected cell line was (8.9 ± 7.1 kPa) that is substantially stiffer than transfection with (GFP-TMEM43-WT) (2.4 ± 0.7 kPa).

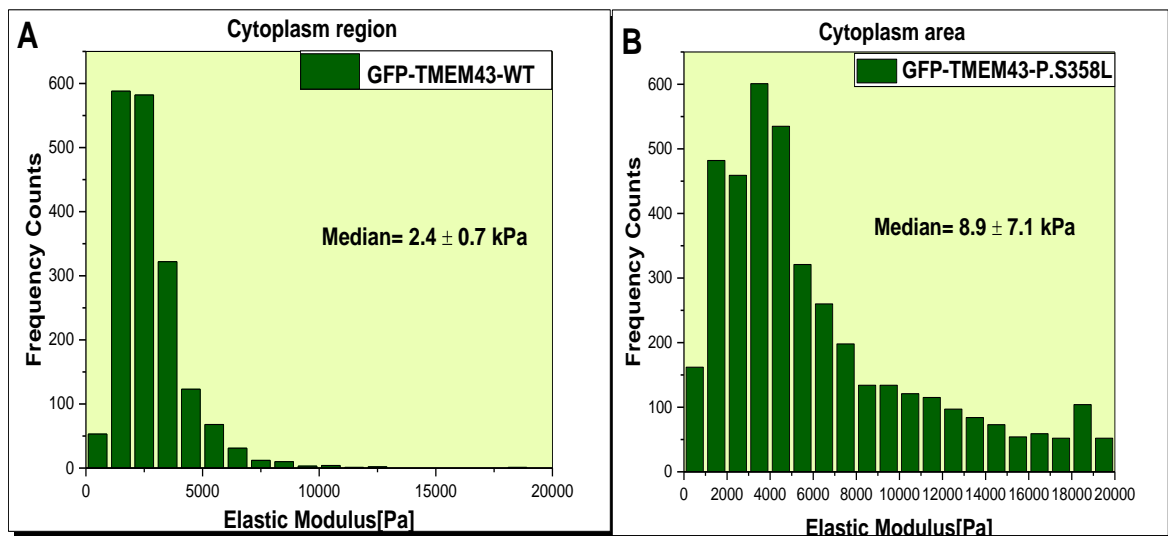


Figure1-17: Histograms represent effects on the elasticity modulus of the cytoplasm area in transfected HeLa cells, (A) Young's modulus measured on cytoplasm transfected with (GFP-TMEM43-WT) and (B) (GFP-TMEM43-S358L).

The results of the impacts of TMEM43 mutation on the mechanical properties inside and outside the nucleus of HeLa cells was summarized in (table1). It was observed that the average median and SD values of Young's modulus of local areas of the transfected HeLa cells (GFP-TMEM43-S358L) were significantly higher than the (GFP-TMEM43-WT) cells. Thus, all elasticity distributions of TMEM43-S358L mutation exhibited significant statistical differences ($p < 0.05$) (Fig.1-18).

Table 1-1: Young's modulus measured by AFM on top of HeLa cell line transfected with wild-type (GFP-TMEM43-WT) and mutant (GFP-TMEM43-S358L). The values represent the median \pm and the standard deviation (SD) over n cells.

| Groups | GFP-TMEM43-WT Young's modulus(kPa) Median \pm SD | N | GFP-TMEM43-S358L Young's modulus(kPa) Median \pm SD | n | P-value |
|----------------|--|----|---|----|------------|
| whole cell | 1.6 \pm 0.8 | 14 | 8.7 \pm 6.4 | 21 | $p < 0.02$ |
| nucleus area | 2.3 \pm 1.4 | 22 | 7.3 \pm 6.0 | 19 | $p < 0.01$ |
| cytoplasm area | 2.4 \pm 0.7 | 14 | 8.9 \pm 7.1 | 20 | $p < 0.02$ |

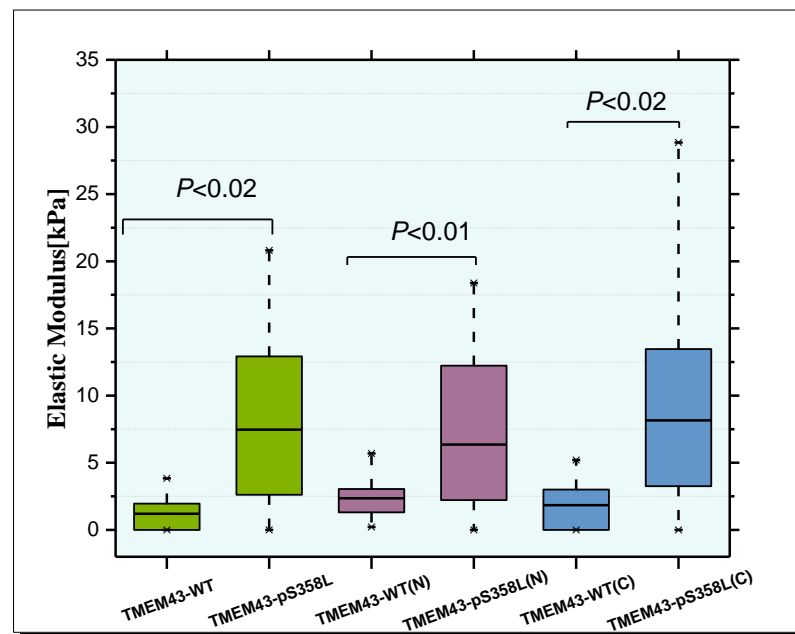


Figure 1-18: The box plot provides the average median values for elastic responses at different areas of wild-type (GFP-TMEM43-WT) and mutant (GFP-TMEM43-S358L) transfected HeLa cell line.

1.3.2 ER stress influences nucleus stiffness of HEK293 cell line

Next, we determined the effect of ER stress on the elasticity of the cell nucleus in HEK293 cells. Furthermore, we checked the effect of increasing the concentration of pharmaceutical inducers on the stiffness level in the nucleus. The HEK293 (human embryonic kidney) was originally generated in 1977 from the sheared Adenovirus 5 (Ad5) DNA by the transformation of the human embryonic kidney cell (Kovesdi and

Hedley 2010). Elasticity measurements during pharmaceutical inducers action were performed by recording a series of force maps on the nucleus of HEK293 cell and analyzing the force curve data by using the Hertz model (Fig.1-19). In order to evaluate the effects of ER stress on the mechanical properties of HEK293 cells, different agents like; Thapsigargin (2mg/ml) and Tunicamycin (1mg/ml) are added to the cell media. Thapsigargin is a selective inhibitor of the sarcoendoplasmic Ca^{2+} -ATPase. Inhibition leads to lowered calcium levels in the ER (Sehgal et al. 2017). When calcium levels decrease in the ER, the calcium-dependent ER chaperones, such as calnexin, lose their chaperone activity, causing the accumulation of unfolded proteins in the ER and consequently increasing the ER stress (Osowski and Urano 2011). On the other hand, Tunicamycin causes blocking the initial step of glycoprotein biosynthesis in the ER, causing an accumulation of unfolded glycoproteins in the ER, leading to ER stress (Yoshida and Sakai 2011). As a negative control, we used Dimethyl sulfoxide (DMSO). It is one of the organic solvents vastly utilized in various cell culture studies (Rodríguez-Burford et al., 2011). In all experiments, the incubation time was six hours. Force curves were obtained at the nuclear zone. At 0.1% volume, Young's modulus of the nuclear zone of HEK293 cells increased significantly upon treatment with thapsigargin (1.33 ± 0.65 kPa) and tunicamycin (1.42 ± 0.44 kPa) compared with nuclear zone treated with 0.1% (DMSO) (0.93 ± 0.51 kPa) (Fig. 1-20, A, C and E). In respect to 0.25% volumes, Young's modulus of the HEK293 cells that treated with volume 0.25% for both the thapsigargin and tunicamycin was compared with the volume 0.25% of DMSO. The histograms (Fig.1-20, B, D, and F) clearly showed an increase in Young's modulus rates of the HEK293 cells nuclear area treated with 0.25% for each the thapsigargin and tunicamycin compared with nuclear zone treated with 0.25% (DMSO), where the values of thapsigargin and tunicamycin were respectively (1.44 ± 0.10 kPa) (2.20 ± 0.25 kPa), while the values of the DMSO were (0.86 ± 0.40 kPa). In brief, both pharmaceutical inducers showed a significant increase in the stiffness of the nuclear zone compared to the nuclear zone treated with DMSO.

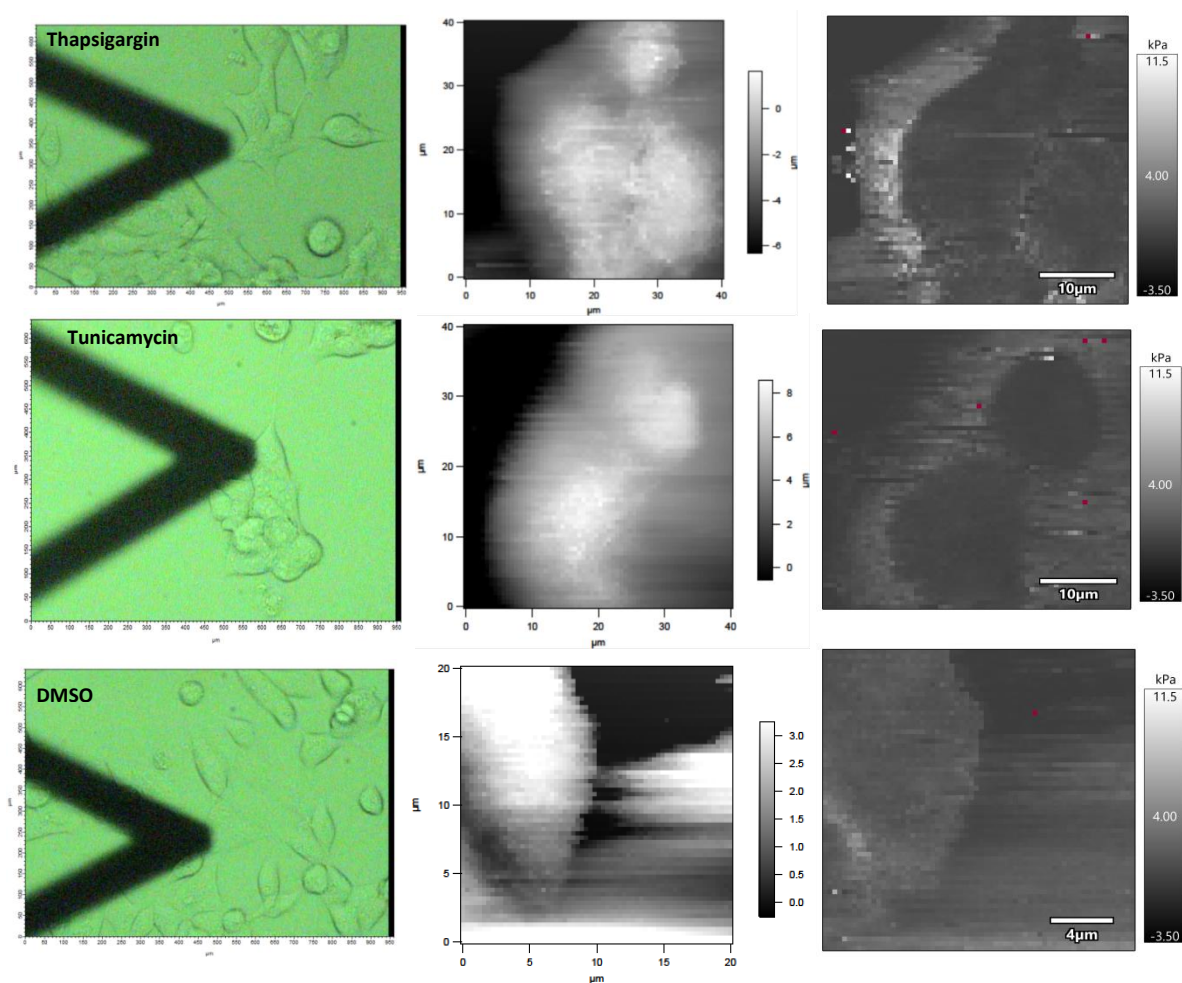


Figure 1-19: AFM images of HEK293 cells treated with (Thapsigargin), (Tunicamycin) and (DMSO), Force curve velocity 3.00 $\mu\text{m/s}$, force curve rate 1.5 Hz, 64 pixel \times 64 force curves. Data acquisition time was 60 min. After the AFM experiment, elasticity maps corresponding to possess differences in Young 'modulus

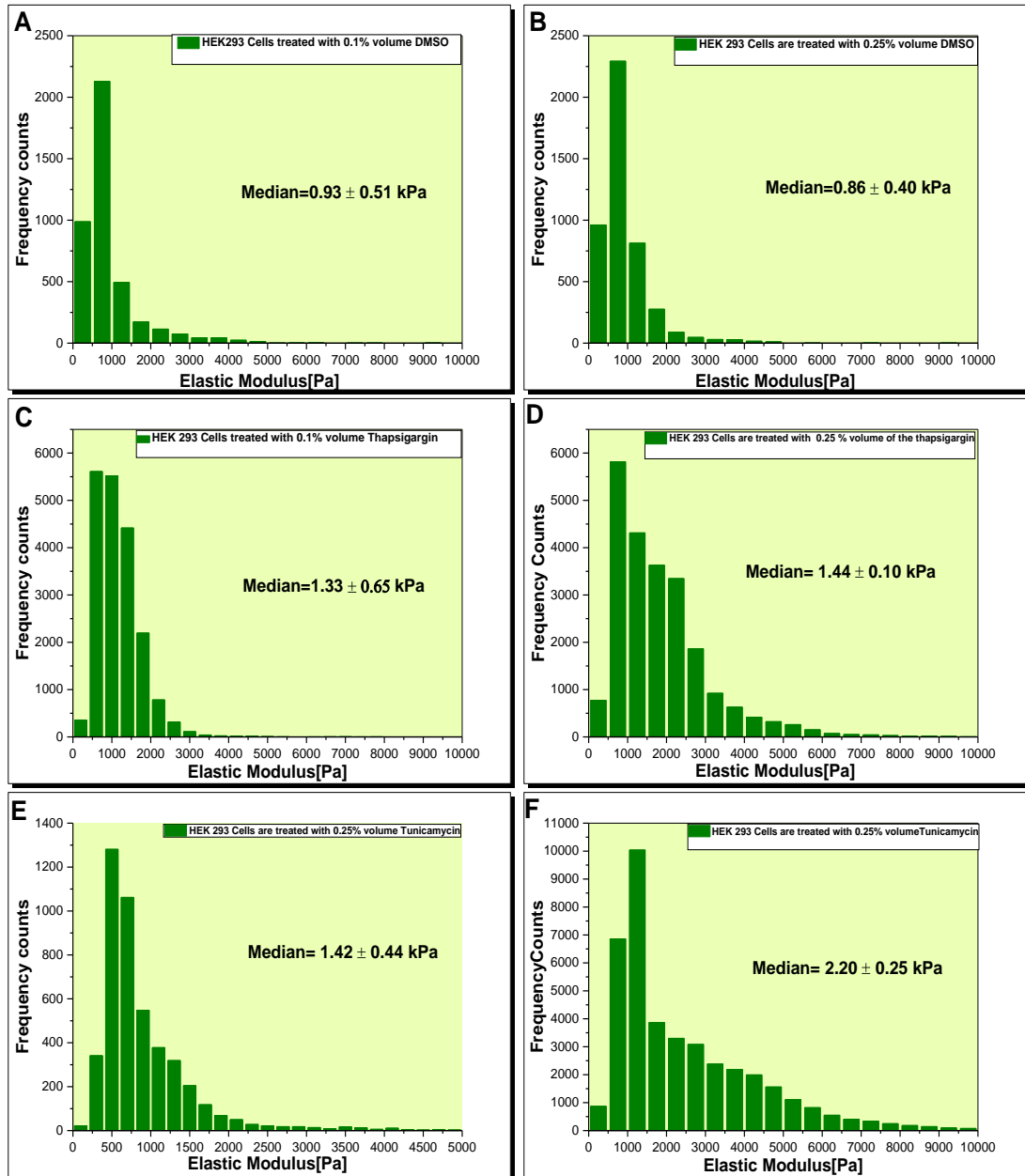


Figure 1-20: The histograms represent effects doses of Pharmaceutical inducers on the elasticity modulus of the nuclear zone of HEK293 cells. (A) represent the histogram of Young's modulus of the nuclear zone of HEK293 cells treated with 0.1% of DMSO (negative control) compared with Young's modulus of the nuclear zone of HEK293 cells treated with 0.1% volume of Thapsigargin and Tunicamycin (positive control) (C and E). While (B) represents the histogram of Young's modulus of the nuclear zone of HEK293 cells treated with 0.25% volume of DMSO (negative control) compared with Young's modulus of the nuclear zone of HEK293 cells treated with a high dose of Thapsigargin and Tunicamycin (positive control) (D and F). Both volumes of Thapsigargin and Tunicamycin displayed a high elastic modulus.

Finally, to assess differences in mechanical responsiveness of the nuclear zone of HEK293 cells, we combined all the data for each concentration into a single averaged value which represent the median of Young's modulus of the effects response to Thapsigargin, Tunicamycin and DMSO (Table2). It can also be accomplished in a rapid diagnostic test. When we performed a Mann–Whitney U analysis of these data, the nuclear zone of HEK293 cells did not show significant effects with either DMSO concentrations, which are used as a negative control. As for the Pharmaceutical inducer agents, the nuclear zone of HEK293 cells was affected by Thapsigargin and Tunicamycin, which show a strong effect. So, all those inducers exhibited significant statistical less than 0.05 (Table1-3). So, we can conclude that the nuclear zone of HEK293 cells treated with pharmaceutical inducers agents was significantly stiffer than the nuclear zone of HEK293 cells treated with DMSO, while there were no significant (ns) differences between the 0.1% and 0.25% volumes of the same agents as in (Fig. 1-21 and 1-22).

Table 1-2: Young's modulus measured by AFM on top of HEK293 cells treated with 0.1% and 0.25% volumes of pharmaceutical inducers. Values refer to the average medain \pm and the standard deviation (SD) over n cells.

| Substances | (n) | Young's modulus(kPa) Medain \pm SD (0.1% volume) | Young's modulus(kPa) Medain \pm SD (0.25% volume) |
|---------------------|------------|--|---|
| DMSO | 11 | 0.93 \pm 0.51 | 0.86 \pm 0.40 |
| Thapsigargin | 16 | 1.33 \pm 0.65 | 1.44 \pm 0.10 |
| Tunicamycin | 13 | 1.42 \pm 0.44 | 2.20 \pm 0.20 |

Table 1-3: Mann–Whitney U test results to compare nucleus stiffness of both volumes (0.1% and 0.25%) between DMSO, Thapsigargin, and Tunicamycin. Results represent two independent experiments. ns, not significant.

| <i>Comparison (0.1% volume)</i> | | <i>p-value</i> | <i>Comparison (0.25% volume)</i> | | <i>p-value</i> |
|---------------------------------|--|---------------------|--|--|--------------------|
| 1 | <i>DMSO versus Thapsigargin</i> | <i>p < 0.01</i> | <i>DMSO versus Thapsigargin</i> | | <i>p < 0.01</i> |
| 2 | <i>DMSO versus Tunicamycin</i> | <i>p < 0.006</i> | <i>DMSO versus Tunicamycin</i> | | <i>p < 0.04</i> |
| 3 | <i>Thapsigargin versus Tunicamycin</i> | <i>(ns)</i> | <i>Thapsigargin versus Tunicamycin</i> | | <i>(ns)</i> |

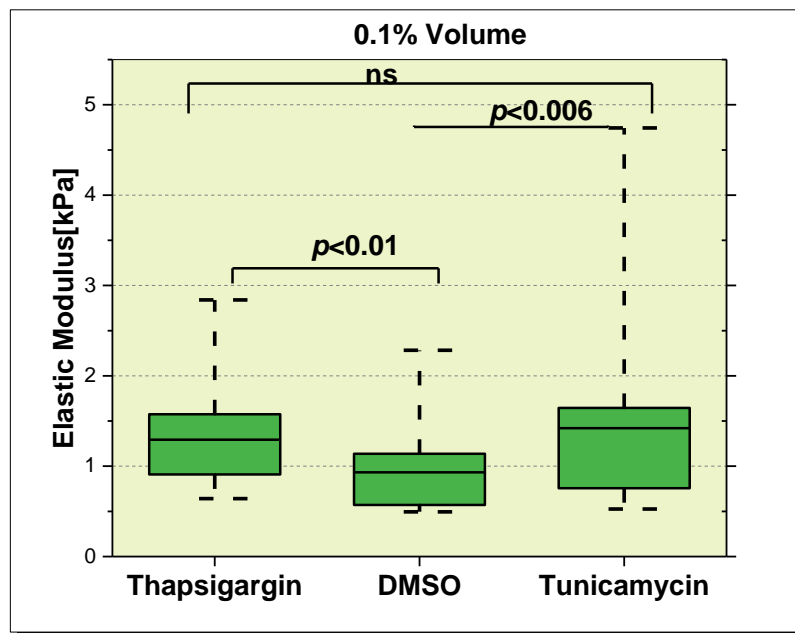


Figure 1-21: Box plot represents elastic responses of the nuclear area of HEK293 cells following treatment with a low volume of 0.1% Thapsigargin and Tunicamycin and compare them with DMSO. Results represent three independent experiments. ns, not significant.

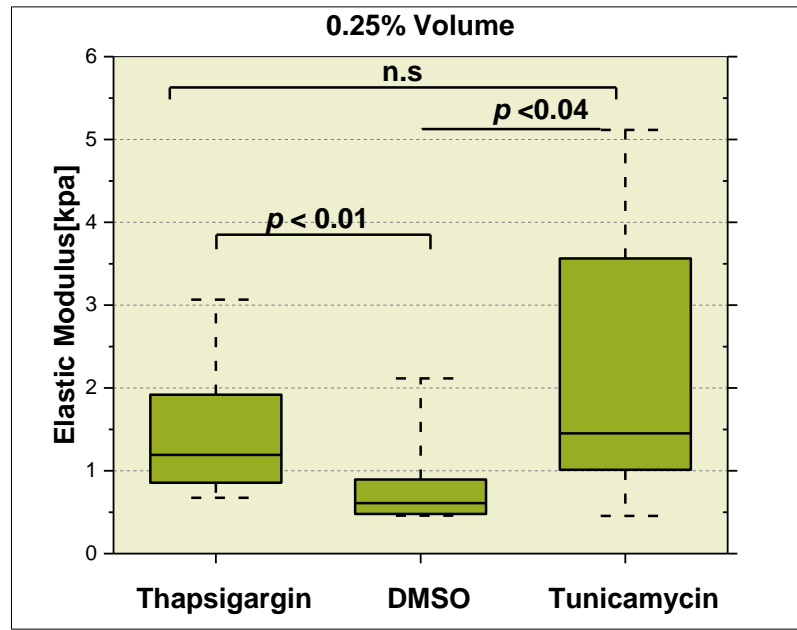


Figure 1-22: Box plot of elastic responses of the nuclear zone of HEK293 cells following treatment with a high volume of 0.25% of Thapsigargin and Tunicamycin comparing them with DMSO. Results represent three independent experiments. ns, not significant.

1.3.3 Stiffness distributions of the fluorescent HEK293 cell line

To evaluate the direct contribution of the mutation TMEM43-p.S358L on the elasticity of the nuclear zone of cells, we generated HEK293 cell lines expressing the GFP-tagged wild-type TMEM43 (TMEM43-WT) and GFP-tagged TMEM43-p.S358L mutation. Fluorescence, as could express the GFP-tagged wild-type without TMEM43, has been used as a negative control. We performed AFM nano-indentation in which, the images are made up of a bright-field image; fluorescence image, topography image and a force map showing retract stiffness data which is proportional to the elastic modulus (Fig.1-23). According to the previous experiment, both the elasticity and topography images have an identical scale, that's, in turn, helped us to compare all results of stiffness for all samples.

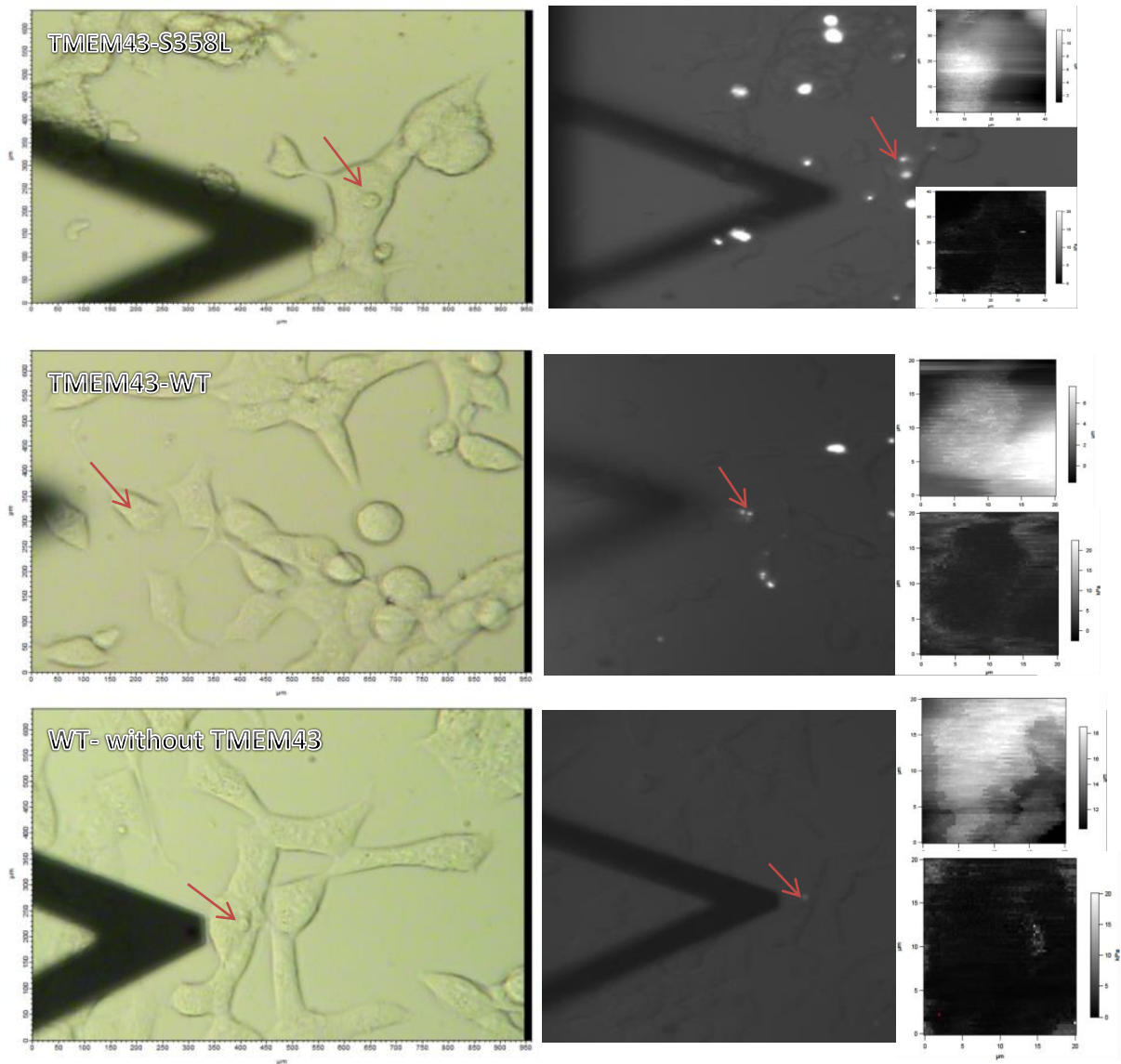


Figure 1-23: AFM images of HEK293 cells transfected with (TMEM43-S358L), (TMEM43-WT) and (WT- without TMEM43), force curve velocity 3.00 $\mu\text{m/s}$, force curve rate 1.5 Hz, 64 pixels \times 64 force curves. Data acquisition time was 60 min. After the AFM experiment, elasticity maps corresponding to possess differences in Young's moduli. The arrow indicates the nucleus

To minimize the impact of cell morphology in each adherent cell, we placed the AFM tip at the centre of the single-cell surface. After obtaining the force curves at the nuclear zone of the transfected HEK293 cells, the histogram (Fig. 1-24) of Young's modulus calculated from the force curves showed that the nuclear zone of (GFP-TMEM43-S358L) showed an increased stiffness compared to TMEM43-WT and WT- without TMEM43 transfection, where the GFP-TMEM43-S358L values were (1.3 ± 0.61 kPa), while GFP-TMEM43-WT and GFP-WT- without TMEM43 values were (0.69 ± 0.4 kPa) and (0.85 ± 0.2 kPa) respectively (Table 1-4).

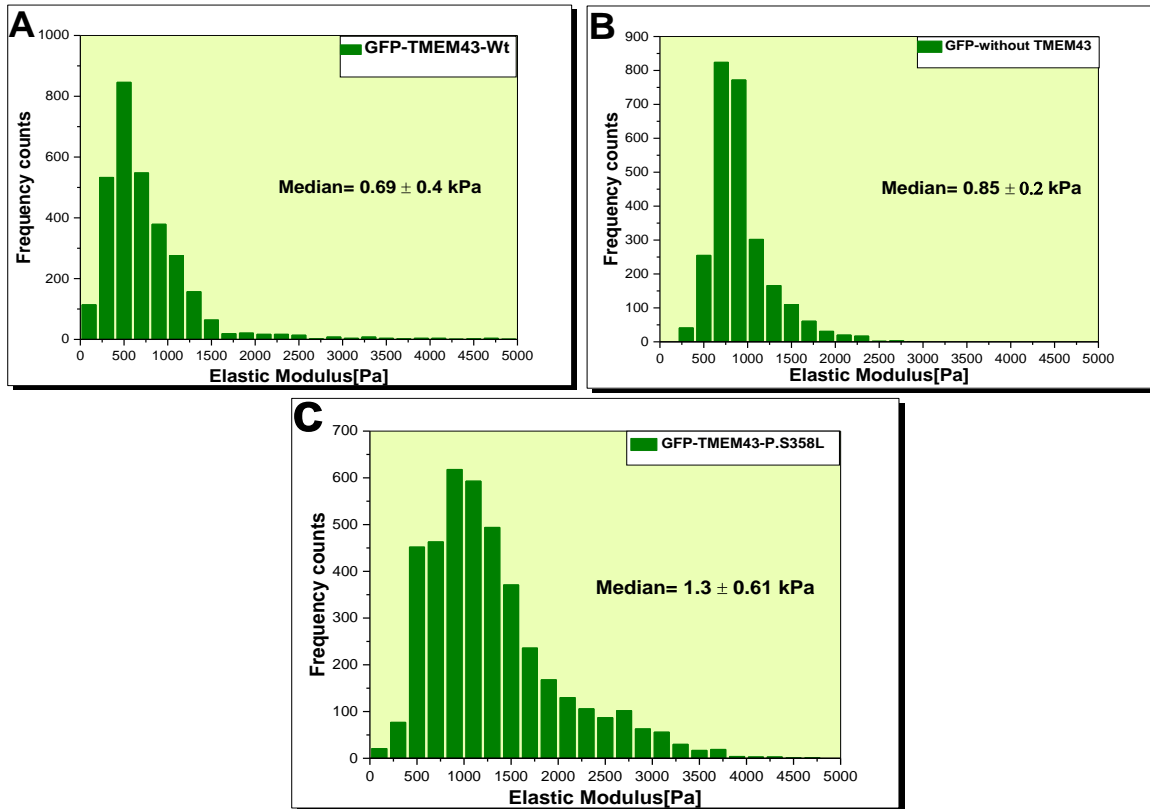


Figure1-24: The histograms present the elasticity distributions of the nuclear area in the fluorescent HEK293 cell line, (A) represents Young's modulus histogram of the wild-type (GFP-TMEM43-WT), (B) represent Young's modulus histogram of the negative control (GFP-without-TMEM43), (C) represent Young's modulus histogram mutant (GFP-TMEM43- p.S358L). The TMEM43-S358L cell displays a high elastic modulus.

Table 1-4: Young's modulus measured by AFM on top of the transfected HEK293 cells. Values refer to the average median \pm and the standard deviation (SD) over n cells.

| Groups | n | Young's modulus(kPa) Medain \pm SD |
|---------------------|----|---|
| GFP-TMEM43- p.S358L | 13 | 1.3 \pm 0.61 |
| GFP-TMEM43-WT | 12 | 0.69 \pm 0.4 |
| GFP-without-TMEM43 | 12 | 0.85 \pm 0.2 |

To further evaluate these differences. We incorporated all the data for each different cell type into a single averaged value (median \pm standard deviation (SD) for each control, as

might be done in a fast diagnostic test. When we completed a Mann–Whitney U test analysis of these data, the nuclear zone of the transfected HEK293 (TMEM43-S358L) cells exhibited significantly different stiffness values than the nuclear zone of the transfected HEK293 cell (TMEM43-WT) and (WT-without TMEM43) cells (Figure25). These differences were statistically significantly less than 5% while the nuclear zone of the transfected HEK293 (TMEM43-WT) cells did not show significance when we compared the nuclear zone of the transfected HEK293 (WT- without TMEM43) cells. These differences were significant statistical significant greater than 5%, as shown in table 5.

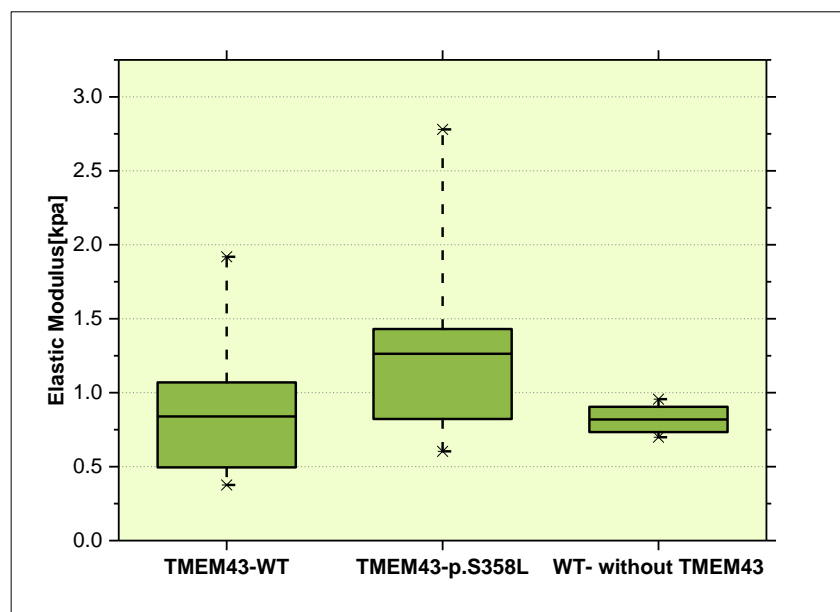


Figure 1-25: Box plots of the elastic responses of the nuclear area of GFP-TMEM43-p.S358L HEK293 cells.

Table 1-5: Mann–Whitney U test results for a comparison of the stiffness of different cell types. Results represent three independent experiments. ns, not significant.

| <i>Comparison</i> | | <i>p-value</i> |
|-------------------|---|---------------------|
| 1 | <i>GFP-TMEM43-S358L versus TMEM43-WT</i> | <i>P < 0.006</i> |
| 2 | <i>GFP-TMEM43-S358L versus WT- without TMEM43</i> | <i>P < 0.04</i> |
| 3 | <i>TMEM43-WT versus WT- without TMEM43</i> | <i>(ns)</i> |

1.4 Discussion

1.4.1 Effect of TMEM43 mutation on entire cell elasticity

The p.S358L point mutation occurs due to the exchange of the residue Serine 358 to a Leucine residue (S358L) in the third TM domain of the TMEM43 protein. This protein mutation is linked with ARVD5, which is a unique type of ARVD (Baskin et al. 2013). Many data proved that the TMEM43 protein is anchored at the inner nuclear envelope and endoplasmic reticulum (Rajkumar et al. 2012). At the inner nuclear membrane, the TMEM43 protein plays an important role in maintaining of nuclear envelope structure by organizing molecular complexes with proteins in INM, including lamins A/C, B1, emerin (Emery-Dreifuss muscular dystrophy [EMD]) and SUN2 (SUN domain-containing protein) (Liang et al. 2011; Stroud et al. 2014). Therefore, TMEM43 is part of the 'linkers of the nucleoskeleton and cytoskeleton complex' (LINC) (Stroud et al. 2014; Stroud 2018). Newly, research has shown that the mutations in genes coding for nuclear envelope proteins, which are physically related between the nucleoskeleton and the cytoskeleton, are resulting in disorganization mechanical of the nuclear envelope and cytoplasm, thus the entire cell (Stroud 2018). Milting et al (2015) proved that the p.S358L point mutation in TMEM43 negatively effect of the nuclear mechanics, while Thomas et al (2013) demonstrated that the mechanical effect of lamina mutation was not to limited nuclear mechanics, but rather extended to the biomechanics of the entire cell. So, all these evidence might provide us with novel insights to the underlying mechanisms behind evolution ARVD5 disease, via understanding the impacts the TMEM43 mutation on the mechanical properties of the whole cell.

In this study, a Green fluorescent protein (GFP) was used as a tag for constructs consisting of full-length wild-type (GFP-TMEM43-WT), mutant (GFP-TMEM43-pS358L) TMEM43 to generate stable transfected HeLa cell. The combination AFM and fluorescent samples could add complementary information, which is of great significance for us to open a new horizon to study the underlying mechanisms that regulate the structure and mechanics of living cells through cellular and physiological activities (Chatterjee et al. 2014). Force curves were obtained to extract the elastic moduli (Young's moduli) of different regions at the cell surface (Fig.1-13 and 1-14). Hertz's model was used to fit the nuclear region of the force curve in resulting elastic moduli. Our data indicate that the HeLa cell carrying GFP-TMEM43-pS358L has an

increase in the Young modulus inside the nucleus compared to control (7.3 ± 6.0 kPa versus 2.3 ± 1.4 kPa with $p < 0.01$) (Fig. 1-16 and table1-1). These values are compatible with the range of other reported measurements (Milting et al. 2015). Padrón-Barthe et al (2019) confirmed that the p.S358L point mutation cause distorted on the 3D structure of TMEM43 protein, disrupting the interaction with his partners. Therefore, any increase in the nuclear stiffness could result from the progressive accumulation of TMEM43 mutation as misfolded protein over time (Milting et al. 2015; Siragam et al. 2014). At the nuclear periphery, the TMEM43-pS358L cause's dysfunction of the emerin, which, in turn, leads to blocking the reaction with the A and C type lamins (Padrón-Barthe et al. 2019). In this way, TMEM43 mutation cause disorder in the functionality of its binding partners, which results in the disturbance of nuclear mechanics (Liang et al. 2011; Milting et al. 2015). Thus, the ability to rearrange the lamina under mechanical stress is reduced (Padrón-Barthe et al. 2019). Moreover, our results showed that the effect of the TMEM43-pS358L was extended to the cytoplasm region, hence the entire cells. These results showed a noticeable increase in the Young modulus values, where the values of the cytoplasm region were (8.9 ± 7.1 kPa versus 2.4 ± 0.7 kPa with $p < 0.02$) (Fig. 1-17 and table1-1), while the values of the entire cells were (7.8 ± 6.4 kPa versus 1.8 ± 0.9 kPa with $p < 0.02$) (Fig. 1-15 and table1-1). The high stiffness of the cytoplasm region and entire cells may be attributed to direct mechanical connections between the nucleus and cytoskeleton, which are affected during alterations in the nuclear envelope (Donnaloja et al. 2019). Indeed, the actin cytoskeletal associated with the nuclear envelope shows a direct connection between the nuclear interior and the ECM (Jorgens et al. 2017). The cell is linked to ECM by integrins at a specific site named focal adhesions. These focal adhesions are in turn linked inside the cell to many actin-binding proteins such as talin, and vinculin, which are linked to the actin cytoskeleton. All these connections contribute to the transmission of mechanical signals from the nucleus to the ECM or vice versa (Zemel 2015). So, these connections play an accurate and integrated role in cellular mechanical sensitization and the mechanical response (Uzer et al. 2016). The mechanical stress caused by force applied to the cell membrane (integrin) is transmitted from the actin stress fibers to the nucleus via the LINC complexes, resulting in (intra-) nuclear disruption (Isermann and Lammerding 2013). Thus, distortions nuclear mechanics accompanying cytoskeletal remodelling results in changes in gene expression, by interactions with members of mechanosensitive signalling (Thorpe and Lee 2017). In accordance with this, the

accumulation of TMEM43 mutation was shown to be perturbing for the LINC complexes. For instance, the excessive expression TMEM43 mutation leads to reduces interaction with the cytoskeleton and cytoskeleton-interacting proteins such as actin, and myosin (Padrón-Barthe et al. 2019). These events lead to the activation of the transcription factors NF- κ B, (Zheng et al. 2019). After activation, the NF- κ B is allowed to translocate to the nucleus and activating its target gene transcription (Kustermans et al. 2005). The anomalous NF- κ B signal enhances the cytokine transforming growth factor-beta (TGF β) signalling, which is responsible for increasing fibrosis level in many various cells and tissues (Chávez et al. 2012). Once released, the TGF- β 1 stimulates a high level of collagen I, which leads to an increase in stiffness the ECM (Johnston and Gillis 2017). Padrón-Barthe et al (2019) proved that the TMEM43 mutation increases the collagen and elastin levels. Stress and ECM stiffness increase the level of lamin A/C to keep the nucleus stable (Swift et al. 2013). Here, our results proposed a new concept about potential mechanisms responsible for the evolution ARVD5, and show that the biomechanical effects of TMEM43 mutation not only affect nuclear mechanics but extends to include of the entire cell biomechanical properties.

1.4.2 ER stress affects cell nucleus elasticity

Homeostasis is defined as the ability to preserve a constant internal physical and chemical environment in response to environmental changes. The effective cellular homeostasis is achieved by the regulated protein turnover machinery; meaning that any interference with this system produces cellular stress and changes the normal functioning of proteins significant for cell survival (Jaalouk and Lammerding 2009; Kolahi and Mofrad 2010). It is well known the ER plays a decisive role in folding and maturation of newly synthesized secretory and transmembrane proteins and in maintaining calcium homeostasis (Amen et al. 2019). Nevertheless, several of these proteins become unfolded or misfolded upon exposure to stimuli, including disturbance of calcium homeostasis and overexpression of pathogenic mutant proteins. These proteins possess a tendency to interact and aggregate in the cell, resulting in toxic species that trigger ERS (Díaz-Villanueva et al. 2015; Shacham et al. 2019). The ERS regulated by three ER transmembrane stress sensors, including inositol-requiring enzyme 1 α (IRE1 α), pancreatic endoplasmic reticulum kinase (PERK) and activating transcription factor 6 (ATF6) (Hetz and Papa 2018). All of the three sensors are activated through dissociation with GRP78 upon there is an overexpression of

misfolded proteins and chaperones (Timberlake, II and Dwivedi 2019) and, therefore induce of the unfolded protein response (UPR). In fact, the cells are sensitive to cellular stress by mechanotransduction. These mechanical stimuli provide a clear description of the cellular processes that leads to translate mechanical stress into biochemical signals, for example, specific intracellular changes (e.g., calcium depletion or activation of various signaling pathways) (Muhamed et al. 2017). These mechanosensitive feedbacks are vital to maintain or restore cellular homeostasis. Thus, these signals can modify the cellular structure to their physical environment (Jaalouk and Lammerding 2009). Accumulating evidence implicates that the disruption of the ER has been associated with numerous human genetic diseases such as neurodegenerative (notably Alzheimer's and Parkinson's), and dilated cardiomyopathy (DCM) disease (Scheper and Hoozemans 2015). That evidences encouraged us to take a closer look for probability the effect of ER stress on the mechanical properties of cells.

In order to make a quantitative explanation of the impact of ERS on the stiffness of the nuclear area of the HEK293 cells, we stimulated ERS using two inducers namely thapsigargin TG (1 $\mu\text{g/ml}$); an inhibitor of sarcoplasmic/endoplasmic reticulum Ca^{2+} ATPases which pump Ca_2^+ into the ER and tunicamycin TUN (2 $\mu\text{g/ml}$), an inhibitor of N-linked protein glycosylation. Indeed, several data have shown that TG and TUN agents induce ERS during the six hours incubation time. Long-term exposure often induces ER stress-mediated cell death (Oslowski and Urano 2011; Abdullahi et al. 2017). This may explain the non-change of the cell morphology after the stimulation of the ERS (Fig.1-19). Also, the application of TG and TUN in a time- and dose-dependent manner stimulate ER stress-mediated cell death (Ogata et al. 2006). In the AFM indentation experiments, all changes in the cell's elasticity were monitored under pharmacological agents TG and TUN. Figure (1-20 A,B,C,D and table 1-3) shows a significant increase in the stiffness of the nuclear area of the HEK293 cells in both TG volumes compared to cells treated with DMSO respectively; 0.1% (1.33 ± 0.65 kPa versus 0.93 ± 0.51 kPa with $p < 0.01$) and 0.25% (1.44 ± 0.10 versus 0.86 ± 0.40 kPa with $p < 0.01$). As for TM, our results of HEK293 cell elasticity examination indicated that the treatment with both volumes 0.1% (1.42 ± 0.44 kPa versus 0.93 ± 0.51 kPa with $p < 0.006$) and 0.25% (2.20 ± 2.58 kPa versus 0.86 ± 0.40 kPa with $p < 0.04$) showed high-level stiffness compared to the control (DMSO) (Fig. 1-20 A,B,E,F and table 1-3). In brief, the stiffness significantly increased after six hours the TG and the TM treatments, which imply that the nuclear zone of HEK293 cells became much stiffer

after inducing the ERS. These results may be attributed to the (UPR) stress response that is responsible for inducing the cellular mechanisms to pro-survival and/or to pro-apoptotic (Iurlaro and Muñoz-Pinedo 2016). Mostly, the fate of the stressed cell is determined through the interplay between these responses (Samali et al. 2010). If ERS is unresolved, the UPR signalling switches from pro-survival to pro-apoptotic (Rozpedek et al. 2016). Several researches have shown that the changes in cell stiffness (elastic modulus) are closely related to the progression of cell death-like apoptosis (Pelling et al. 2009). This also includes the dynamic changes in the cytoskeleton and the nucleus. Indeed, the cytoskeleton is connected to the nucleus by a linker of the previously mentioned (Hohmann and Dehghani 2019). A number of studies have proved that this link supports the mechanical stability of the nucleus via the stiffening of the nucleus to reduce nuclear distortion (Cho et al. 2017). Therefore, we tentatively propose the UPR response activate the pro-apoptotic signalling to resolves ERS. Previous surveys confirmed that the ERS stimulates pro-apoptotic signalling by overexpression C/EBP homologous protein (CHOP) and GRP78 (Hu et al. 2018). The researchers checked the time it takes for TG and TUN agents to stimulate apoptosis. They found that TG induces the early apoptosis by increased the levels of GRP78 and CHOP after 2 h of treatment, while the TUN increased the levels of GRP78 and CHOP after 4-8 h (Matsumoto et al. 2013; Krajarng et al. 2015). The programmed cell death (or apoptosis) process is known to indicate dramatic changes in cell shape and organization, which allows the transfer of signaling molecules between intracellular organelles (Elmore 2007). In addition, the apoptosis process coordinates a set of complex biochemical and the structural events resulting in abnormalities in the cell. Hence, it changes the elastic modulus of the cells (Taylor et al. 2008). Several current studies have focused on the cellular stiffness changes during progression pro-apoptotic, which was stimulated by the chemotherapy and drug treatment. Pelling et al (2009) reported that the cellular elastic modulus increase during early-stage apoptosis, Ambriz et al (2018) observed that the amount of stiffness relies on actin and its arrangement at the mesh layer of the cytoskeletal structure. All these finding have shown that the dynamic mechanical alterations are related with perturbation of the linker of nucleoskeleton, cytoskeleton and also timescales with apoptosis progresses. The dynamic alternations events are strictly organized, forming connect between cell molecular biology and the physical microenvironment (Pelling et al. 2009). A defect of mechanical regulation during early-apoptotic cause increase stiffness values. This may

be due to relate between the cytoskeleton and nucleus that help reduce distortion through minimize the risk of genetic instability (Wang et al. 2018).

Here, we were encouraged by the above results to make new propose about pathophysiological mechanisms of the TMEM43 Ser358Leu mutation. This hypothesis suggests an unanticipated new regulatory mechanism that combines TMEM43 mutation with ERS and signaling pathways. In order to make better comparisons, we used the HEK293 cells as a model system; it is the same model used by the above experiments. To test this hypothesis, we generated transfection constructs encoding missense of TMEM43 mutant proteins, wild type of TMEM43 protein, and wild type without TMEM43 fused to GFP. In our elasticity experiments, the mutant (GFP-TMEM43-S358L) group show a high significant stiffness rates compare with the control groups (GFP-TMEM43-WT) (1.3 ± 0.6 versus 0.86 ± 0.2 , $p < 0.006$), and (GFP-WT-without TMEM43) (1.3 ± 0.6 versus 0.69 ± 0.3 , $p < 0.04$, Fig. 1-24 and table 1-5). Once again, our results are consistent with others (Milting et al. 2015), but it is interesting the absence TMEM43 protein did not affect cellular function, as our experiments did not record a change in the rate of nuclei stiffness versus TMEM43-wild type (0.86 ± 0.2 versus 0.69 ± 0.3 , ns) (Fig. 1-24 and table 1-5). This may be because that the localization and levels of LINC complex proteins interacting with TMEM43 protein have not been affected. Thus, the LINC complex proteins work synergistically to compensate for the absence of TMEM43 protein and maintain cellular homogeneity (Stroud 2018). This is undoubted evidence that the p.S358L mutant of TMEM43 cause cellular homeostasis disorder. Newly, wide attentions have been paid to the crosstalk that occurs between the p.S358L mutant of TMEM43 and signalling pathways, which in turn may stimulate ERS. As we mentioned earlier, the overexpression of the TMEM43 mutation activates cascades of the mechanosensitive signaling, including NF- κ B, which activates the TGF β signaling pathway (Jiang et al. 2017; Zheng et al. 2019) The high levels of TGF β contribute to stimulating ERS. Factually, this signaling causes an excessive overload of ECM proteins to the endoplasmic reticulum (ER), resulting in trigger the unfolded protein response (UPR) (Liu et al. 2019). It is well known that the AKT signaling pathway is a signal transduction pathway, which plays a key role in support cell survival in response to extracellular signals (Shi et al. 2019). Recently by Padr3n-Barthe et al (2019) demonstrated that the overexpression of the TMEM43 S358L mutation causes a malfunction in the AKT signaling pathway, consequently

leads to activation the glycogen synthase kinase-3 β (GSK3 β). In turn, GSK3 β promotes up-regulation of CHOP that contributes to stimulating ER stress-induced apoptosis (Osowski and Urano 2011). So, our observations strongly suggest that TMEM43-S358L is a deleterious mutation that causes ER stress by stimulating aberrant signals. As a result, pro-apoptotic signals are stimulated and followed by fibrotic replacement, which leads to passive stiffness (Zheng et al. 2019). All these notes highlight the functional impact of TMEM43-S358L in the evolution of ARVC5 as well as the implicit molecular regulatory processes.

1.5 Conclusions & Outlooks

1.5.1 Conclusions

In summary, our data presented in this study showed the following:

1. The TMEM43-S358L mutation affect the stability of the cells due to reduced interaction between the nucleus and the cytoskeleton, which is contributing to cell death under biomechanical stress.
2. The cells treated with pharmacological agents TG and TUN to stimulate ERS revealed a significant increase in the stiffness of the nucleus. This may be attributed to an increase of the intracellular hemostasis tension and then followed by a change in physical activity to protect the nucleus. If ERS is unresolved, the UPR signaling switches from pro-survival to pro-apoptotic.
3. The absence of the TMEM43 protein did not affect the nanomechanical properties of the nucleus. Actually, this may be due to the synergistic work of the LINC complex proteins to compensate for the absence of the TMEM43 protein and maintain cellular homogeneity.

In summary, the p.S358L mutant of TMEM43 caused disorder in cytoskeletal architecture and modulation of cellular elasticity, thus corruption to mechanically-derived signals, which is usually, transmitted through the ECM proteins. These signals stimulate excessive expression of ECM proteins to the endoplasmic reticulum (ER), resulting in unfolded protein response (UPR). Here, the ER stress could be regarded as a reasonable mechanism leading to contribute to pathological mechanisms of the ARVC5.

1.5.2 Outlook

With the findings above, there will be more insights to explain the impact of the TMEM43 mutation depending on cross-talk between the mechanical stress and gene expression, which induce ER stresses and thus stimulating cell death programs. So, exciting questions linking pathogenic evolution of a TMEM43 mutation, ER stress and cellular mechanics are open for discussion.

References

- **Abdullahi**, Abdikarim; Stanojcic, Mile; Parousis, Alexandra; Patsouris, David; Jeschke, Marc G. (2017): Modeling Acute ER Stress in Vivo and in Vitro. In *Shock (Augusta, Ga.)* 47 (4), pp. 506–513. DOI: 10.1097/SHK.0000000000000759.
- **Akhmanova**, Anna; Mausset-Bonnefont, Anne-Laure; van Cappellen, Wiggert; Keijzer, Nanda; Hoogenraad, Casper C.; Stepanova, Tatiana et al. (2005): The microtubule plus-end-tracking protein CLIP-170 associates with the spermatid manchette and is essential for spermatogenesis. In *Genes & Development* 19 (20), pp. 2501–2515. DOI: 10.1101/gad.344505.
- **Alberts**, B., Johnson, A., Lewis, J., Raff, M., Roberts, K. and Walter, P. (2003): Molecular biology of the cell. 4th edn. In *Annals of Botany* 91 (3), p. 401. DOI: 10.1093/aob/mcg023.
- **Aliano**, Antonio; Cicero, Giancarlo; Nili, Hossein; Green, Nicolas G.; García-Sánchez, Pablo; Ramos, Antonio et al. (2012): Atomic Force Microscopy. In Bharat Bhushan (Ed.): *Encyclopedia of nanotechnology*. Dordrecht, London: Springer (Springer reference), pp. 146–160.
- **Al-Jassar**, Caesar; Bikker, Hennie; Overduin, Michael; Chidgey, Martyn (2013): Mechanistic basis of desmosome-targeted diseases. In *Journal of Molecular Biology* 425 (21), pp. 4006–4022. DOI: 10.1016/j.jmb.2013.07.035.
- **Allison**, David P.; Mortensen, Ninell P.; Sullivan, Claretta J.; Doktycz, Mitchel J. (2010): Atomic force microscopy of biological samples. In *Wiley interdisciplinary reviews. Nanomedicine and nanobiotechnology* 2 (6), pp. 618–634. DOI: 10.1002/wnan.104.
- **Ambriz**, X.; Lanerolle, P. de; Ambrosio, J. R. (2018): The Mechanobiology of the Actin Cytoskeleton in Stem Cells during Differentiation and Interaction with Biomaterials. In *Stem cells international* 2018, p. 2891957. DOI: 10.1155/2018/2891957.
- **Amen**, Omar Mohammed; Sarker, Satyajit D.; Ghildyal, Reena; Arya, Aditya (2019): Endoplasmic Reticulum Stress Activates Unfolded Protein Response

- Signaling and Mediates Inflammation, Obesity, and Cardiac Dysfunction: Therapeutic and Molecular Approach. In *Frontiers in pharmacology* 10, p. 977. DOI: 10.3389/fphar.2019.00977.
- **Bártová**, Eva; Krejčí, Jana; Harnicarová, Andrea; Galiová, Gabriela; Kozubek, Stanislav (2008): Histone modifications and nuclear architecture: a review. In *Journal of Histochemistry and Cytochemistry* 56 (8), pp. 711–721. DOI: 10.1369/jhc.2008.951251.
 - **Baskin**, Berivan; Skinner, Jon R.; Sanatani, Shubhayan; Terespolsky, Deborah; Krahn, Andrew D.; Ray, Peter N. et al. (2013): TMEM43 mutations associated with arrhythmogenic right ventricular cardiomyopathy in non-Newfoundland populations. In *Human genetics* 132 (11), pp. 1245–1252. DOI: 10.1007/s00439-013-1323-2.
 - **Bianchi**, Andrea; Manti, Pierluigi Giuseppe; Lucini, Federica; Lanzaolo, Chiara (2018): Mechanotransduction, nuclear architecture and epigenetics in Emery Dreifuss Muscular Dystrophy: tous pour un, un pour tous. In *Nucleus* 9 (1), pp. 276–290. DOI: 10.1080/19491034.2018.1460044.
 - **Binnig**, G.; Quate, C. F.; Gerber, Ch. (1986): Atomic Force Microscope. In *Phys. Rev. Lett.* 56 (9), pp. 930–933. DOI: 10.1103/PhysRevLett.56.930.
 - **Binnig**, G.; Rohrer, H.; Gerber, Ch.; Weibel, E. (1982): Surface Studies by Scanning Tunneling Microscopy. In *Phys. Rev. Lett.* 49 (1), pp. 57–61. DOI: 10.1103/PhysRevLett.49.57.
 - **Bowen**, W. Richard; Hilal, Nidal (2009): Atomic force microscopy in process engineering. Introduction to AFM for improved processes and products / [edited by] W. Richard Bowen and Nidal Hilal. Oxford, Burlington, MA: Butterworth-Heinemann (Butterworth-Heinemann/ICHEM series).
 - **Bravo**, Roberto; Parra, Valentina; Gatica, Damián; Rodríguez, Andrea E.; Torrealba, Natalia; Paredes, Felipe et al. (2013): Endoplasmic reticulum and the unfolded protein response: dynamics and metabolic integration. In *International review of cell and molecular biology* 301, pp. 215–290. DOI: 10.1016/B978-0-12-407704-1.00005-1.

- **Buchwalter**, Abigail; Schulte, Roberta; Tsai, Hsiao; Capitanio, Juliana; Hetzer, Martin (2019): Selective clearance of the inner nuclear membrane protein emerin by vesicular transport during ER stress. In *eLife* 8. DOI: 10.7554/eLife.49796.
- **Burrige**, Keith; Guilluy, Christophe (2016): Focal adhesions, stress fibers and mechanical tension. In *Experimental cell research* 343 (1), pp. 14–20. DOI: 10.1016/j.yexcr.2015.10.029.
- **Carmosino**, Monica; Gerbino, Andrea; Schena, Giorgia; Procino, Giuseppe; Miglionico, Rocchina; Forleo, Cinzia et al. (2016): The expression of Lamin A mutant R321X leads to endoplasmic reticulum stress with aberrant Ca²⁺ handling. In *Journal of Cellular and Molecular Medicine* 20 (11), pp. 2194–2207. DOI: 10.1111/jcmm.12926.
- **Chang**, Kai-Chih; Chiang, Yu-Wei; Yang, Chin-Hao; Liou, Je-Wen (2012): Atomic force microscopy in biology and biomedicine. In *Tzu Chi Medical Journal* 24 (4), pp. 162–169. DOI: 10.1016/j.tcmj.2012.08.002.
- **Chatterjee**, Susmita; Biswas, Nupur; Datta, Alokmay; Dey, Rupali; Maiti, Prasantakumar (2014): Atomic force microscopy in biofilm study. In *Microscopy (Oxford, England)* 63 (4), pp. 269–278. DOI: 10.1093/jmicro/dfu013.
- **Chávez**, E.; Castro-Sánchez, L.; Shibayama, M.; Tsutsumi, V.; Moreno, M. G.; Muriel, P. (2012): Sulfasalazine prevents the increase in TGF- β , COX-2, nuclear NF κ B translocation and fibrosis in CCl₄-induced liver cirrhosis in the rat. In *Human & experimental toxicology* 31 (9), pp. 913–920. DOI: 10.1177/0960327112438928.
- **Cheng**, Bo; Lin, Min; Huang, Guoyou; Li, Yuhui; Ji, Baohua; Genin, Guy M. et al. (2017): Cellular mechanosensing of the biophysical microenvironment: A review of mathematical models of biophysical regulation of cell responses. In *Physics of life reviews* 22-23, pp. 88–119. DOI: 10.1016/j.plrev.2017.06.016.
- **Cho**, Sangkyun; Irianto, Jerome; Discher, Dennis E. (2017): Mechanosensing by the nucleus: From pathways to scaling relationships. In *The Journal of Cell Biology* 216 (2), pp. 305–315. DOI: 10.1083/jcb.201610042.

- **Ciavarella**, M.; Joe, J.; Papangelo, A.; Barber, J. R. (2019): The role of adhesion in contact mechanics. In *Journal of the Royal Society, Interface* 16 (151), p. 20180738. DOI: 10.1098/rsif.2018.0738.
- **Cleveland**, J. P.; Anczykowski, B.; Schmid, A. E.; Elings, V. B. (1998): Energy dissipation in tapping-mode atomic force microscopy. In *Appl. Phys. Lett.* 72 (20), pp. 2613–2615. DOI: 10.1063/1.121434.
- **Codan**, B.; Del Favero, G.; Martinelli, V.; Long, C. S.; Mestroni, L.; Sbaizero, O. (2014): Exploring the elasticity and adhesion behavior of cardiac fibroblasts by atomic force microscopy indentation. In *Materials science & engineering. C, Materials for biological applications* 40, pp. 427–434. DOI: 10.1016/j.msec.2014.04.003.
- **Dechat**, Thomas; Adam, Stephen A.; Taimen, Pekka; Shimi, Takeshi; Goldman, Robert D. (2010): Nuclear lamins. In *Cold Spring Harbor perspectives in biology* 2 (11), a000547. DOI: 10.1101/cshperspect.a000547.
- **Díaz-Villanueva**, José Fernando; Díaz-Molina, Raúl; García-González, Victor (2015): Protein Folding and Mechanisms of Proteostasis. In *International Journal of Molecular Sciences* 16 (8), pp. 17193–17230. DOI: 10.3390/ijms160817193.
- **Dombrowski**, R. T. (2013): Microscopy techniques for analyzing the phase nature and morphology of biomaterials. In M. Jaffe, W. Hammond, P. Tolia, T. Arinzeh (Eds.): *Characterization of biomaterials*. Oxford, Philadelphia: Woodhead Publishing (Woodhead Publishing series in biomaterials, number 64), pp. 1–33.
- **Donnalaja**, F.; Jacchetti, E.; Soncini, M.; Raimondi, M. T. (2019): Mechanosensing at the Nuclear Envelope by Nuclear Pore Complex Stretch Activation and Its Effect in Physiology and Pathology. In *Frontiers in physiology* 10, p. 896. DOI: 10.3389/fphys.2019.00896.
- **Dufrêne**, Yves F.; Ando, Toshio; Garcia, Ricardo; Alsteens, David; Martinez-Martin, David; Engel, Andreas et al. (2017): Imaging modes of atomic force microscopy for application in molecular and cell biology. In *Nature nanotechnology* 12 (4), pp. 295–307. DOI: 10.1038/nnano.2017.45.

- **Elmore**, Susan (2007): Apoptosis: a review of programmed cell death. In *Toxicologic pathology* 35 (4), pp. 495–516. DOI: 10.1080/01926230701320337.
- **Essawy**, Nada; Samson, Camille; Petitalot, Ambre; Moog, Sophie; Bigot, Anne; Herrada, Isaline et al. (2019): An Emerin LEM-Domain Mutation Impairs Cell Response to Mechanical Stress. In *Cells* 8 (6). DOI: 10.3390/cells8060570.
- **Fernandez-Martinez**, Javier; Rout, Michael P. (2009): Nuclear pore complex biogenesis. In *Current opinion in cell biology* 21 (4), pp. 603–612. DOI: 10.1016/j.ceb.2009.05.001.
- **Fletcher**, Daniel A.; Mullins, R. Dyche (2010): Cell mechanics and the cytoskeleton. In *Nature* 463 (7280), pp. 485–492. DOI: 10.1038/nature08908.
- **Frank**, R.; Fontaine, G.; Vedel, J.; Mialet, G.; Sol, C.; Guiraudon, G.; Grosogeat, Y. (1978): Electrocardiologie de quatre cas de dysplasie ventriculaire droite arythmogène. In *Archives des maladies du coeur et des vaisseaux* 71 (9), pp. 963–972.
- **Frieden**, B. R.; Gatenby, R. A. (2019): Signal transmission through elements of the cytoskeleton form an optimized information network in eukaryotic cells. In *Scientific Reports* 9 (1), p. 6110. DOI: 10.1038/s41598-019-42343-2.
- **Gardel**, Margaret L.; Kasza, Karen E.; Brangwynne, Clifford P.; Liu, Jiayu; Weitz, David A. (2008): Chapter 19 Mechanical Response of Cytoskeletal Networks. In John J. Correia, H. William Detrich (Eds.): *Biophysical tools for biologists*, vol. 89. London: Academic (Methods in cell biology, 0091-679X, 84, 89), pp. 487–519.
- **Gavara**, Núria (2017): A beginner's guide to atomic force microscopy probing for cell mechanics. In *Microscopy Research and Technique* 80 (1), pp. 75–84. DOI: 10.1002/jemt.22776.
- **Gendelman**, Howard E.; Balogh, Lajos P.; Bawa, Raj; Bradbury, Michelle; Chang, Esther H.; Chiu, Wah et al. (2014): The 4th Annual Meeting of the American Society for Nanomedicine. In *Journal of Neuroimmune Pharmacology* 9 Suppl 1 (Suppl 1), S1-3. DOI: 10.1007/s11481-014-9526-4.

- **Gibson**, Christopher T.; Weeks, Brandon L.; Abell, Chris; Rayment, Trevor; Myhra, Sverre (2003): Calibration of AFM cantilever spring constants. In *Ultramicroscopy* 97 (1-4), pp. 113–118. DOI: 10.1016/S0304-3991(03)00035-4.
- **Gibson**, Christopher T.; Weeks, Brandon L.; Lee, Jonathan R. I.; Abell, Chris; Rayment, Trevor (2001): A nondestructive technique for determining the spring constant of atomic force microscope cantilevers. In *Review of Scientific Instruments* 72 (5), pp. 2340–2343. DOI: 10.1063/1.1361080.
- **Guck**, Jochen; Schinkinger, Stefan; Lincoln, Bryan; Wottawah, Falk; Ebert, Susanne; Romeyke, Maren et al. (2005): Optical deformability as an inherent cell marker for testing malignant transformation and metastatic competence. In *Biophysical Journal* 88 (5), pp. 3689–3698. DOI: 10.1529/biophysj.104.045476.
- **Guo**, Ming; Ehrlicher, Allen J.; Mahammad, Saleemulla; Fabich, Hilary; Jensen, Mikkel H.; Moore, Jeffrey R. et al. (2013): The role of vimentin intermediate filaments in cortical and cytoplasmic mechanics. In *Biophysical Journal* 105 (7), pp. 1562–1568. DOI: 10.1016/j.bpj.2013.08.037.
- **Guz**, Nataliia; Dokukin, Maxim; Kalaparthi, Vivekanand; Sokolov, Igor (2014): If cell mechanics can be described by elastic modulus: study of different models and probes used in indentation experiments. In *Biophysical Journal* 107 (3), pp. 564–575. DOI: 10.1016/j.bpj.2014.06.033.
- **Herren**, Thomas; Gerber, Philipp A.; Duru, Firat (2009): Arrhythmogenic right ventricular cardiomyopathy/dysplasia: a not so rare "disease of the desmosome" with multiple clinical presentations. In *Clinical research in cardiology : official journal of the German Cardiac Society* 98 (3), pp. 141–158. DOI: 10.1007/s00392-009-0751-4.
- **Hetz**, Claudio; Papa, Feroz R. (2018): The Unfolded Protein Response and Cell Fate Control. In *Molecular cell* 69 (2), pp. 169–181. DOI: 10.1016/j.molcel.2017.06.017.
- **Ho**, Huddee; West, Paul (1996): Optimizing AC-mode atomic force microscope imaging. In *Scanning* 18 (5), pp. 339–343. DOI: 10.1002/sca.1996.4950180503.
- **Hohmann**, Tim; Dehghani, Faramarz (2019): The Cytoskeleton-A Complex Interacting Meshwork. In *Cells* 8 (4). DOI: 10.3390/cells8040362.

- **Holliday**, Deborah L.; Speirs, Valerie (2011): Choosing the right cell line for breast cancer research. In *Breast cancer research : BCR* 13 (4), p. 215. DOI: 10.1186/bcr2889.
- **Hu**, Hai; Tian, Mingxing; Ding, Chan; Yu, Shengqing (2018): The C/EBP Homologous Protein (CHOP) Transcription Factor Functions in Endoplasmic Reticulum Stress-Induced Apoptosis and Microbial Infection. In *Frontiers in Immunology* 9, p. 3083. DOI: 10.3389/fimmu.2018.03083.
- **Hutter**, Jeffrey L.; Bechhoefer, John (1993): Calibration of atomic-force microscope tips. In *Review of Scientific Instruments* 64 (7), pp. 1868–1873. DOI: 10.1063/1.1143970.
- **Isermann**, Philipp; Lammerding, Jan (2013): Nuclear mechanics and mechanotransduction in health and disease. In *Current biology : CB* 23 (24), R1113-21. DOI: 10.1016/j.cub.2013.11.009.
- **Iurlaro**, Raffaella; Muñoz-Pinedo, Cristina (2016): Cell death induced by endoplasmic reticulum stress. In *The FEBS journal* 283 (14), pp. 2640–2652. DOI: 10.1111/febs.13598.
- **Jaalouk**, Diana E.; Lammerding, Jan (2009): Mechanotransduction gone awry. In *Nature reviews. Molecular cell biology* 10 (1), pp. 63–73. DOI: 10.1038/nrm2597.
- **Janin**, Alexandre; Bauer, Delphine; Ratti, Francesca; Millat, Gilles; Méjat, Alexandre (2017): Nuclear envelopathies: a complex LINC between nuclear envelope and pathology. In *Orphanet Journal of Rare Diseases* 12 (1), p. 147. DOI: 10.1186/s13023-017-0698-x.
- **Jazvinščak Jembrek**, Maja; Šimić, Goran; Hof, Patrick R.; Šegota, Suzana (2015): Atomic force microscopy as an advanced tool in neuroscience. In *Translational Neuroscience* 6 (1), p. 908. DOI: 10.1515/tnsci-2015-0011.
- **Jeon**, Oju; Alt, Daniel S.; Linderman, Stephen W.; Alsberg, Eben (2013): Biochemical and physical signal gradients in hydrogels to control stem cell behavior. In *Advanced materials (Deerfield Beach, Fla.)* 25 (44), pp. 6366–6372. DOI: 10.1002/adma.201302364.

- **Jiang, C.;** Zhu, Y.; Zhou, Z.; Gumin, J.; Bengtsson, L.; Wu, W. et al. (2017): TMEM43/LUMA is a key signaling component mediating EGFR-induced NF- κ B activation and tumor progression. In *Oncogene* 36 (20), pp. 2813–2823. DOI: 10.1038/onc.2016.430.
- **Johnston, Elizabeth F.;** Gillis, Todd E. (2017): Transforming growth factor beta-1 (TGF- β 1) stimulates collagen synthesis in cultured rainbow trout cardiac fibroblasts. In *The Journal of experimental biology* 220 (Pt 14), pp. 2645–2653. DOI: 10.1242/jeb.160093.
- **Jorgens, Danielle M.;** Inman, Jamie L.; Wojcik, Michal; Robertson, Claire; Palsdottir, Hildur; Tsai, Wen-Ting et al. (2017): Deep nuclear invaginations are linked to cytoskeletal filaments - integrated bioimaging of epithelial cells in 3D culture. In *Journal of Cell Science* 130 (1), pp. 177–189. DOI: 10.1242/jcs.190967.
- **Kámán, Judit** (2015): Young's Modulus and Energy Dissipation Determination Methods by AFM, with Particular Reference to a Chalcogenide Thin Film. In *Period. Polytech. Elec. Eng. Comp. Sci.* 59 (1), pp. 18–25. DOI: 10.3311/PPee.7865.
- **Kolahi, Kevin S.;** Mofrad, Mohammad R. K. (2010): Mechanotransduction: a major regulator of homeostasis and development. In *Wiley interdisciplinary reviews. Systems biology and medicine* 2 (6), pp. 625–639. DOI: 10.1002/wsbm.79.
- **Kontomaris, Stylianos-Vasileios** (2018): The Hertz Model in AFM Nanoindentation Experiments: Applications in Biological Samples and Biomaterials. In *MNS* 10 (1), pp. 11–22. DOI: 10.2174/1876402910666180426114700.
- **Krajarng, Aungkana;** Imoto, Masaya; Tashiro, Etsu; Fujimaki, Takahiro; Shinjo, Satoko; Watanapokasin, Ramida (2015): Apoptosis induction associated with the ER stress response through up-regulation of JNK in HeLa cells by gambogic acid. In *BMC Complementary and Alternative Medicine* 15, p. 26. DOI: 10.1186/s12906-015-0544-4.

- **Kumar**, Sanjay; Weaver, Valerie M. (2009): Mechanics, malignancy, and metastasis: the force journey of a tumor cell. In *Cancer metastasis reviews* 28 (1-2), pp. 113–127. DOI: 10.1007/s10555-008-9173-4.
- **Kustermans**, Gaelle; El Benna, Jamel; Piette, Jacques; Legrand-Poels, Sylvie (2005): Perturbation of actin dynamics induces NF-kappaB activation in myelomonocytic cells through an NADPH oxidase-dependent pathway. In *Biochemical Journal* 387 (Pt 2), pp. 531–540. DOI: 10.1042/BJ20041318.
- **Lee**, John M.; Jung, Hea-Jin; Fong, Loren G.; Young, Stephen G. (2014): Do lamin B1 and lamin B2 have redundant functions? In *Nucleus* 5 (4), pp. 287–292. DOI: 10.4161/nucl.29615.
- **Lee**, Stacey; Kumar, Sanjay (2016): Actomyosin stress fiber mechanosensing in 2D and 3D. In *F1000Research* 5. DOI: 10.12688/f1000research.8800.1.
- **Liang**, Wen-Chen; Mitsuhashi, Hiroaki; Keduka, Etsuko; Nonaka, Ikuya; Noguchi, Satoru; Nishino, Ichizo; Hayashi, Yukiko K. (2011): TMEM43 mutations in Emery-Dreifuss muscular dystrophy-related myopathy. In *Annals of neurology* 69 (6), pp. 1005–1013. DOI: 10.1002/ana.22338.
- **Lin**, David C.; Dimitriadis, Emilios K.; Horkay, Ferenc (2007): Robust strategies for automated AFM force curve analysis--I. Non-adhesive indentation of soft, inhomogeneous materials. In *Journal of biomechanical engineering* 129 (3), pp. 430–440. DOI: 10.1115/1.2720924.
- **Lingwood**, Daniel; Simons, Kai (2010): Lipid rafts as a membrane-organizing principle. In *Science (New York, N.Y.)* 327 (5961), pp. 46–50. DOI: 10.1126/science.1174621.
- **Liu**, Zhikui; Li, Chao; Kang, Ningling; Malhi, Harmeet; Shah, Vijay H.; Maiers, Jessica L. (2019): Transforming growth factor β (TGF β) cross-talk with the unfolded protein response is critical for hepatic stellate cell activation. In *The Journal of biological chemistry* 294 (9), pp. 3137–3151. DOI: 10.1074/jbc.RA118.005761.
- **Manificier**, Ian; Milan, Jean-Louis; Jeanneau, Charlotte; Chmilewsky, Fanny; Chabrand, Patrick; About, Imad (2016): Computational Tension Mapping of

- Adherent Cells Based on Actin Imaging. In *PloS one* 11 (1), e0146863. DOI: 10.1371/journal.pone.0146863.
- **Maninová**, Miloslava; Vomastek, Tomáš (2016): Dorsal stress fibers, transverse actin arcs, and perinuclear actin fibers form an interconnected network that induces nuclear movement in polarizing fibroblasts. In *The FEBS journal* 283 (20), pp. 3676–3693. DOI: 10.1111/febs.13836.
 - **Marcus**, Frank I.; Abidov, Aiden (2012): Arrhythmogenic right ventricular cardiomyopathy 2012: diagnostic challenges and treatment. In *Journal of cardiovascular electrophysiology* 23 (10), pp. 1149–1153. DOI: 10.1111/j.1540-8167.2012.02412.x.
 - **Marrese**, Marica; Guarino, Vincenzo; Ambrosio, Luigi (2017): Atomic Force Microscopy: A Powerful Tool to Address Scaffold Design in Tissue Engineering. In *Journal of Functional Biomaterials* 8 (1). DOI: 10.3390/jfb8010007.
 - **Martin**, Y.; Williams, C. C.; Wickramasinghe, H. K. (1987): Atomic force microscope–force mapping and profiling on a sub 100-Å scale. In *Journal of Applied Physics* 61 (10), pp. 4723–4729. DOI: 10.1063/1.338807.
 - **Matsumoto**, Hiroki; Miyazaki, Shuichi; Matsuyama, Satoshi; Takeda, Masayuki; Kawano, Makoto; Nakagawa, Hiroshi et al. (2013): Selection of autophagy or apoptosis in cells exposed to ER-stress depends on ATF4 expression pattern with or without CHOP expression. In *Biology Open* 2 (10), pp. 1084–1090. DOI: 10.1242/bio.20135033.
 - **McCauley**, Mark D.; Wehrens, Xander H. T. (2009): Animal models of arrhythmogenic cardiomyopathy. In *Disease Models & Mechanisms* 2 (11-12), pp. 563–570. DOI: 10.1242/dmm.002840.
 - **Merner**, Nancy D.; Hodgkinson, Kathy A.; Haywood, Annika F. M.; Connors, Sean; French, Vanessa M.; Drenckhahn, Jörg-Detlef et al. (2008): Arrhythmogenic right ventricular cardiomyopathy type 5 is a fully penetrant, lethal arrhythmic disorder caused by a missense mutation in the TMEM43 gene. In *American journal of human genetics* 82 (4), pp. 809–821. DOI: 10.1016/j.ajhg.2008.01.010.

- **Miller**, Ethan J.; Trewby, William; Farokh Payam, Amir; Piantanida, Luca; Cafolla, Clodomiro; Voitchovsky, Kislon (2016): Sub-nanometer Resolution Imaging with Amplitude-modulation Atomic Force Microscopy in Liquid. In *Journal of visualized experiments : JoVE* (118). DOI: 10.3791/54924.
- **Milting**, Hendrik; Klauke, Bärbel; Christensen, Alex Hoerby; Müsebeck, Jörg; Walhorn, Volker; Grannemann, Sören et al. (2015): The TMEM43 Newfoundland mutation p.S358L causing ARVC-5 was imported from Europe and increases the stiffness of the cell nucleus. In *European heart journal* 36 (14), pp. 872–881. DOI: 10.1093/eurheartj/ehu077.
- **Muhammed**, Ismaeel; Chowdhury, Farhan; Maruthamuthu, Venkat (2017): Biophysical Tools to Study Cellular Mechanotransduction. In *Bioengineering* 4 (1). DOI: 10.3390/bioengineering4010012.
- **Müller**, Daniel J.; Helenius, Jonne; Alsteens, David; Dufrêne, Yves F. (2009): Force probing surfaces of living cells to molecular resolution. In *Nature chemical biology* 5 (6), pp. 383–390. DOI: 10.1038/nchembio.181.
- **Ogata**, Maiko; Hino, Shin-ichiro; Saito, Atsushi; Morikawa, Keisuke; Kondo, Shinichi; Kanemoto, Soshi et al. (2006): Autophagy is activated for cell survival after endoplasmic reticulum stress. In *Molecular and cellular biology* 26 (24), pp. 9220–9231. DOI: 10.1128/MCB.01453-06.
- **Okumura**, Naoki; Hashimoto, Keisuke; Kitahara, Miu; Okuda, Hirokazu; Ueda, Emi; Watanabe, Kyoko et al. (2017): Activation of TGF- β signaling induces cell death via the unfolded protein response in Fuchs endothelial corneal dystrophy. In *Scientific Reports* 7 (1), p. 6801. DOI: 10.1038/s41598-017-06924-3.
- **Osowski**, Christine M.; Urano, Fumihiko (2011): Measuring ER stress and the unfolded protein response using mammalian tissue culture system. In *Methods in enzymology* 490, pp. 71–92. DOI: 10.1016/B978-0-12-385114-7.00004-0.
- **Osmanagic-Myers**, Selma; Dechat, Thomas; Foisner, Roland (2015): Lamins at the crossroads of mechanosignaling. In *Genes & Development* 29 (3), pp. 225–237. DOI: 10.1101/gad.255968.114.
- **Padrón-Barthe**, Laura; Villalba-Orero, María; Gómez-Salineró, Jesús M.; Domínguez, Fernando; Román, Marta; Larrasa-Alonso, Javier et al. (2019):

- Severe Cardiac Dysfunction and Death Caused by Arrhythmogenic Right Ventricular Cardiomyopathy Type 5 Are Improved by Inhibition of Glycogen Synthase Kinase-3 β . In *Circulation* 140 (14), pp. 1188–1204. DOI: 10.1161/CIRCULATIONAHA.119.040366.
- **Pegoraro**, Adrian F.; Janmey, Paul; Weitz, David A. (2017): Mechanical Properties of the Cytoskeleton and Cells. In *Cold Spring Harbor perspectives in biology* 9 (11). DOI: 10.1101/cshperspect.a022038.
 - **Pelling**, Andrew E.; Veraitch, Farlan S.; Chu, Carol Pui-Kei; Mason, Chris; Horton, Michael A. (2009): Mechanical dynamics of single cells during early apoptosis. In *Cell motility and the cytoskeleton* 66 (7), pp. 409–422. DOI: 10.1002/cm.20391.
 - **Pertici**, Irene; Bongini, Lorenzo; Melli, Luca; Bianchi, Giulio; Salvi, Luca; Falorsi, Giulia et al. (2018): A myosin II nanomachine mimicking the striated muscle. In *Nature communications* 9 (1), p. 3532. DOI: 10.1038/s41467-018-06073-9.
 - **Pilichou**, Kalliopi; Thiene, Gaetano; Bauce, Barbara; Rigato, Ilaria; Lazzarini, Elisabetta; Migliore, Federico et al. (2016): Arrhythmogenic cardiomyopathy. In *Orphanet Journal of Rare Diseases* 11, p. 33. DOI: 10.1186/s13023-016-0407-1.
 - **Piner**; Zhu; Xu; Hong; Mirkin (1999): "Dip-Pen" nanolithography. In *Science (New York, N.Y.)* 283 (5402), pp. 661–663. DOI: 10.1126/science.283.5402.661.
 - **Pobre**, Kristine Faye R.; Poet, Greg J.; Hendershot, Linda M. (2019): The endoplasmic reticulum (ER) chaperone BiP is a master regulator of ER functions: Getting by with a little help from ERdj friends. In *The Journal of biological chemistry* 294 (6), pp. 2098–2108. DOI: 10.1074/jbc.REV118.002804.
 - **Proksch**, R.; Schäffer, T. E.; Cleveland, J. P.; Callahan, R. C.; Viani, M. B. (2004): Finite optical spot size and position corrections in thermal spring constant calibration. In *Nanotechnology* 15 (9), pp. 1344–1350. DOI: 10.1088/0957-4484/15/9/039.

- **Proksch**, Roger (2006): Multifrequency, repulsive-mode amplitude-modulated atomic force microscopy. In *Appl. Phys. Lett.* 89 (11), p. 113121. DOI: 10.1063/1.2345593.
- **Putman**, Constant A. J.; van der Werf, Kees O.; Grooth, Bart G. de; van Hulst, Niek F.; Greve, Jan (1994): Tapping mode atomic force microscopy in liquid. In *Appl. Phys. Lett.* 64 (18), pp. 2454–2456. DOI: 10.1063/1.111597.
- **Rajkumar**, Revathi; Sembrat, John C.; McDonough, Barbara; Seidman, Christine E.; Ahmad, Ferhaan (2012): Functional effects of the TMEM43 Ser358Leu mutation in the pathogenesis of arrhythmogenic right ventricular cardiomyopathy. In *BMC Medical Genetics* 13, p. 21. DOI: 10.1186/1471-2350-13-21.
- **Rosenbluth**, Michael J.; Lam, Wilbur A.; Fletcher, Daniel A. (2006): Force microscopy of nonadherent cells: a comparison of leukemia cell deformability. In *Biophysical Journal* 90 (8), pp. 2994–3003. DOI: 10.1529/biophysj.105.067496.
- **Rozpedek**, W.; Pytel, D.; Mucha, B.; Leszczynska, H.; Diehl, J. A.; Majsterek, I. (2016): The Role of the PERK/eIF2 α /ATF4/CHOP Signaling Pathway in Tumor Progression During Endoplasmic Reticulum Stress. In *Current molecular medicine* 16 (6), pp. 533–544. DOI: 10.2174/1566524016666160523143937.
- **Ruggeri**, Francesco Simone; Šneideris, Tomas; Vendruscolo, Michele; Knowles, Tuomas P. J. (2019): Atomic force microscopy for single molecule characterisation of protein aggregation. In *Archives of biochemistry and biophysics* 664, pp. 134–148. DOI: 10.1016/j.abb.2019.02.001.
- **Samali**, Afshin; Fulda, Simone; Gorman, Adrienne M.; Hori, Osamu; Srinivasula, Srinivasa M. (2010): Cell stress and cell death. In *International Journal of Cell Biology* 2010, p. 245803. DOI: 10.1155/2010/245803.
- **Schäffer**, Tilman E. (2005): Calculation of thermal noise in an atomic force microscope with a finite optical spot size. In *Nanotechnology* 16 (6), pp. 664–670. DOI: 10.1088/0957-4484/16/6/007.

- **Scheper**, Wiep; Hoozemans, Jeroen J. M. (2015): The unfolded protein response in neurodegenerative diseases: a neuropathological perspective. In *Acta Neuropathologica* 130 (3), pp. 315–331. DOI: 10.1007/s00401-015-1462-8.
- **Scholl**, Zackary N.; Marszalek, Piotr E. (2018): AFM-Based Single-Molecule Force Spectroscopy of Proteins. In *Methods in molecular biology (Clifton, N.J.)* 1814, pp. 35–47. DOI: 10.1007/978-1-4939-8591-3_3.
- **Schwarz**, Dianne S.; Blower, Michael D. (2016): The endoplasmic reticulum: structure, function and response to cellular signaling. In *Cellular and Molecular Life Sciences* 73 (1), pp. 79–94. DOI: 10.1007/s00018-015-2052-6.
- **Sciatti**, Edoardo; Vizzardì, Enrico; Bonadei, Ivano; Fabbricatore, Davide; Prati, Francesco; Pagnoni, Mattia; Metra, Marco (2018): Prognostic evaluation of the elastic properties of the ascending aorta in dilated cardiomyopathy. In *European journal of clinical investigation* 48 (7), e12950. DOI: 10.1111/eci.12950.
- **Sehgal**, Pankaj; Szalai, Paula; Olesen, Claus; Praetorius, Helle A.; Nissen, Poul; Christensen, Søren Brøgger et al. (2017): Inhibition of the sarco/endoplasmic reticulum (ER) Ca²⁺-ATPase by thapsigargin analogs induces cell death via ER Ca²⁺ depletion and the unfolded protein response. In *The Journal of biological chemistry* 292 (48), pp. 19656–19673. DOI: 10.1074/jbc.M117.796920.
- **Shacham**, Talya; Sharma, Neeraj; Lederkremer, Gerardo Z. (2019): Protein Misfolding and ER Stress in Huntington's Disease. In *Frontiers in molecular biosciences* 6, p. 20. DOI: 10.3389/fmolb.2019.00020.
- **Shi**, Xiang; Wang, Jingjing; Lei, Yu; Cong, Caofan; Tan, Dailin; Zhou, Xianrong (2019): Research progress on the PI3K/AKT signaling pathway in gynecological cancer (Review). In *Molecular Medicine Reports* 19 (6), pp. 4529–4535. DOI: 10.3892/mmr.2019.10121.
- **Siragam**, Vinayakumar; Cui, Xuezhi; Masse, Stephane; Ackerley, Cameron; Aafaqi, Shabana; Strandberg, Linn et al. (2014): TMEM43 mutation p.S358L alters intercalated disc protein expression and reduces conduction velocity in arrhythmogenic right ventricular cardiomyopathy. In *PloS one* 9 (10), e109128. DOI: 10.1371/journal.pone.0109128.

- **Srinivasan**, Neil T.; Schilling, Richard J. (2018): Sudden Cardiac Death and Arrhythmias. In *Arrhythmia & Electrophysiology Review* 7 (2), p. 111. DOI: 10.15420/aer.2018:15:2.
- **Starr**, Daniel A. (2007): Communication between the cytoskeleton and the nuclear envelope to position the nucleus. In *Molecular bioSystems* 3 (9), pp. 583–589. DOI: 10.1039/b703878j.
- **Stroud**, Matthew J. (2018): Linker of nucleoskeleton and cytoskeleton complex proteins in cardiomyopathy. In *Biophysical Reviews* 10 (4), pp. 1033–1051. DOI: 10.1007/s12551-018-0431-6.
- **Stroud**, Matthew J.; Banerjee, Indroneal; Veevers, Jennifer; Chen, Ju (2014): Linker of nucleoskeleton and cytoskeleton complex proteins in cardiac structure, function, and disease. In *Circulation research* 114 (3), pp. 538–548. DOI: 10.1161/CIRCRESAHA.114.301236.
- **Stylianou**, Andreas; Kontomaris, Stylianos-Vasileios; Grant, Colin; Alexandratou, Eleni (2019): Atomic Force Microscopy on Biological Materials Related to Pathological Conditions. In *Scanning* 2019, p. 8452851. DOI: 10.1155/2019/8452851.
- **Svitkina**, Tatyana M. (2018): Ultrastructure of the actin cytoskeleton. In *Current opinion in cell biology* 54, pp. 1–8. DOI: 10.1016/j.ceb.2018.02.007.
- **Swift**, Joe; Ivanovska, Irena L.; Buxboim, Amnon; Harada, Takamasa; Dingal, P. C. Dave P.; Pinter, Joel et al. (2013): Nuclear lamin-A scales with tissue stiffness and enhances matrix-directed differentiation. In *Science (New York, N.Y.)* 341 (6149), p. 1240104. DOI: 10.1126/science.1240104.
- **Taatjes**, Douglas J.; Quinn, Anthony S.; Rand, Jacob H.; Jena, Bhanu P. (2013): Atomic force microscopy: High resolution dynamic imaging of cellular and molecular structure in health and disease. In *Journal of cellular physiology* 228 (10), pp. 1949–1955. DOI: 10.1002/jcp.24363.
- **Tanja Mierke**, Claudia (2017): Physical role of nuclear and cytoskeletal confinements in cell migration mode selection and switching. In *AIMS Biophysics* 4 (4), pp. 615–658. DOI: 10.3934/biophy.2017.4.615.

- **Taylor**, Rebecca C.; Cullen, Sean P.; Martin, Seamus J. (2008): Apoptosis: controlled demolition at the cellular level. In *Nature reviews. Molecular cell biology* 9 (3), pp. 231–241. DOI: 10.1038/nrm2312.
- **Thomas**, Gawain; Burnham, Nancy A.; Camesano, Terri Anne; Wen, Qi (2013): Measuring the mechanical properties of living cells using atomic force microscopy. In *Journal of visualized experiments : JoVE* (76). DOI: 10.3791/50497.
- **Thorpe**, Stephen D.; Lee, David A. (2017): Dynamic regulation of nuclear architecture and mechanics-a rheostatic role for the nucleus in tailoring cellular mechanosensitivity. In *Nucleus (Austin, Tex.)* 8 (3), pp. 287–300. DOI: 10.1080/19491034.2017.1285988.
- **Timberlake**, Matthew, II; Dwivedi, Yogesh (2019): Linking unfolded protein response to inflammation and depression: potential pathologic and therapeutic implications. In *Molecular psychiatry* 24 (7), pp. 987–994. DOI: 10.1038/s41380-018-0241-z.
- **Uitto**, Jouni; Kouba, David (2000): Cytokine modulation of extracellular matrix gene expression: relevance to fibrotic skin diseases. In *Journal of Dermatological Science* 24, S60-S69. DOI: 10.1016/S0923-1811(00)00143-2.
- **Uzer**, Gunes; Rubin, Clinton T.; Rubin, Janet (2016): Cell Mechanosensitivity is Enabled by the LINC Nuclear Complex. In *Current molecular biology reports* 2 (1), pp. 36–47. DOI: 10.1007/s40610-016-0032-8.
- **Vahabi**, Surena; Nazemi Salman, Bahareh; Javanmard, Anahita (2013): Atomic force microscopy application in biological research: a review study. In *Iranian Journal of Medical Sciences* 38 (2), pp. 76–83.
- **Veerapandian**, Murugan; Yun, Kyusik (2009): Study of Atomic Force Microscopy in Pharmaceutical and Biopharmaceutical Interactions - A Mini Review. In *CPA* 5 (3), pp. 256–268. DOI: 10.2174/157341209788922020.
- **Vinckier**, Anja; Semenza, Giorgio (1998): Measuring elasticity of biological materials by atomic force microscopy. In *FEBS Letters* 430 (1-2), pp. 12–16. DOI: 10.1016/S0014-5793(98)00592-4.

- **Walter**, Franziska; O'Brien, Aisling; Concannon, Caoimhín G.; Düssmann, Heiko; Prehn, Jochen H. M. (2018): ER stress signaling has an activating transcription factor 6 α (ATF6)-dependent "off-switch". In *The Journal of biological chemistry* 293 (47), pp. 18270–18284. DOI: 10.1074/jbc.RA118.002121.
- **Wang**, Dau-Chung; Chen, Ken-Yen; Tsai, Cheng-Hsien; Chen, Gen-You; Chen, Chuan-Hung (2011): AFM membrane roughness as a probe to identify oxidative stress-induced cellular apoptosis. In *Journal of biomechanics* 44 (16), pp. 2790–2794. DOI: 10.1016/j.jbiomech.2011.08.021.
- **Wang**, Xian; Liu, Haijiao; Zhu, Min; Cao, Changhong; Xu, Zhensong; Tsatskis, Yonit et al. (2018): Mechanical stability of the cell nucleus - roles played by the cytoskeleton in nuclear deformation and strain recovery. In *Journal of Cell Science* 131 (13). DOI: 10.1242/jcs.209627.
- **West**, Gun; Gullmets, Josef; Virtanen, Laura; Li, Song-Ping; Keinänen, Anni; Shimi, Takeshi et al. (2016): Deleterious assembly of the lamin A/C mutant p.S143P causes ER stress in familial dilated cardiomyopathy. In *Journal of Cell Science* 129 (14), pp. 2732–2743. DOI: 10.1242/jcs.184150.
- **Yalcin**, Abdullah; Hotamisligil, Gökhan S. (2013): Impact of ER protein homeostasis on metabolism. In *Diabetes* 62 (3), pp. 691–693. DOI: 10.2337/db12-1526.
- **Yoshida**, Tatsushi; Sakai, Toshiyuki (2011): Tunicamycin. In M. Schwab (Ed.): *Encyclopedia of cancer*. 3rd ed. Heidelberg, New York: Springer (Springer reference), pp. 3816–3819.
- **Zemel**, Assaf (2015): Active mechanical coupling between the nucleus, cytoskeleton and the extracellular matrix, and the implications for perinuclear actomyosin organization. In *Soft matter* 11 (12), pp. 2353–2363. DOI: 10.1039/c4sm02425g.
- **Zheng**, Guoxing; Jiang, Changying; Li, Yulin; Yang, Dandan; Ma, Youcai; Zhang, Bing et al. (2019): TMEM43-S358L mutation enhances NF- κ B-TGF β signal cascade in arrhythmogenic right ventricular dysplasia/cardiomyopathy. In *Protein & Cell* 10 (2), pp. 104–119. DOI: 10.1007/s13238-018-0563-2.

- **Zitzler**, L.; Herminghaus, S.; Mugele, F. (2002): Capillary forces in tapping mode atomic force microscopy. In *Phys. Rev. B* 66 (15). DOI: 10.1103/PhysRevB.66.155436.
- **Zwenger**, Monika; Ho, Chin Yee; Lammerding, Jan (2011): Nuclear mechanics in disease. In *Annual review of biomedical engineering* 13, pp. 397–428. DOI: 10.1146/annurev-bioeng-071910-124736.

Summary

The xanthan gum is an exopolysaccharide which is secreted by the gram-negative phytopathogen the *Xanthomonas campestris* (Xcc). Given its distinctive rheological properties such as the capability to form a highly viscous solution at low shear forces, xanthan was used in various applications such as the foods industry, cosmetics, pharmaceuticals and technical applications. With the growing industrial importance, many biotechnological approaches used to improve the xanthan gum production. Targeted metabolic engineering of *Xanthomonas campestris* (Xcc) could be an effective approach in which xanthan production efficiency and optimize shear-thickening potency is improved. By means of atomic force microscopy (AFM), the secondary structure of the single molecules of the wild type xanthan strain B100, the mutant xanthan strain Xcc H21012 (wxcB), the commercial acetate, pyruvate-free xanthan, and JBL007 were analyzed. The topological images of the single molecules of xanthan revealed characteristic differences between these strains. The structures ranged from branched xanthan double-strands of both the B100 and the strain Xcc H21012 (wxcB), while other products showed a single-stranded coiled polymer. Here, these results proved that the secondary structure of xanthan strongly correlates with its viscosity properties. Overall, the results of this study provide a better understanding of the polymerization and secretion-machinery related to the biosynthesis of xanthan gum which will benefit future applications.

2.1 Introduction

Polysaccharides are biopolymers that play an essential role in molecular recognition. They are located in many plants like; seaweeds or bacterial fermentation (Ross-Murphy et al. 1998; Sutherland 2001-2003; Miao et al. 2018). It has a high affinity to water, and it is able to increase the viscosity of the solution, even at low concentrations. It is commonly called gums. Xanthan gum is one of the most important and widely used polysaccharides (Guo et al. 2017; Fagioli et al. 2019).

2.1.1 Xanthan gum

2.1.1.1 History

In the middle of the last century, Xanthan was discovered at the National Center of the United States Department of Agriculture (USDA) for agricultural uses. In 1960, the first industrial production of xanthan was carried out, followed by the commercial products in 1964 (Margaritis and Zajic 1978). It is the second microbial polysaccharide that is industrially commercialized, after dextran. Xanthan gum is characterized as a non-toxic, non-sensitizing agent also, it does not irritate both of skin or eyes and was adopted in 1969 by the United States Food and Drug Administration (FDA) (Meddeb et al. 2015).

2.1.1.2 Production of Xanthan Gum

A. *Xanthomonas (campestris)*

Xanthomonas is a gram-negative plant-associated bacterium that belongs to the family *Pseudomonadaceae* (Ryan et al. 2011; Rodriguez-R et al. 2012). This genus comprises of many different strains that produce xanthan gum, such as *X. arboricola*, *X. axonopodis*, *X. campestris*, *X. citri*, *X. fragaria*, *X. gummisudans*, *X. juglandis*, *X. phaseoli*, *X. vasculorum*. All of those strains are plant pathogens (Katzen et al. 1998). The *Xanthomonas campestris* is most widely used in the commercial production of xanthan gum. This strain is short, rod-shaped with a size of 0.7 to 1.0 x 2.0 to 2.4 μm and strictly aerobic; wherefore, oxygen is a fundamental part for its growth and xanthan gum production (Fig. 2-26) (García-Ochoa et al. 2000; Dai et al. 2019).

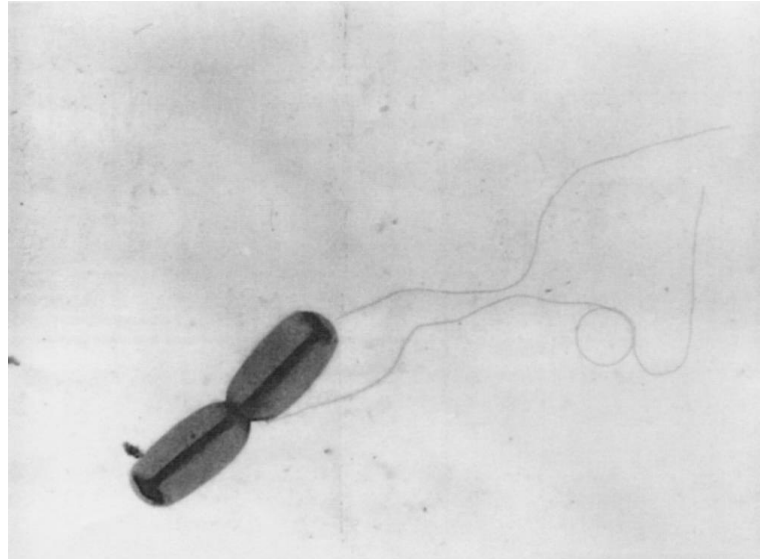


Figure 2-1: Transmission electron microscope image of *X.campestris*, which exist individually or in pairs, and they are motile attribute to a single flagellum (1.7–3.0 μm long) (García-Ochoa et al. 2000).

B. Biosynthesis of Xanthan Gum

The process of biosynthesis of xanthan by *X. campestris* is a complex process involving a multi-enzyme system (Fig.2-2) (Becker et al. 1998; Alkhateeb et al. 2018; Vorhölter et al. 2008). This process begins upon uptake of carbohydrate, which usually occurs either by active transport or facilitated diffusion. Then, the phosphorylation process of the substrate occurs by hexokinase enzymes, which use adenosine 5'-triphosphate. The presence of enzymes such as UDP-Glc pyrophosphorylase results in, conversion of the phosphorylated substrate to the different nucleotide derivatives, as well as producing the nucleotide precursor sugars (NDP-sugars) (Vorhölter et al. 2008). The nucleotide precursor sugars (NDP-sugars) such as UDP-glucose, GDP-mannose and UDP-glucuronic acids are necessary elements of the biosynthesis of xanthan gum with the proper repeating unit (Alkhateeb et al. 2018; Vorhölter et al. 2008). During the phase of assembling of the monosaccharide subunits, pentasaccharide repeating units are constructed from glucose, mannose, and glucuronic acid in a molar ratio of 2:2:1 (Schatschneider et al. 2013; Vorhölter et al. 2008). Here, the enzymes glycosyltransferases which are encoded by the Gum D, Gum M, Gum H, Gum K, and Gum I genes are responsible for complete synthesis of the monosaccharide subunits (Barreras et al. 2004; Vorhölter et al. 2008). The synthesis of these repeating units takes place through the sequential transfer of monosaccharides from NDP-sugars by

glycosyltransferases. These monosaccharides are bound to a polyisoprenol lipid carrier at the inner membrane of the cell. This lipid carrier consists of long-chain phosphate ester and isoprenoide alcohol, which has a role to in organizing the formation of the carbohydrate chain and also stimulate the chain transfer through the cell membrane using a phosphate anchor (Donot et al. 2012). The basis of the synthesis of monosaccharides repeating units depends on the transfer of glycosyl-1-phosphate by a UDP-glucose molecule to the polyisoprenol phosphate transporter. The completion of the lipid-linked pentasaccharide unit assembly depends on the consecutive transfer of d-mannose from GDP-mannose and d-glucuronic acid from UDP-glucuronic acid (Rosalam and England 2006). The pyruvyltransferase (Gum L) is used to add pyruvate to the terminal mannose residues, while the acetyltransferases (Gum F and Gum G) are used to add acetyl groups to inner the mannose residues in the repeating unit (Hager et al. 2019). In the next phase, the flippase enzymes flips the lipid carrier with the pentasaccharide repeating units from the cytoplasmic face of the inner membrane to the periplasmic face (Becker 2015; Islam and Lam 2013). During the polymerization process, the mature xanthan chain is transported to the extracellular medium. Nevertheless, the exact mechanism of the polymerization and exportation processes is still obscure (Vorhölter et al. 2008).

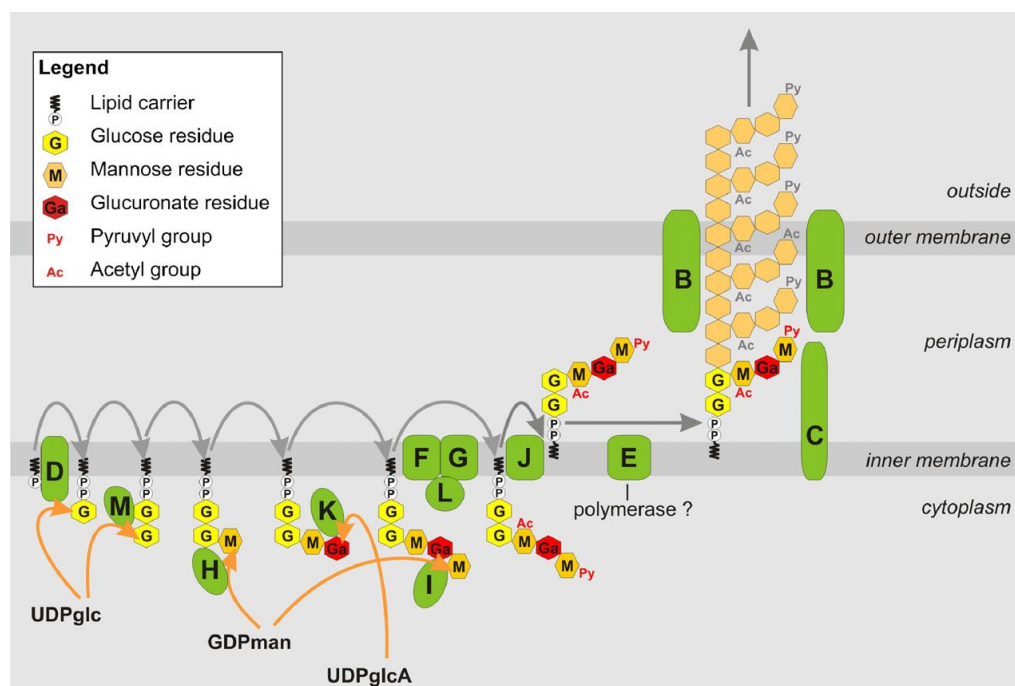


Figure 2-2: The biosynthesis process for xanthan gum at the inner membrane of *Xanthomonas campestris pv. campestris* (Xcc) (Vorhölter et al. 2008).

C. Commercial Production Process

It is well known that Xanthan is an anionic polysaccharide with prominent rheological properties and the fermentation of *Xanthomonas campestris pv. campestris* (Xcc) is a fundamental way that is used to produce Xanthan (Ross-Murphy et al. 1998; Palaniraj and Jayaraman 2011a). It comprises the biggest proportion of the total world microbial polysaccharide market with an anniversary production exceeding 150 000 tons. In large fermenters, more than 350 000 litres were used to produce a large scale in a feed batch process (Kreyenschulte et al. 2014; Dai et al. 2019). The production process of xanthan includes preparation of the bacterial inoculum and the substrate, fermentation, cell removal, recovery, and purification of the final product (García-Ochoa et al. 2000). In the fermentation process, the production of xanthan gum is stimulated using organic acids at a temperature between 27 °C and 30 °C (Habibi and Khosravi-Darani 2017). In order to obtain a high-quality product from the substrates used for xanthan gum production, the conditions for the fermentation process must be carefully evaluated. These assessments usually determine the starting point of bench-scale experiments which generates significant results for upscaling (Soleymanpour et al. 2018). These results may be useful to choose appropriate xanthan strains, the nutrients desired for fermentation, the conditions for microbial growth are vital and aeration and fermentation time. The xanthan gum is produced on a broad commercial scale by a batch fermentation process (Palaniraj and Jayaraman 2011b; Soleymanpour et al. 2018). After the fermentation step, bacterial cells, and many unwanted substances are removed from the fermented culture medium by filtration or centrifugation (Leroy and Vuyst 2016). Moreover, for high purity, organic solvents (isopropanol, ethanol) are used to enhance the precipitation of xanthan (García-Ochoa et al. 2000). At the end of the precipitation, the final product with desirable qualities is dewatered and dried. Then, the dried product is milled and packed into containers. These containers have low permeability of water (Palaniraj and Jayaraman 2011a). This process is illustrated in Fig. 2-3.



Figure2-3: The steps of producing xanthan gum (Synder filtration website)

2.1.2 Chemical structure of xanthan gum

Xanthan has remarkable biocompatibility and excellent water solubility as well as to owning having branched polymeric chains (Song et al. 2019; Mohammadinejad et al. 2020). In 1975, the primary structure of xanthan was established. It is composed of a sugar backbone which has two D-glucose residues and a side chain composed of D-mannose, and D-glucuronic acid that is connected in a ratio of 2:2:1 (Fig 2-4) (Jansson et al. 1975; Douglas et al. 2018). Accordingly, a subunit of xanthan depicts a pentasaccharide. The D-mannose unit can be linked to an acetyl group and a pyruvic acid substitute which put negative charge in the side chain of the polymer structure (Phillips and Williams 2009; Moffat et al. 2016). The secondary structure of xanthan relies on the charged side chains (Phillips and Williams 2009). These side chains are closely related with the cellulosic backbone of xanthan, resulting in the rigid helical structure, which contributes to the complex formation through interacts with other molecules (Moorhouse et al. 1977; Moffat et al. 2016). The unique characteristics of xanthan gum, including the rheological properties, thickening, and a great pseudo-plasticity, are due to its distinct chemical structure and a large molecular weight (Hu et al. 2019). Both structure and molecular weight of the polymer are affected by fermentation conditions used in the production of xanthan (García-Ochoa et al. 2000). The xanthan exists at low physiological temperatures in an ordered structure, but at higher temperatures, it becomes disordered. This is defined as “order-disorder transition” and affected by different factors including pH-value, pyruvate-, acetyl

content and salt concentration of the solution (Kool et al. 2013; Yang et al. 2019). In diffraction experiments using X-ray, xanthan exists as a right-handed helix, in which the side chains enclose the helix. Although, we could not get a definite proof if the helix is composed of a single xanthan polymer or two molecules as a double helix (Moorhouse et al. 1977). Recent studies have provided evidence of the presence of xanthan as a double-stranded helix in its ordered form (Moffat et al. 2016; Teckentrup et al. 2017). Furthermore, the xanthan molecule takes the form of a ‘random coil’ on positively charged mica. This form is characterized as less stiff and describe the disordered form that xanthan can build in solutions with a very low ionic strength (Gulrez et al. 2012).

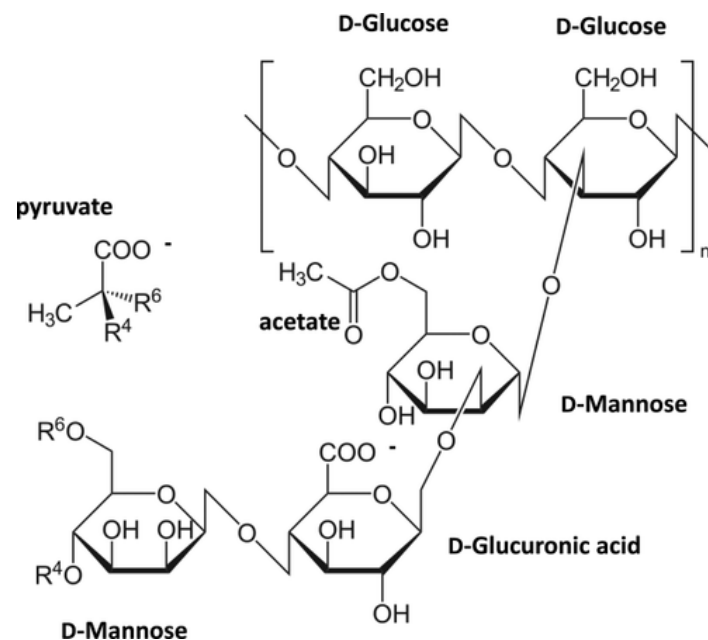


Figure 2-4: The primary structure of xanthan, D-mannose and D-glucuronic acid units are linked to the glucose backbone. Acetate and pyruvate can be linked in different amounts to the D-mannose subunits of the chain (Petri 2015).

2.1.3 Properties of Xanthan Solutions

Xanthan gum is characterized by its ability to be soluble in both cold and hot water due to the polyelectrolyte nature of xanthan molecule (Goff and Guo 2019). Xanthan solutions have sufficiently high viscosity even at low concentrations. Xanthan solutions display highly pseudo-plastic or shear-thinning behaviour under increasing shear rates (Luvielmo et al. 2016). Xanthan’s viscosity is mainly based on salt

concentration, temperature, pH-value and pyruvate-, acetyl content of the solution (Petri 2015). Both the measurement temperature and dissolution temperature affect the viscosity of xanthan solutions. Here, solutions of xanthan at low dissolution temperatures are highly viscous compared to high temperatures. So, xanthan exists at low dissolution temperatures in an ordered structure, but at higher temperatures, it becomes disordered. This characteristic behavior of the xanthan molecule is attributed to the conformational changes (order-disorder transition) (García-Ochoa et al. 2000; Petri 2015). In industrial and food application, xanthan is preferred over many water-soluble polysaccharides due to the thermal stability. This may be attributed to the ordered helical structure; which is protects the molecules from de-polymerization (Stokke and Christensen 1996). Xanthan concentration significantly influences the viscosity of the solution. At high polymer concentration, the viscosity rate is high due to the interaction between strands or the dense entanglement of the intermolecular. This leads to an increase in the dimensions of the effective macromolecules as well as higher of the molecular weight rates (García-Ochoa et al. 2000). Also, the salts concentration affects the viscosity; at low biopolymer concentration, the viscosity of xanthan decreases a bit upon the addition of a small amount of salt to the solution. This behavior is due to the reduction in shielding of electrostatic interaction between intermolecular, which in turn reduces intermolecular dimensions (Smith and Pace 1982). Notwithstanding, the high reaction rates between biopolymer molecules may give another reason for an increased viscosity at the high polymer concentration or when a large amount of salts (Smith and Pace 1982; Milas and Rinaudo 1986; García-Ochoa et al. 2000). On the other hand, Kang and Pettitt (2012) they proved that the salt content was higher than 0.1% (w/v), the viscosity of solution can be independent of the effect of the salt content. Moreover, the presence of salts may give a more ordered conformation, but their effectiveness depends on nature of the linked ions (especially cations, such as Ca^{2+} , K^+ , and Na^+) (Galván et al. 2018). For example, Ca^{2+} ions stimulate a complex formation involving two di-saccharide units of the main chain and pairs of carboxyl groups separate helices. This complex promotes interactions between intra-and intermolecular, and therefore, result in increased viscosity of the solution (Mohammed et al. 2007). On the other hand, the dynamic viscoelasticity xanthan solutions are stable in over a broad range of pH values (P. Bharali 2013). At high pH (up9), xanthan chains are subject to conformational changes from a more ordered state to coils in disorder state (Bueno and Petri 2014), while in low pH (less than 3), xanthan

gum behaves as a polyanion. This is due to a loss of the pyruvic acid acetyl groups (Petri 2015). The molecular composition of xanthan also affects the conformational state (Order–disorder transitions). Indeed, the conformational state of the helix is affected by the degrees of substitution of the acetyl and pyruvate groups (Shatwell et al. 1990). The distribution of acetyl and pyruvyl residues in the xanthan molecule depends on the *Xanthomonas* strains, medium composition, culture conditions, and intentional structural modifications (García-Ochoa et al. 2000; Li and Feke 2015). Approximately more than half of the inner mannose residues may be acetylated, while only 40% of the terminal mannose residues can be replaced by ketal-pyruvate groups (Conforte et al. 2019). The rheological properties of xanthan solution are affected by the content of these groups, especially the viscosity, and also its stability with respect to temperature and salts (Petri 2015; Dário et al. 2011).

2.1.4 Applications of Xanthan gum

The biopolymer xanthan is an occupied important ingredient in various applications such as the foods industry (Petri 2015), cosmetics (Fiume et al. 2016), water treatments (Petri 2015), and pharmaceuticals (Rosalam and England 2006). Even more, it also plays an important role in technical applications such as gas and oil-drilling projects, especially during drilling, fracturing, pipeline cleaning, workover, and completion (Kreyenschulte et al. 2014). This is mainly owing to its distinctive rheological properties, including the ability to form a highly viscous solution even at low concentrations and pseudo-elasticity. Moreover, xanthan shows great stability in a wide range of temperatures, salinities, and pH values (Ashraf et al. 2017). In all above applications, Xanthan is utilized as a thickener, emulsifier and stabilizer for emulsions suspensions (Rosalam and England 2006; Kreyenschulte et al. 2014). The food industries are the most important areas of applications of xanthan. It is utilized in a wide range of food products (e.g. sauces, baked goods and dairy products, etc.), in order to obtain desired properties of food products such as flavour, viscosity and appearance. The xanthan content in food lies in the range of 0.05–0.7 wt—% (Zhou and Hui 2014). After addition to food, xanthan may undergo major variations in pH and ionic strength. It is may also be affected by the ingredients of the formulation, such as salts, acids, and proteins (Freitas et al. 2011). These ingredients can affect the xanthan due to changes in matrix charge. For example, salt concentrations adversely influence viscosity. In order to avoid these effects, it is recommended to use moisturizing xanthan to have a good

ability to tolerate salt even at 30 % (Rinaudo and Moroni 2009). The use of xanthan was not only limited in the food industry; it even extended its applications to the personal care products such as toothpaste, creams and shampoos in order to obtain the right consistency, improve the flow, suspend insoluble ingredients, and promote a stable, rich, and creamy lather (Rosalam and England 2006). The xanthan was also applied in agriculture, especially agricultural chemical preparations (e.g. fungicides, herbicides, and insecticides etc.); in order to get products of high quality in terms of effectiveness, spread and adhesiveness to the plant surface (Flickinger and Draw, 1999). Currently, xanthan is also widely used in biomedical applications such as drug delivery and tissue engineering, because of its ability to form networks allowing its application as a drug carrier as well as biodegradability and biocompatibility in vivo (Rosalam and England 2006; Kreyenschulte et al. 2014). In these applications, it was used as a thickener, emulsifier, and also in topical formulas; as a controlled release agent in tablets; and as a binder in colon-specific drug delivery systems (Palaniraj and Jayaraman 2011a).

The main objective of this study

The major objectives of this study were focused on two parts. Firstly we tried to provide a direct comparison of various xanthan samples which have been produced by several different *X. campestris* strains in order to identify differences in their secondary structures. Secondly, we wanted to find a reasonable explanation linking microscopic structural features of xanthan with its macroscopic viscosity. By using atomic force microscopy (AFM), several single molecules of xanthan samples under ambient conditions were analyzed. In addition, the structural parameters such as the molecule height, contour and persistence length were estimated where possible. Overall, this study provided an integrated evaluation of the individual xanthan molecules to determine distinct secondary structures which can be attributed to the chemical composition of the xanthan side chains.

2.2 Materials and Methods

2.2.1 Xanthan samples

In this work, a group of different xanthan strains were used, as shown in table 2-1.

Table 2-1: Overview of xanthan samples

| No. | Xanthan samples | Characteristics |
|-----|--|---|
| 1 | Wild type Xcc B100 | Wild type strain xanthan; precipitated by isopropanol |
| 2 | Wild type Xcc B100 | Wild type strain xanthan; unprecipitated by isopropanol |
| 3 | Mutant Xcc H21012 (wxcB) | Mutant type strain xanthan; precipitated by isopropanol |
| 4 | Mutant Xcc H21012 (wxcB) | Mutant type strain xanthan; unprecipitated by isopropanol |
| 5 | Acetate-free xanthan | Acetyl group of xanthan missing |
| 6 | Production strain (JBL007; derivative of NRRL B-1459). | Selected for xanthan production |
| 7 | Pyruvate-free xanthan | Pyruvate of xanthan missing |

Xantomonas campestris pv. *campestris* (Xcc) cultures grown in the minimal medium have been used to extract xanthan samples (Schatschneider et al. 2014). Then, xanthan is precipitated as described by Steffens et al. (2016). All xanthan samples were kindly provided by Professor Karsten Niehaus from Proteome and Metabolome Research, Faculty of Biology, Bielefeld University.

2.2.2 Measurements Samples

All samples used were distributed in deionized water and by an initial concentration ranging from 1mg/ml^{-1} to 2mg/ml^{-1} . In order to obtain individual well-separated molecules, the serial dilution method was used. The effective concentrations of samples ranged between 2 and $5\ \mu\text{g ml}^{-1}$. For AFM imaging under ambient conditions, $5\ \mu\text{l}$ of the xanthan solution was dropped onto a freshly cleaved mica

substrate. After 30 seconds of incubation, the samples were dried under a gentle flow of dry nitrogen gas.

2.2.3 AFM experiments

2.2.3.1 AFM setup

A commercial AFM (Multimode 8, Bruker, USA) was used to obtain topographic images of single xanthan molecules. The AFM was mounted on an isolation table TS150 (Table Stable LTD, Switzerland) to provide for a disturbance-free environment and also an acoustic enclosure was used (Park Systems, Korea) during the measurements (Figure 4). The scanning and imaging process was conducted by the AFM controller software Nanoscope (versions 5.30 and 8.15) in tapping mode. Tap300 Al-G monolithic silicon cantilevers with an aluminum reflex coating were used (Budget Sensors, Sofia, Bulgaria).

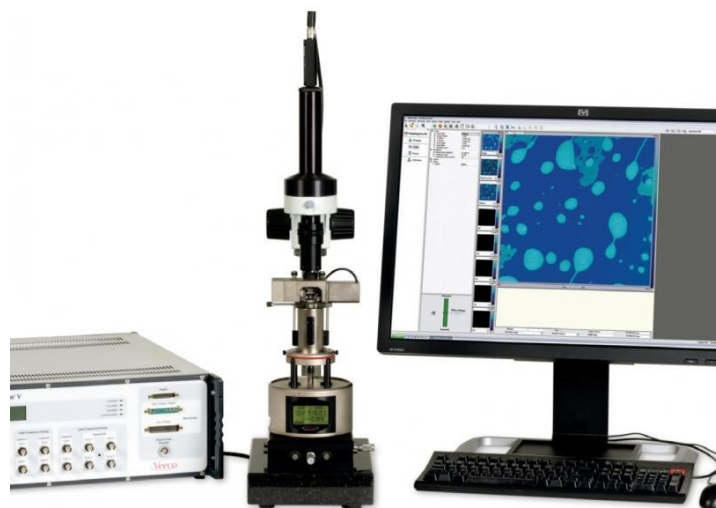


Figure2-5: Image illustrates the AFM-Multimode 8 setup

2.2.3.2 Cantilevers

Tap300 Al-G monolithic silicon cantilevers plated with a thin layer of aluminum was used in an order reflecting light from the deflection sensor in the AFM equipment (Fig. 31). These cantilevers are characterized by its tip allows for the more symmetric representation of high sample features.

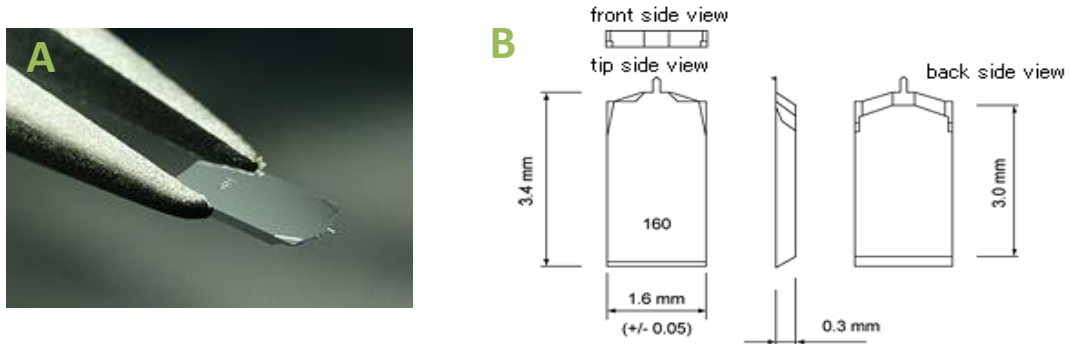


Figure 2-6: The Tap300 Al-G monolithic silicon cantilevers. Image (A) shows of the AFM cantilever and chip. While the image (B), shows approximate values for most of the standard silicon AFM probes available from Nano-science Instruments.

2.2.3.3 AFM measurements

The measurements were carried out under clean conditions at room temperature, and AFM imaging was performed under ambient conditions with a scanning frequency of 1 Hz. The image resolution was set to 1280 x 1280 pixels for overview images ($5 \times 5 \mu\text{m}^2$) whereas smaller regions were scanned with a resolution of 512x 512 pixels to ensure a high degree of reproducibility of experiment data.

2.2.4 Structural analysis

The Gwyddion software package (version 2.4.2) was used to process and analyze original images, while the software package Easyworm (Joerg Gsponer Lab, University of British Columbia, Vancouver, Canada) was used in the structural analysis of single xanthan molecules. Both software packages are distributed freely. Initially, we flattened the native data and corrected for error lines as well as the assessment the height of single xanthan strands using Gwyddion. We estimated the height of a single strand by averaging the height estimated from at least five cross-sections. To estimate the mean height of one kind, we estimated the overall mean of one sample. Eventually, the images were exported as bitmap data to be used for further analysis with Easyworm. Using a model Worm-Like-Chain-Model for semi-flexible polymers, the contour length and bending stiffness, which are considered as general properties of the polymer (Teraoka 2002), were described. Here, we used the Easyworm software package to estimate and calculate these values. Certainly, the bending stiffness is determined by the decay length of the tangent correlation function of the polymer chain.

$$\langle \vec{t}_s \cdot \vec{t}_{s'} \rangle = \exp\left(-\frac{|s - s'|}{L_p}\right)$$

Here, \vec{t}_s and $\vec{t}_{s'}$ are tangent vectors of the polymer backbone at positions s and s' , respectively. In the present study, we used the persistence length to measure the structural stiffness for single- or double-stranded polymers. Moreover, the contour length L_C is defined as the distance between the ends of the polymer. It can be evaluated as a product of all individual segments (n) and the length of an individual monomer (l) (Fixman&Kovac, 1973):

$$L_C = n \cdot l$$

2.2.5 Viscosity measurements

In order to measure the viscosity, dried xanthan was milled then; the powder was utilized to produce 1% (w/v) xanthan in distilled water (at least 60 min stirring was applied in order to dissolve the xanthan. The viscosimeter was used to measure the different viscosities over a variety of shear rates (Rheotec Rotational Viscosimeter,

Ottendorf-Okrilla, Germany). Depending on the use of viscosimeter, spindle shear rates could be calculated. These measurements were performed by Tim Steffens.

2.2.6 Statistics

The statistics software Spss to estimate and analyze the distributions of the polymer height, contour and persistence length was used. A Shapiro-Wilk test was applied to test each distribution for normality. Because not all experimental series showed a normal distribution, a non-parametric Mann-Whitney U-Test was carried out to test for significant differences in the distributions of the samples. The level of significance was set to $\alpha = 5\%$ by default.

2.3 Results and Discussion

2.3.1 Structure analysis of xanthan

For the structural analysis of single xanthan molecules, commercial xanthan was dissolved in deionized water (1 mg ml^{-1}) in a first step and has been shaken gently for at least 12 hours. In order to image single, well-separated molecules, the solution was diluted further ($2\text{-}5 \text{ }\mu\text{g ml}^{-1}$) and was shaken again for at least 12 hours. The main objective of these experiments is to study and compare individual xanthan molecules for each xanthan samples in their native state. Therefore, preheating of samples was not used to obtain individual xanthan molecules. Prior to AFM experiments, the optimum concentration was used to obtain single xanthan molecules and placed to freshly cleaved mica sheets, and dried with nitrogen gas. Statistical analysis did not give significant differences between B100 samples and wxcB samples. In contrast, significant differences were evident of all three measured parameters height, persistence and contour length when comparing B100 and wxcB samples with other samples (Table 2-2)

Table 2-2: Structural and viscosity data of all xanthan samples tested. For the pyruvate-free xanthan, only the polymers which could be clearly classified as single or double-stranded (n=8) are shown here. Stated is the mean value \pm standard deviation in nm for structural data as well as the viscosity in mPas. The countour length could only be estimated for linear xanthan strands

| | Height [nm] | Contour length [nm] | Persistence length [nm] | Viscosity [mPas] (*) |
|------------------------------|-----------------|---------------------|-------------------------|----------------------|
| B100 [n=30]** | 0.66 \pm 0.05 | NA | 38 \pm 10 | 46460 |
| B100 [n=25]*** | 0.58 \pm 0.6 | NA | 35 \pm 5 | 50110 |
| wxcB [n= 31]** | 0.64 \pm 0.1 | NA | 37 \pm 4 | 46460 |
| wxcB [n= 26]*** | 0.61 \pm 0.03 | NA | 36 \pm 7 | 50110 |
| JBL007 [n=15] | 0.30 \pm 0.01 | 2270 \pm 2148 | 34 \pm 3 | 15090 |
| Acetate-free [n=25] | 0.44 \pm 0.03 | 1635 \pm 1140 | 46 \pm 11 | 12300 |
| Pyruvate-free < 0.5 nm [n=3] | 0.31 \pm 0.02 | 620 \pm 384 | 39 \pm 4 | 97650 |
| Pyruvate-free > 0.5 nm [n=5] | 0.60 \pm 0.04 | NA | 82 \pm 19 | 97650 |

* At shear rate 0.17 s⁻¹

**B100 and wxcB precipitated by isopropanol

*** B100 and wxcB un-precipitated by isopropanol

2.3.1.1 Structures analysis of xanthan B100 and wxcB

Fig. 2-7 displays AFM images of single molecules of the xanthan produced by B100 and mutant wxcB in way fermentation methods(precipitated and un-precipitated by isopropanol) was as follows:

1. The wild type Xcc strain B100 (n = 30) (precipitated by isopropanol).
2. The wild type xanthan Xcc B100 (n= 25) (un-precipitated by isopropanol).
3. The mutant xanthan Xcc H21012 (wxcB) (n= 31) (precipitated by isopropanol).
4. The mutant xanthan Xcc H21012 (wxcB) (n= 26) (un-precipitated by isopropanol).

All images showed visible branching, giving them a star and tree-like structure (Fig. 2-7). The mean values of height of the B100 were (precipitated by isopropanol) $A = 0.66 \text{ nm} \pm 0.05$, while B100 (un-precipitated by isopropanol) was $B = 0.58 \text{ nm} \pm 0.6$ nm, on the other hand, the mean values of height of the wxcB (precipitated by isopropanol) was $C = 0.64 \text{ nm} \pm 0.1$ nm, while the mean values of height of the wxcB (un-precipitated by isopropanol) $D = 0.61 \text{ nm} \pm 0.03$ nm (Fig.2-8). This strongly suggests that they build a double-stranded secondary structure. When we performed a Mann–Whitney U analysis for the mean values of height, the yielded four did not show significant effects (Fig.2-9). Moreover, the persistence length was as $A = 38 \text{ nm} \pm 10$ nm, $B = 35 \text{ nm} \pm 0.5$ nm, $C = 37 \text{ nm} \pm 4.8$ nm, $D = 39 \text{ nm} \pm 0.4$ nm. Here, the distinct contour length is not possible to assess due to the extensive branching this samples. All the B100 and wxcB results are summarized in table 2-3.

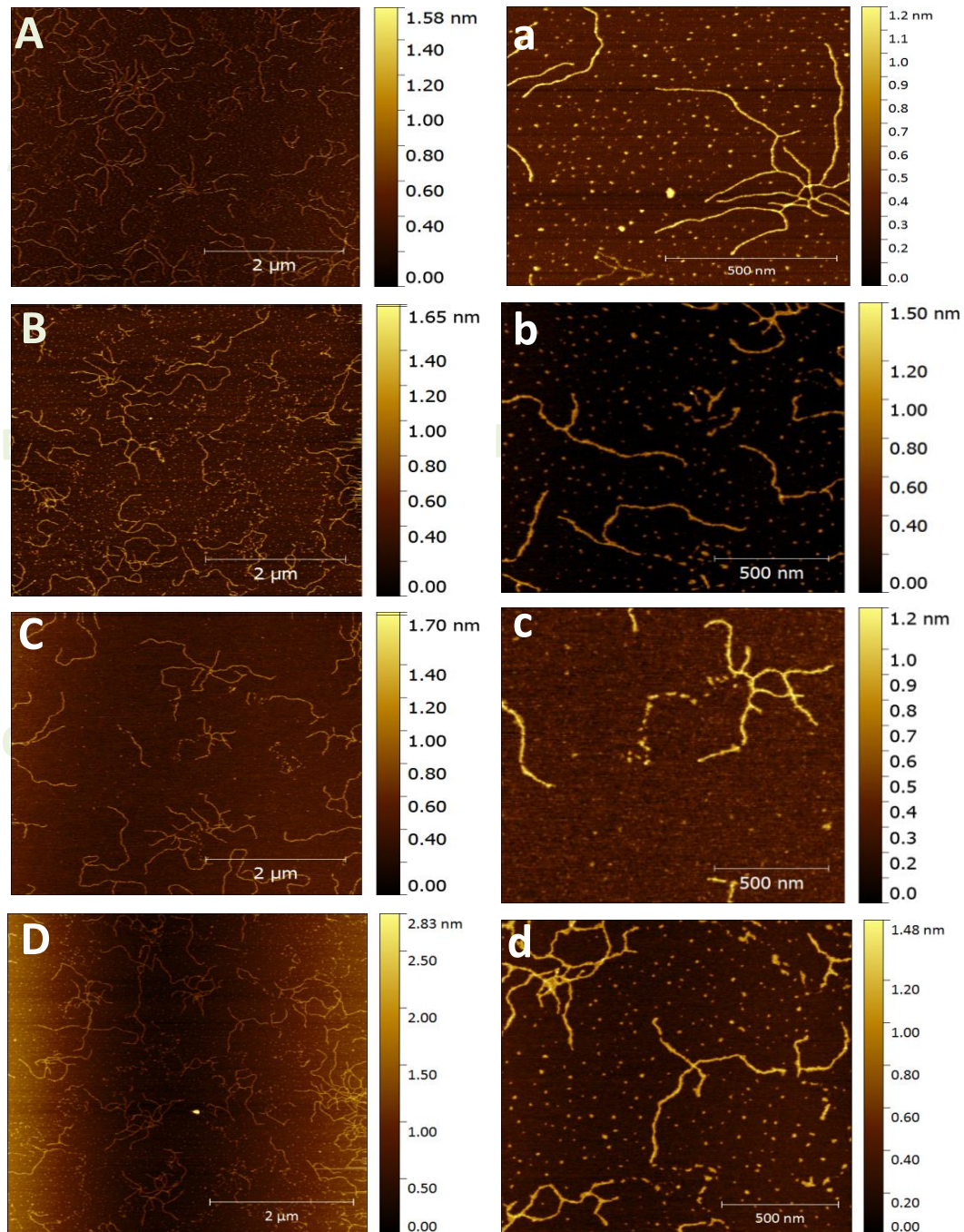


Figure 2-7: The AFM topography images show *Xanthomonas campestris pv. campestris* B100 and wxcB. Images A, B, C, and D give an overview of the samples, while a, b, c and d show a detailed structure of each sample: (A) represent the wild type of B100 (precipitated by isopropanol), and (B) represent the wild type of B100 (un-precipitated by isopropanol), while (C) represent the mutant wxcB (precipitated by isopropanol), and (D) represent the mutant wxcB (un-precipitated by isopropanol). The single molecules show visible branching and overlapping sections a, b, c and d.

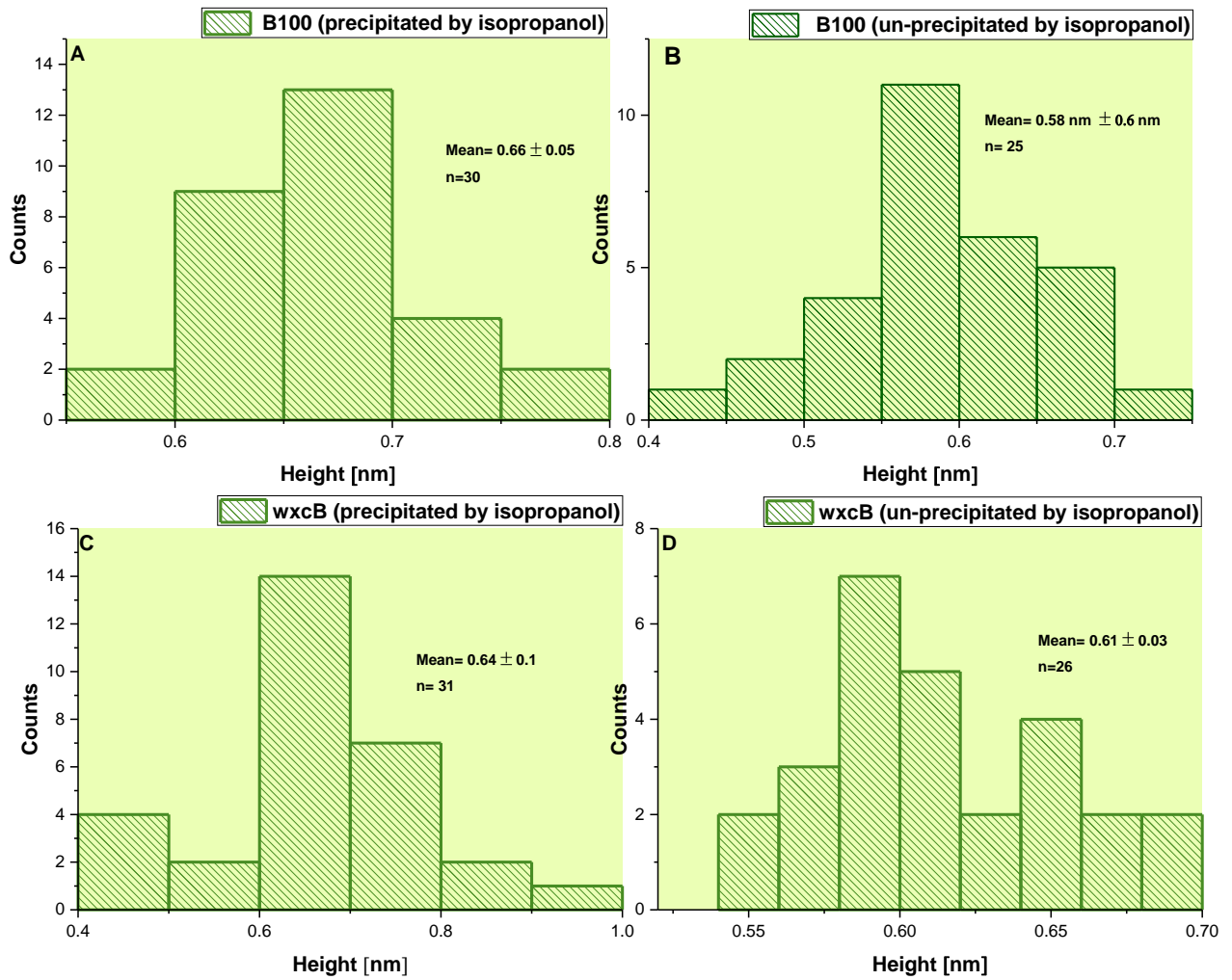


Figure 2-8: The histograms represent the mean values of height of the wild type B100 and the mutant type wxcB samples. A representative of the mean values of height of the B100 (precipitated by isopropanol) and B represent the mean values of height of the B100 (un-precipitated by isopropanol), while C represents the mean values of height of the mutant type wxcB (precipitated by isopropanol) and D represent the mean values of height of the mutant type wxcB (un-precipitated by isopropanol).

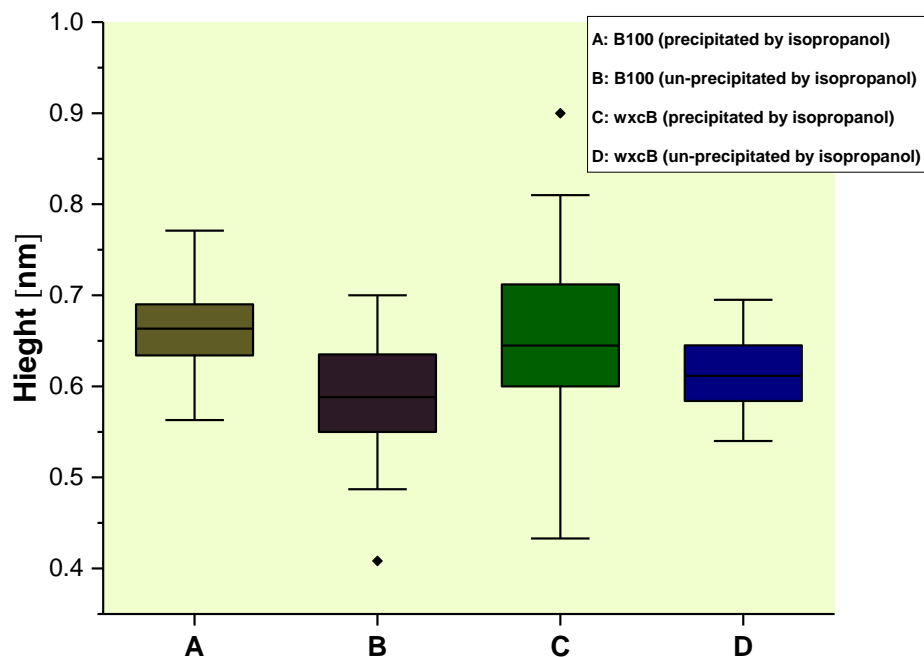


Figure 2-9: Box plot represents the mean values of height of the B100 and (A, B, C, D) samples. Results represent four independent experiments.

Table 2-3: Structural and viscosity data of B100 and wxcB samples, the show is the mean value \pm standard deviation in nm for structural data and also the viscosity in mPas.

| | Height [nm] | Contour length [nm] | Persistence length [nm] | Viscosity [mPas](*) |
|----------|-----------------------------------|---------------------|-------------------------------|---------------------|
| A | 0.66 ± 0.05 | NA | 38 ± 10 | 46460 |
| B | 0.58 ± 0.6 | NA | 35 ± 5 | 50110 |
| C | 0.64 ± 0.1 | NA | 37 ± 8 | 46460 |
| D | 0.61 ± 0.03 | NA | 39 ± 10 | 50110 |

* at a shear rate 0.17 s^{-1}

2.3.1.2 Structures analysis of xanthan JBL007

In contrast to the both Xcc B100 and wxcB samples that exhibited a double-stranded secondary structure. The AFM image of the production strain JBL007 exhibited no branching but sharp kinks (Fig 2-10), which is also reflected in the lower persistence length of $34 \text{ nm} \pm 3 \text{ nm}$. The lower persistence length and a height of only $0.30 \text{ nm} \pm 0.01 \text{ nm}$ (Fig. 2-11) can be attributed to the fact that the JBL007 strain exists only as a single-stranded structure without any distinct secondary structure. By applied

the Mann-Whitney U-Test, the mean height of the JBL007 strain revealed significant differences compared to the means height of the other samples (Table 2-4). Also, in comparison with the tested samples, JBL007 strain formed the longest polymers were estimated $2270 \text{ nm} \pm 2148 \text{ nm}$. However, there was great variability in the contour length. The longest molecule had a length of 7870 nm while the shortest was only 277 nm long.

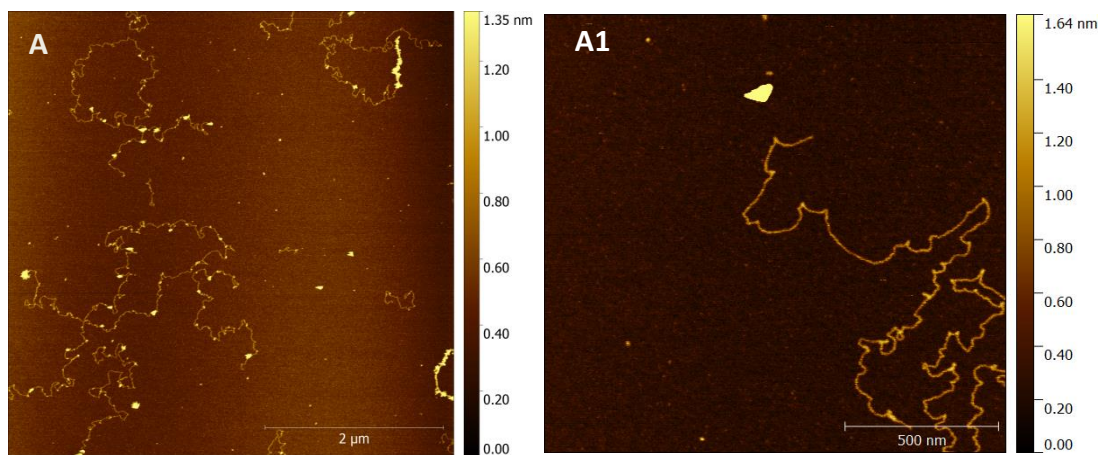


Figure 2-10: The AFM topography images show the production strain JBL007. Image (A) gives an overview of the sample, while (A1) shows a detailed structure of the sample. The polymers show no branching. These images were done by Julia Teckentrup

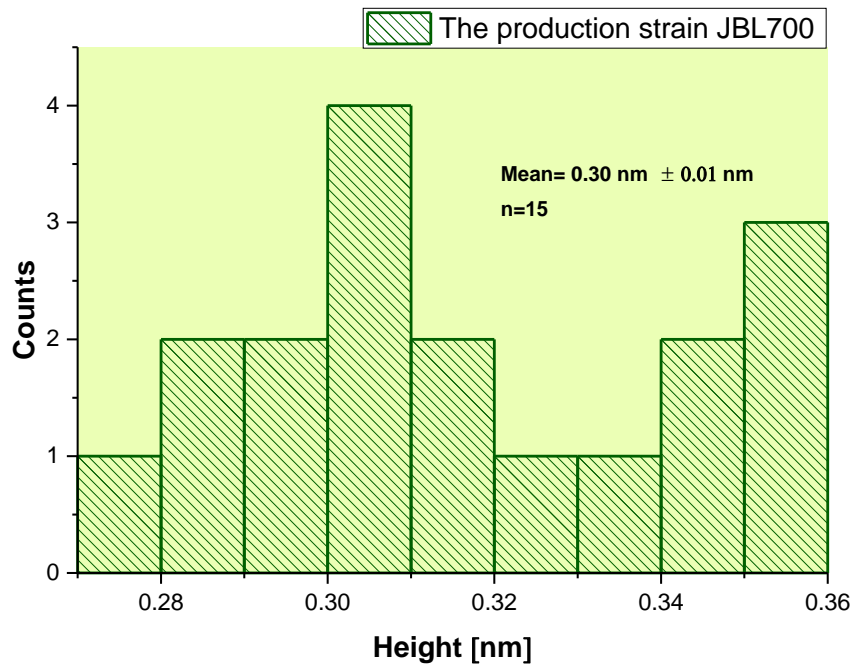


Figure 2-11: The histograms represent the mean values of height of the production strain JBL007.

Table 2-4: Calculated *p*-values of the Mann-Whitney U-Test for the distributions of the mean heights between JBL007 and other tested samples. ns, not significant

| Comparison | | <i>p</i> -value |
|------------|---|-----------------|
| 1 | JBL007 versus B100 (a) | $p < 0.001$ |
| 2 | JBL007 versus B100 (b) | $p < 0.001$ |
| 3 | JBL007 versus wxcB (c) | $p < 0.001$ |
| 4 | JBL007 versus wxcB (d) | $p < 0.001$ |
| 5 | JBL007 versus Acetate-free xanthan | $p < 0.001$ |
| 6 | JBL007 versus pyruvate-free xanthan > 0.5 nm | ns |
| 7 | JBL007 versus pyruvate-free xanthan < 0.5 nm | $p < 0.01$ |

2.3.1.3 Structure analysis of Acetate-free xanthan

The xanthan lacking acetate substitution exhibited no branching (Fig 2-12). In addition, the variation in the contour length can be observed, where the shortest polymer had a length of 304 nm whereas the longest was 4038 nm long: A contour length of $1635 \text{ nm} \pm 1140 \text{ nm}$ was evaluated for the acetate-free xanthan ($n = 25$). The mean height was $0.44 \text{ nm} \pm 0.03 \text{ nm}$ (Fig 2-13), and the sample showed a persistence length of $0.46 \text{ nm} \pm 6 \text{ nm}$. Here, the total means of the height and persistence length appear greater than it would be expected for a predominantly single-stranded system. This is due to the presence of very few polymers that display visibly higher and stiffer double-stranded regions. The mean of the height the acetate-free xanthan showed obviously significant differences compared to the means height of the other tested samples (Table 2-5).

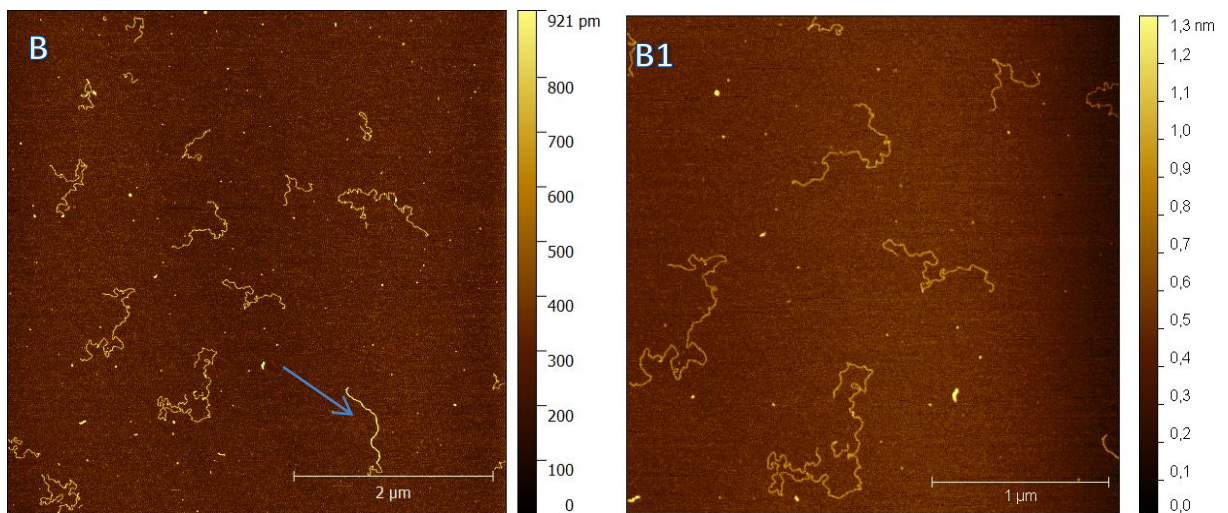


Figure 2-12: The AFM topography images show of the Acetate-free xanthan. Image (B) gives an overview of the sample, while (B1) shows a detailed structure of the sample. The polymers show no branching. The arrow points on the polymer double-stranded.

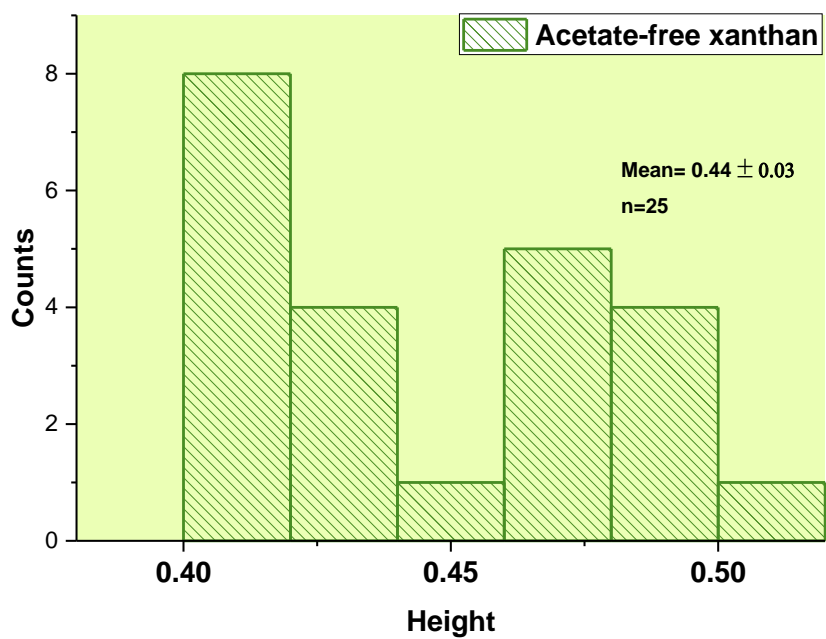


Figure 2-13: The histograms represent the mean values of height of the Acetate-free xanthan.

Table 2-5: Calculated p-values of the Mann-Whitney U-Test for the distributions of the mean heights between Acetate-free xanthan and tested samples. ns, not significant

| Comparison | | p-value |
|------------|--|-------------|
| 1 | Acetate-free xanthan versus B100 (a) | $p < 0.002$ |
| 2 | Acetate-free xanthan versus B100 (b) | $p < 0.001$ |
| 3 | Acetate-free xanthan versus wxcB (c) | $p < 0.001$ |
| 4 | Acetate-free xanthan versus wxcB (d) | $p < 0.001$ |
| 5 | Acetate-free xanthan versus JBL007 | $p < 0.001$ |
| 6 | Acetate-free xanthan versus pyruvate-free xanthan > 0.5 nm | ns |
| 7 | Acetate-free xanthan versus pyruvate-free xanthan < 0.5 nm | $p < 0.05$ |

2.3.1.4 Structure analysis of Pyruvate-free xanthan

In contrast to all of the samples that showed a fairly homogeneous structure, the pyruvate-free xanthan structure appeared as single ($n=3$) and doubled ($n=5$) strands at the same time. Nevertheless, in the most cases ($n=25$) the individual molecules exposed many spot-like structures (Fig. 2-14), which, in turn, may be attributed to local back folding, resulting in a series of loops along the backbone of the polymer. In this case, it is not possible to estimate the molecule height, contour and persistence length. This is due to the inability to classify them as to whether single or double-stranded. Fig. 2-14 C1 displays AFM images of the individual molecule of the pyruvate-free xanthan that exposed a homogeneous structure. It could be distinguished between polymers with a mean height of less than 0.5 nm ($n = 3$) and polymers with a mean height greater than 0.5 nm ($n = 5$) corresponding to single and double-stranded species. The individual molecule that classified as single-stranded molecules exposed the mean height of $0.31 \text{ nm} \pm 0.11 \text{ nm}$ and the persistence length of $38 \text{ nm} \pm 5 \text{ nm}$. While the double-stranded exposed height of $0.63 \text{ nm} \pm 0.13 \text{ nm}$ and a persistence length of $81 \text{ nm} \pm 17 \text{ nm}$. Clear variations of the persistence length can be distinguished between among the single and double-stranded molecule species (Fig. 2-14 C1). While double-stranded species are

stiffer, the single-stranded structures exhibit permanent bends or sharp kinks. In these experimental series, the shortest polymers were recorded the single-stranded molecules of the pyruvate-free xanthan with a contour length of only $620 \text{ nm} \pm 384 \text{ nm}$. Obviously, the bonds that the pyruvate xanthan create by means of ordered (double-strands) or unordered (local loops) back-folding leads to the high abundance of locally folded polymers. As a result, increased folded polymers might be an indicator of the missing charge plays a role in the binding probabilities of the molecules (Phillips and Williams 2009). We suppose that the side chains of the polymer that lose the negative charge weaken Coulomb repulsion. This, in turn, enhances the formation of a secondary structure. By using the Mann–Whitney U method, the mean height of the pyruvate-free xanthan showed significant differences when compared to other samples (Tables 2-6 and 2-7).

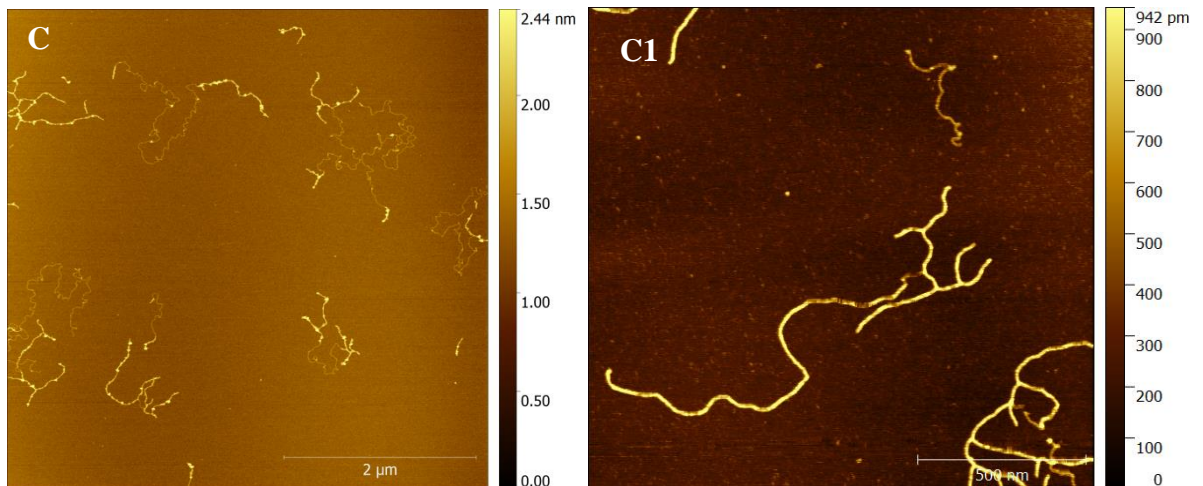


Figure 2-14. The AFM topography images show the Pyruvate-free xanthan. Image (C) gives an overview of the sample, while (C1) show a detailed structure of the sample. The polymer displays simultaneously single- and double-stranded areas, resulting in an inhomogeneous height. These images were done by Julia Teckentrup

Table 2-6: Calculated p-values of the Mann-Whitney U-Test for the distributions of the mean heights between pyruvate-free xanthan < 0.5 nm and other tested samples. ns, not significant

| Comparison | | p-value |
|------------|--|------------|
| 1 | pyruvate-free xanthan < 0.5 nm versus B100 (a) | $p < 0.02$ |
| 2 | pyruvate-free xanthan < 0.5 nm versus B100 (b) | $p < 0.01$ |
| 3 | pyruvate-free xanthan < 0.5 nm versus wxcB (c) | $p < 0.02$ |
| 4 | pyruvate-free xanthan < 0.5 nm versus wxcB (d) | $p < 0.02$ |
| 5 | pyruvate-free xanthan < 0.5 nm versus JBL007 | ns |
| 6 | pyruvate-free xanthan < 0.5 nm versus Acetate-free xanthan | ns |

Table 2-7: Calculated p-values of the Mann-Whitney U-Test for the distributions of the mean heights between pyruvate-free xanthan > 0.5 nm and other tested samples. ns, not significant

| Comparison | | p-value |
|------------|--|------------|
| 1 | pyruvate-free xanthan > 0.5 nm versus B100 (a) | ns |
| 2 | pyruvate-free xanthan > 0.5 nm versus B100 (b) | ns |
| 3 | pyruvate-free xanthan > 0.5 nm versus wxcB (c) | ns |
| 4 | pyruvate-free xanthan > 0.5 nm versus wxcB (d) | ns |
| 5 | pyruvate-free xanthan > 0.5 nm versus JBL007 | $p < 0.04$ |
| 6 | pyruvate-free xanthan > 0.5 nm versus Acetate-free xanthan | $p < 0.05$ |

2.3.2 Specificity of secondary structures

In this work, Mann–Whitney U analysis was used to analyse the specificity of the individual xanthan structures were analyzed by means of the molecule height, which showed set significant differences between tested samples (Fig. 2-15). It is well known that the xanthan secreted by different strains of bacteria can differ substantially. The wide structural diversity of the same product indicates that *Xantomonas* do not produce a uniform product with regard to their genetic composition or the culture conditions in which xanthan is produced. Indeed, The secondary structure of xanthan relies on proportions the acetate and pyruvate substitutes which put negative charge in the side chains of the polymer structure (Abbaszadeh et al. 2015). These side chains are closely related with the cellulosic backbone of xanthan, resulting in the rigid helical structure, which in turn contribute to the complex formation through interacts with other molecules (Moorhouse et al. 1977; Moffat et al. 2016). As stated before, acetate and pyruvate are added to the chain in non-stoichiometric amounts during the synthesis process (Teckentrup et al. 2017a); therefore, xanthan shows differing amounts of its non-sugar substituents. Undoubtedly, the dynamics building interloops within the chain may be created at places with a low ratio of charged substituents linked to the chain, due to which the chain is more mobile especially if it consists of a single-strand, thus stimulating the formation of points of high entanglement. This may explain the presence of the same local in most of the samples tested. Also, modification of charged substituents plays an important role in the conformation state of xanthan (Phillips and Williams 2009). For example, The missing pyruvate group in pyruvate-free xanthan promotes electrostatic interactions which are increase association to other parts of the molecule, resulting in the formation of double-strands and inter-loops structures (Abbaszadeh et al. 2015; Phillips and Williams 2009). On the contrary, the destabilizing effect of the acetate groups reduces electrostatic interactions between intermolecular, therefore leads to single formation strands and very few double-strands (Abbaszadeh et al. 2015).

With the AFM images, the molecular height measurements clearly confirmed that the tested xanthan samples reveal clear differences that led to the formation of single- as well as double-stranded molecules. All the double-stranded xanthan (B100 and wxCB) samples only exhibited the stiffer structure known for the ordered form of xanthan (Gulrez et al. 2012). In contrast, the single-stranded xanthan samples (JBL007, acetate-free and the flat polymers of the pyruvate-free xanthan) obviously exhibited the

disordered form known as ‘random coil’ structure, which characterizes by less stiff and occurs in very dilute solution with low ionic strength (Gulrez et al. 2012). Here, we can strongly suggest that the xanthan conformation state (ordered-disordered form) depends on the degree of acetate and pyruvate substitutes of the bacterial strains used, whether the bacterium has been genetically modified or subsequent chemical modification as well as fermentation conditions. These strains differ in their ability to change the degree of substitution of their exopolysaccharide in response to a change in environment or fermentation conditions (Abbaszadeh et al. 2015).

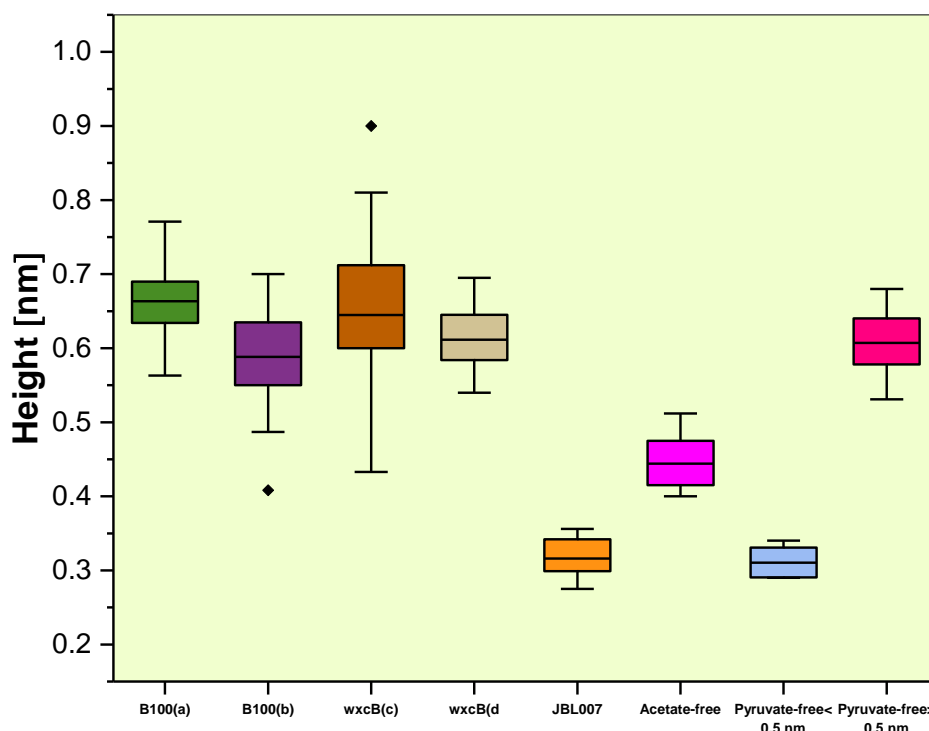


Figure 2-15: Boxplots of the measured heights (nm) of the different xanthan samples. The sample sizes were B100 (a. precipitated by isopropanol n= 30), B100 (b. un-precipitated by isopropanol n= 25), the mutant type wxcB (c. precipitated by isopropanol n= 31), the mutant type wxcB (d.un-precipitated by isopropanol n=26) JBL007 n = 15, acetate-free xanthan n= 25, pyruvate-free xanthan < 0.5 nm (n =3) and pyruvate-free xanthan > 0.5 nm (n =5).

2.3.3 Xanthan contour length distributions

In this study, the analyzed samples showed obvious differences in the structural features. Wild type B100, the mutant type wxcB, and certain extend pyruvate-free xanthan samples exposed extensive branching and back-folding, while the production strain and acetate-free xanthan exposed nicely traceable linear polymers. A non-

parametric Mann-Whitney U test yielded no significant differences were revealed in the distributions of the mean values of the contour length of the samples (all p-values > 0.05) (Fig.2-16). On the other hand, the width of the distributions of the different samples showed great differences compared to the mean values that did not show any significant differences. The large variation in polymers lengths is shown by the high values of standard deviations of the contour lengths. As anticipated, this may be due to a somewhat heterogeneous secretion process concerning the polymer length (van der Maarel 2008).

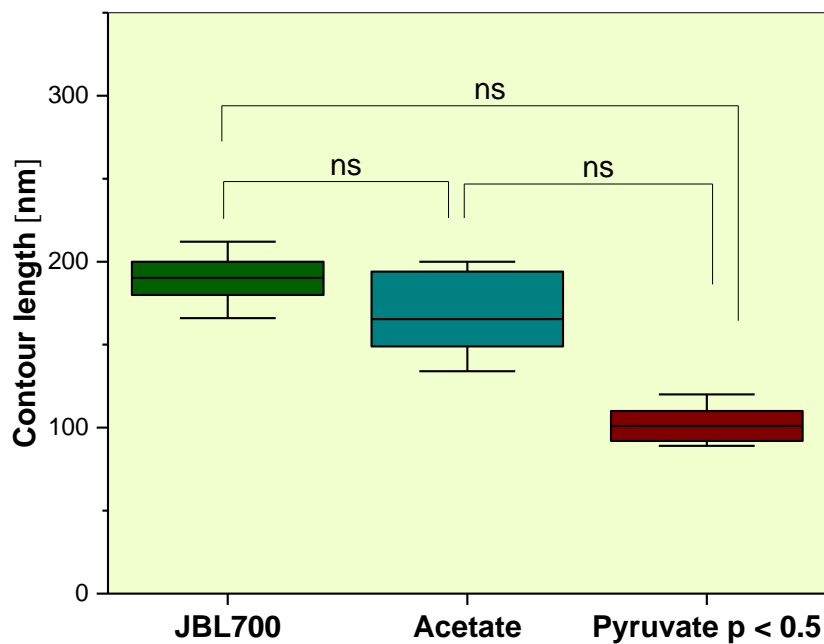


Figure 2-16: Boxplots of the measured contour lengths [nm] of the different xanthan samples.

2.3.4 Correlation between Viscosity Behavior and Structure

In order to determine the dynamic viscosity of xanthan dispensed in water, the aqueous xanthan solutions at shear rates ranging from 0.17 to 8.4 s⁻¹ were used. Just like xanthan structures, the shear-thickening potency showed a very clear contrast between the different kinds of xanthan (Table2-1). The lowest viscosity was recorded for acetate-free xanthan (12.300 mPas), while the pyruvate-free xanthan had the highest viscosity (97650 mPas). On the other hand, the wild-type B100 and the mutant type wxcB that produced by fermentation and shaken culture techniques revealed a high viscosity. The wild-type B100 and the mutant type wxcB that produced by fermentation was estimated 46 460 mPas as for, the wild-typeB100 and the mutant type wxcB that

produced by shaken culture technique were 50110 mPas. Interestingly, the viscosity of the commercially used production strain was lower than the wild type B100 (15090 mPas) and very close to the one of acetate-free xanthan. Actually, the variation in the viscosity of the aqueous solutions of xanthan produced by genetically and chemically modified strains of *X. campestris* rely on the details of inter- and intramolecular interactions (Smith and Pace 1982). This study results contradict with those obtained by Bradshaw et al. (1983) and Callet et al. (1987) who stated that the shear-thickening potency of xanthan is not affected by the degree of pyruvulation. However, the pyruvate residue was cut off after the excretion process in order to chemical modifies this xanthan species. Since there may be variation among properties of chemically modified xanthan and its native form, it is unknown if both xanthan types are identical. In contrast to our results, several studies reported that increasing pyruvate content, which is related to its mannose side-chain lead to an increase in viscosity rates (Sandford et al. 1977; Hassler and Doherty 1990). However, likewise with the work of Bradshaw and Callet the analyzed xanthan was not secreted by a mutant strain of *X. campestris* but was also chemically altered. Also, the salt concentration affects the viscosity; the increase of viscosity was observed at a high salt concentration in the dispensing medium. Here, this behavior may be due to the increase in shielding of the negative charges of the pyruvate groups, resulting in increased electrostatic interaction between inter- and intramolecular (Milas and Rinaudo 1986; Smith and Pace 1982). Obviously, xanthan production by genetically and chemically modified strains of *X. campestris* has a significant effect on the shear-thickening efficiency.

Our results suggest that the xanthan viscosity is attributing to the ability to form helical secondary structures and local inter-loops. The high viscosity of the wild type B100, the mutant type wxcB and pyruvate-free xanthan samples expose a wide range of different secondary structure motives such as a double-stranded structure and various kinds of local interloops. On the other hand, the low viscosity production strain xanthan JBL007 and acetate-free xanthan only expose single-stranded polymers. Thus, in order to improve the shear-thickening potency of xanthan, one can use a modification of the side chain of xanthan by introducing or removing charged residues. Moreover, Analysis of the 3D structure of the xanthan allows providing a glimpse of the macroscopic viscosity.

2.4 Conclusions

In this work, the molecular secondary structure and viscosity of xanthan, which natively secreted by several different *X. campestris* strains were analyzed. We could define the structural features for each product, which were ranging from flexible single-stranded polymers for the acetate free xanthan, pyruvate free xanthan, and JBL007 to stiff branched double-strands in the case the wild-type B100 and the mutant (wxcB) xanthan. Here, our results demonstrated that the viscosity is strongly related to the ability to build up a secondary molecular structure. Moreover, the analysis of the results has not revealed a significant correlation between the xanthan chain length and its viscosity. Indeed, the length distributions of natively secreted xanthan are rather broad. Subsequently, the apparent heterogeneity of the samples may mask the potential effect of the polymer chain length.

References

- **Abbaszadeh**, A.; Lad, M.; Janin, M.; Morris, G. A.; MacNaughtan, W.; Sworn, G.; Foster, T. J. (2015): A novel approach to the determination of the pyruvate and acetate distribution in xanthan. In *Food Hydrocolloids* 44, pp. 162–171. DOI: 10.1016/j.foodhyd.2014.08.014.
- **Alkhateeb**, Rabeaa S.; Vorhölter, Frank-Jörg; Steffens, Tim; Rückert, Christian; Ortseifen, Vera; Hublik, Gerd et al. (2018): Comparative transcription profiling of two fermentation cultures of *Xanthomonas campestris* pv. *Campestris* B100 sampled in the growth and in the stationary phase. In *Applied microbiology and biotechnology* 102 (15), pp. 6613–6625. DOI: 10.1007/s00253-018-9106-2.
- **Ashraf**, Simin; Soudi, Mohammad Reza; Ghadam, Parinaz (2017): Production of Xanthanases by *Paenibacillus* spp.: Complete Xanthan Degradation and Possible Applications. In *Iranian journal of biotechnology* 15 (2), pp. 120–127. DOI: 10.15171/ijb.1477.
- **Barreras**, Máximo; Abdian, Patricia L.; Ielpi, Luis (2004): Functional characterization of GumK, a membrane-associated beta-glucuronosyltransferase from *Xanthomonas campestris* required for xanthan polysaccharide synthesis. In *Glycobiology* 14 (3), pp. 233–241. DOI: 10.1093/glycob/cwh056.
- **Becker**, A.; Katzen, F.; Pühler, A.; Ielpi, L. (1998): Xanthan gum biosynthesis and application: a biochemical/genetic perspective. In *Applied microbiology and biotechnology* 50 (2), pp. 145–152. DOI: 10.1007/s002530051269.
- **Becker**, Anke (2015): Challenges and perspectives in combinatorial assembly of novel exopolysaccharide biosynthesis pathways. In *Frontiers in microbiology* 6, p. 687. DOI: 10.3389/fmicb.2015.00687.
- **Bueno**, Vânia Blasques; Petri, Denise Freitas Siqueira (2014): Xanthan hydrogel films: molecular conformation, charge density and protein carriers. In *Carbohydrate Polymers* 101, pp. 897–904. DOI: 10.1016/j.carbpol.2013.10.039.
- **Conforte**, Valeria P.; Yaryura, Pablo M.; Bianco, María I.; Rodríguez, María C.; Daglio, Yasmin; Prieto, Eduardo et al. (2019): Changes in the physico-chemical properties of the xanthan produced by *Xanthomonas citri* subsp. *citri* in

- grapefruit leaf extract. In *Glycobiology* 29 (3), pp. 269–278. DOI: 10.1093/glycob/cwy114.
- **Dai**, Xiaohui; Gao, Ge; Wu, Mengmeng; Wei, Weiyang; Qu, Jianmei; Li, Guoqiang; Ma, Ting (2019): Construction and application of a *Xanthomonas campestris* CGMCC15155 strain that produces white xanthan gum. In *MicrobiologyOpen* 8 (2), e00631. DOI: 10.1002/mbo3.631.
 - **Dário**, Aline F.; Hortêncio, Lucas M.A.; Sierakowski, Maria Rita; Neto, João C. Queiroz; Petri, Denise F.S. (2011): The effect of calcium salts on the viscosity and adsorption behavior of xanthan. In *Carbohydrate Polymers* 84 (1), pp. 669–676. DOI: 10.1016/j.carbpol.2010.12.047.
 - **Donot**, F.; Fontana, A.; Baccou, J. C.; Schorr-Galindo, S. (2012): Microbial exopolysaccharides: Main examples of synthesis, excretion, genetics and extraction. In *Carbohydrate Polymers* 87 (2), pp. 951–962. DOI: 10.1016/j.carbpol.2011.08.083.
 - **Douglas**, Timothy E. L.; Schietse, Josefien; Zima, Aneta; Gorodzha, Svetlana; Parakhonskiy, Bogdan V.; KhaleNkow, Dmitry et al. (2018): Novel self-gelling injectable hydrogel/alpha-tricalcium phosphate composites for bone regeneration: Physiochemical and microcomputer tomographical characterization. In *Journal of biomedical materials research. Part A* 106 (3), pp. 822–828. DOI: 10.1002/jbm.a.36277.
 - **Fagioli**, Laura; Pavoni, Lucia; Logrippo, Serena; Pelucchini, Caroline; Rampoldi, Luca; Cespi, Marco et al. (2019): Linear Viscoelastic Properties of Selected Polysaccharide Gums as Function of Concentration, pH, and Temperature. In *Journal of food science* 84 (1), pp. 65–72. DOI: 10.1111/1750-3841.14407.
 - **Fiume**, Monice M.; Heldreth, Bart; Bergfeld, Wilma F.; Belsito, Donald V.; Hill, Ronald A.; Klaassen, Curtis D. et al. (2016): Safety Assessment of Microbial Polysaccharide Gums as Used in Cosmetics. In *International journal of toxicology* 35 (1 Suppl), 5S-49S. DOI: 10.1177/1091581816651606.
 - **Freitas**, Filomena; Alves, Vitor D.; Reis, Maria A. M. (2011): Advances in bacterial exopolysaccharides: from production to biotechnological applications.

- In *Trends in biotechnology* 29 (8), pp. 388–398. DOI: 10.1016/j.tibtech.2011.03.008.
- **Galván**, Zoila Rosa Nieto; Soares, Lucas de Souza; Medeiros, Eber Antonio Alves; Soares, Nilda de Fátima Ferreira; Ramos, Afonso Mota; Coimbra, Jane Sélia dos Reis; Oliveira, Eduardo Basílio de (2018): Rheological Properties of Aqueous Dispersions of Xanthan Gum Containing Different Chloride Salts Are Impacted by both Sizes and Net Electric Charges of the Cations. In *Food Biophysics* 13 (2), pp. 186–197. DOI: 10.1007/s11483-018-9524-9.
 - **García-Ochoa**, F.; Santos, V.E; Casas, J.A; Gómez, E. (2000): Xanthan gum: production, recovery, and properties. In *Biotechnology Advances* 18 (7), pp. 549–579. DOI: 10.1016/S0734-9750(00)00050-1.
 - **Goff**, H. Douglas; Guo, Qingbin (2019): Chapter 1. The Role of Hydrocolloids in the Development of Food Structure. In Fotios Spyropoulos, Aris Lazidis, Ian T. Norton (Eds.): *Handbook of food structure development*. 1st. Cambridge: Royal Society of Chemistry (Food Chemistry, Function and Analysis, v. 18), pp. 1–28.
 - **Gulrez**, Syed K.H.; Al-Assaf, Saphwan; Fang, Yapeng; Phillips, Glyn O.; Gunning, A. Patrick (2012): Revisiting the conformation of xanthan and the effect of industrially relevant treatments. In *Carbohydrate Polymers* 90 (3), pp. 1235–1243. DOI: 10.1016/j.carbpol.2012.06.055.
 - **Guo**, Mark Q.; Hu, Xinzhong; Wang, Changlu; Ai, Lianzhong (2017): Polysaccharides: Structure and Solubility. In Zhenbo Xu (Ed.): *Solubility of Polysaccharides*: InTech.
 - **Habibi**, Hossein; Khosravi-Darani, Kianoush (2017): Effective variables on production and structure of xanthan gum and its food applications: A review. In *Biocatalysis and Agricultural Biotechnology* 10, pp. 130–140. DOI: 10.1016/j.bcab.2017.02.013.
 - **Hager**, Fiona F.; Sützl, Leander; Stefanović, Cordula; Blaukopf, Markus; Schäffer, Christina (2019): Pyruvate Substitutions on Glycoconjugates. In *International Journal of Molecular Sciences* 20 (19). DOI: 10.3390/ijms20194929.

- **Hu**, Xiaolong; Wang, Kangli; Yu, Miao; He, Peixin; Qiao, Hanzhen; Zhang, Huiru; Wang, Zichao (2019): Characterization and Antioxidant Activity of a Low-Molecular-Weight Xanthan Gum. In *Biomolecules* 9 (11). DOI: 10.3390/biom9110730.
- **Islam**, Salim T.; Lam, Joseph S. (2013): Wzx flippase-mediated membrane translocation of sugar polymer precursors in bacteria. In *Environmental microbiology* 15 (4), pp. 1001–1015. DOI: 10.1111/j.1462-2920.2012.02890.x.
- **Jansson**, Per-erik; Kenne, Lennart; Lindberg, Bengt (1975): Structure of the extracellular polysaccharide from xanthomonas campestris. In *Carbohydrate Research* 45 (1), pp. 275–282. DOI: 10.1016/S0008-6215(00)85885-1.
- **KANG**, K. S.; **PETTITT**, D. J. (2012): XANTHAN, GELLAN, WELAN, AND RHAMSAN. In Roy L. Whistler, James N. BeMiller (Eds.): Industrial gums. Polysaccharides and their derivatives / edited by Roy L. Whistler, James N. BeMiller. Third edition. San Diego: Academic Press, pp. 341–397.
- **Katzen**, F.; Ferreiro, D. U.; Oddo, C. G.; Ielmini, M. V.; Becker, A.; Pühler, A.; Ielpi, L. (1998): Xanthomonas campestris pv. campestris gum mutants: effects on xanthan biosynthesis and plant virulence. In *Journal of Bacteriology* 180 (7), pp. 1607–1617.
- **Kool**, Marijn M.; Schols, Henk A.; Delahaije, Roy J. B. M.; Sworn, Graham; Wierenga, Peter A.; Gruppen, Harry (2013): The influence of the primary and secondary xanthan structure on the enzymatic hydrolysis of the xanthan backbone. In *Carbohydrate Polymers* 97 (2), pp. 368–375. DOI: 10.1016/j.carbpol.2013.05.045.
- **Kreyenschulte**, Dirk; Krull, Rainer; Margaritis, Argyrios (2014): Recent advances in microbial biopolymer production and purification. In *Critical reviews in biotechnology* 34 (1), pp. 1–15. DOI: 10.3109/07388551.2012.743501.
- **Leroy**, Frédéric; Vuyst, Luc de (2016): Advances in production and simplified methods for recovery and quantification of exopolysaccharides for applications in food and health. In *Journal of dairy science* 99 (4), pp. 3229–3238. DOI: 10.3168/jds.2015-9936.

- **Li**, Ruoshi; Feke, Donald L. (2015): Rheological and kinetic study of the ultrasonic degradation of xanthan gum in aqueous solution: effects of pyruvate group. In *Carbohydrate Polymers* 124, pp. 216–221. DOI: 10.1016/j.carbpol.2015.02.018.
- **Luvielmo**, Márcia de Mello; Borges, Caroline Dellinghausen; Toyama, Daniela de Oliveira; Vendruscolo, Claire Tondo; Scamparini, Adilma Regina Pippa (2016): Structure of xanthan gum and cell ultrastructure at different times of alkali stress. In *Brazilian journal of microbiology : [publication of the Brazilian Society for Microbiology]* 47 (1), pp. 102–109. DOI: 10.1016/j.bjm.2015.11.006.
- **Margaritis**, Argyrios; Zajic, James E. (1978): Mixing, mass transfer, and scale-up of polysaccharide fermentations. In *Biotechnol. Bioeng.* 20 (7), pp. 939–1001. DOI: 10.1002/bit.260200702.
- **Meddeb**, Zina; Hajjem, Hatem; Mabrouk, Aicha; Jeday, M. Razak (2015): A New Industrial Hydrogen Production Process. In *GSC* 05 (04), pp. 145–153. DOI: 10.4236/gsc.2015.54018.
- **Miao**, Tianxin; Wang, Junqing; Zeng, Yun; Liu, Gang; Chen, Xiaoyuan (2018): Polysaccharide-Based Controlled Release Systems for Therapeutics Delivery and Tissue Engineering: From Bench to Bedside. In *Advanced science (Weinheim, Baden-Wurtemberg, Germany)* 5 (4), p. 1700513. DOI: 10.1002/advs.201700513.
- **Milas**, Michel; Rinaudo, Marguerite (1986): Properties of xanthan gum in aqueous solutions: Role of the conformational transition. In *Carbohydrate Research* 158, pp. 191–204. DOI: 10.1016/0008-6215(86)84017-4.
- **Moffat**, Jonathan; Morris, Victor J.; Al-Assaf, Saphwan; Gunning, A. Patrick (2016): Visualisation of xanthan conformation by atomic force microscopy. In *Carbohydrate Polymers* 148, pp. 380–389. DOI: 10.1016/j.carbpol.2016.04.078.
- **Mohammadinejad**, Reza; Kumar, Anuj; Ranjbar-Mohammadi, Marziyeh; Ashrafizadeh, Milad; Han, Sung Soo; Khang, Gilson; Roveimiab, Ziba (2020): Recent Advances in Natural Gum-Based Biomaterials for Tissue Engineering and Regenerative Medicine: A Review. In *Polymers* 12 (1). DOI: 10.3390/polym12010176.

- **Mohammed**, Z. H.; Haque, A.; Richardson, R. K.; Morris, E. R. (2007): Promotion and inhibition of xanthan ‘weak-gel’ rheology by calcium ions. In *Carbohydrate Polymers* 70 (1), pp. 38–45. DOI: 10.1016/j.carbpol.2007.02.026.
- **MOORHOUSE**, R.; WALKINSHAW, M. D.; ARNOTT, S. (1977): Xanthan Gum—Molecular Conformation and Interactions. In Paul Sandford, Allen I. Laskin (Eds.): Extracellular microbial polysaccharides. A symposium sponsored by the Division of Carbohydrate Chemistry and the Division of Microbial and Biochemical Technology at the 172nd Meeting of the American Chemical Society, San Francisco, Calif., August 30-31, 1976 / Paul A.Sandford, Allen Laskin, editors, vol. 45. Washington, D.C.: AMERICAN CHEMICAL SOCIETY (ACS Symposium Series, 45), pp. 90–102.
- **P. Bharali**, P. Mudoj (2013): Study on the Effect of pH, Temperature and Aeration on the Cellular Growth and Xanthan Production by *Xanthomonas campestris* Using Waste Residual Molasses. In *J Bioprocess Biotechniq* 03 (03). DOI: 10.4172/2155-9821.1000135.
- **Palaniraj**, Aarthy; Jayaraman, Vijayakumar (2011a): Production, recovery and applications of xanthan gum by *Xanthomonas campestris*. In *Journal of Food Engineering* 106 (1), pp. 1–12. DOI: 10.1016/j.jfoodeng.2011.03.035.
- **Palaniraj**, Aarthy; Jayaraman, Vijayakumar (2011b): Production, recovery and applications of xanthan gum by *Xanthomonas campestris*. In *Journal of Food Engineering* 106 (1), pp. 1–12. DOI: 10.1016/j.jfoodeng.2011.03.035.
- **Petri**, Denise F. S. (2015): Xanthan gum: A versatile biopolymer for biomedical and technological applications. In *J. Appl. Polym. Sci.* 132 (23), n/a-n/a. DOI: 10.1002/app.42035.
- **Phillips**, Glyn O.; Williams, Peter A. (2009): Handbook of hydrocolloids. 2nd ed. Boca Raton, Fla.: CRC; Oxford : Woodhead Publishing Ltd (Woodhead Publishing in food science, technology and nutrition).
- **Rinaudo**, M.; Moroni, A. (2009): Rheological behavior of binary and ternary mixtures of polysaccharides in aqueous medium. In *Food Hydrocolloids* 23 (7), pp. 1720–1728. DOI: 10.1016/j.foodhyd.2009.01.012.

- **Rodriguez-R**, Luis M.; Grajales, Alejandro; Arrieta-Ortiz, Mario L.; Salazar, Camilo; Restrepo, Silvia; Bernal, Adriana (2012): Genomes-based phylogeny of the genus *Xanthomonas*. In *BMC microbiology* 12, p. 43. DOI: 10.1186/1471-2180-12-43.
- **Rosalam**, S.; England, R. (2006): Review of xanthan gum production from unmodified starches by *Xanthomonas campestris* sp. In *Enzyme and Microbial Technology* 39 (2), pp. 197–207. DOI: 10.1016/j.enzmictec.2005.10.019.
- **Ross-Murphy**, Simon B.; Wang, Qi; Ellis, Peter R. (1998): Structure and mechanical properties of polysaccharides. In *Macromol. Symp.* 127 (1), pp. 13–21. DOI: 10.1002/masy.19981270105.
- **Ryan**, Robert P.; Vorhölter, Frank-Jörg; Potnis, Neha; Jones, Jeffrey B.; van Sluys, Marie-Anne; Bogdanove, Adam J.; Dow, J. Maxwell (2011): Pathogenomics of *Xanthomonas*: understanding bacterium-plant interactions. In *Nature reviews. Microbiology* 9 (5), pp. 344–355. DOI: 10.1038/nrmicro2558.
- **Schatschneider**, Sarah; Huber, Claudia; Neuweger, Heiko; Watt, Tony Francis; Pühler, Alfred; Eisenreich, Wolfgang et al. (2014): Metabolic flux pattern of glucose utilization by *Xanthomonas campestris* pv. *campestris*: prevalent role of the Entner-Doudoroff pathway and minor fluxes through the pentose phosphate pathway and glycolysis. In *Molecular bioSystems* 10 (10), pp. 2663–2676. DOI: 10.1039/c4mb00198b.
- **Schatschneider**, Sarah; Persicke, Marcus; Watt, Steven Alexander; Hublik, Gerd; Pühler, Alfred; Niehaus, Karsten; Vorhölter, Frank-Jörg (2013): Establishment, in silico analysis, and experimental verification of a large-scale metabolic network of the xanthan producing *Xanthomonas campestris* pv. *campestris* strain B100. In *Journal of biotechnology* 167 (2), pp. 123–134. DOI: 10.1016/j.jbiotec.2013.01.023.
- **Shatwell**, Karolyn P.; Sutherland, Ian W.; Dea, Iain C.M.; Ross-Murphy, Simon B. (1990): The influence of acetyl and pyruvate substituents on the helix-coil transition behaviour of xanthan. In *Carbohydrate Research* 206 (1), pp. 87–103. DOI: 10.1016/0008-6215(90)84009-J.

- **Smith**, Ian H.; Pace, Gary W. (1982): Recovery of microbial polysaccharides. In *J. Chem. Technol. Biotechnol.* 32 (1), pp. 119–129. DOI: 10.1002/jctb.5030320116.
- **Soleymanpour**, Zahra; Nikzad, Maryam; Talebnia, Farid; Niknezhad, Vahid (2018): Xanthan gum production from acid hydrolyzed broomcorn stem as a sole carbon source by *Xanthomonas campestris*. In *3 Biotech* 8 (7), p. 296. DOI: 10.1007/s13205-018-1322-z.
- **Song**, Zhigang; Zhang, Yan; Shao, Huarong; Ying, Yong; Chen, Xiang'e; Mei, Li et al. (2019): Effect of xanthan gum on the prevention of intra-abdominal adhesion in rats. In *International journal of biological macromolecules* 126, pp. 531–538. DOI: 10.1016/j.ijbiomac.2018.12.233.
- **Steffens**, Tim; Vorhölter, Frank-Jörg; Giampà, Marco; Hublik, Gerd; Pühler, Alfred; Niehaus, Karsten (2016): The influence of a modified lipopolysaccharide O-antigen on the biosynthesis of xanthan in *Xanthomonas campestris* pv. *campestris* B100. In *BMC microbiology* 16, p. 93. DOI: 10.1186/s12866-016-0710-y.
- **Stokke**, Bjørn Torger; Christensen, Bjørn Erik (1996): Release of disordered xanthan oligomers upon partial acid hydrolysis of double-stranded xanthan. In *Food Hydrocolloids* 10 (1), pp. 83–89. DOI: 10.1016/S0268-005X(96)80058-0.
- **Sutherland**, Ian W. (2001-2003): Polysaccharides from Microorganisms, Plants and Animals. In A. Steinbüchel, S. Matsumura, M. Hofrichter, T. Koyama, E. J. Vandamme, S. de Baets, S. R. Fahnestock (Eds.): *Biopolymers. Biology, chemistry, biotechnology, applications: Lignin, humic substances and coal*. Weinheim: Wiley-VCH.
- **Teckentrup**, Julia; Al-Hammood, Orooba; Steffens, Tim; Bednarz, Hanna; Walhorn, Volker; Niehaus, Karsten; Anselmetti, Dario (2017a): Comparative analysis of different xanthan samples by atomic force microscopy. In *Journal of biotechnology* 257, pp. 2–8. DOI: 10.1016/j.jbiotec.2016.11.032.
- **Teckentrup**, Julia; Al-Hammood, Orooba; Steffens, Tim; Bednarz, Hanna; Walhorn, Volker; Niehaus, Karsten; Anselmetti, Dario (2017b): Comparative analysis of different xanthan samples by atomic force microscopy. In *Journal of biotechnology* 257, pp. 2–8. DOI: 10.1016/j.jbiotec.2016.11.032.

- **Van der Maarel**, Johan R. C. (2008): Introduction to biopolymer physics. Hackensack N.J.: WORLD SCIENTIFIC.
- **Vorhölter**, Frank-Jörg; Schneiker, Susanne; Goesmann, Alexander; Krause, Lutz; Bekel, Thomas; Kaiser, Olaf et al. (2008): The genome of *Xanthomonas campestris pv. campestris* B100 and its use for the reconstruction of metabolic pathways involved in xanthan biosynthesis. In *Journal of biotechnology* 134 (1-2), pp. 33–45. DOI: 10.1016/j.jbiotec.2007.12.013.
- **Yang**, Fan; Li, He; Sun, Jie; Guo, Xiaoyu; Zhang, Xinyu; Tao, Min et al. (2019): Novel Endotype Xanthanase from Xanthan-Degrading Microbacterium sp. Strain XT11. In *Applied and environmental microbiology* 85 (2). DOI: 10.1128/AEM.01800-18.
- **Zhou**, Weibiao; Hui, Y. H. (2014): Bakery products science and technology. Second edition. Chichester West Sussex UK: John Wiley & Sons Inc. Available online at <http://gbv.ebib.com/patron/FullRecord.aspx?p=1708801>.

Curriculum Vita

1. Personal information

First name: Orooba Nadhim Harbi

Last name: AL-Hammood

Sex: Female

Date of Birth: 14/04/1975

Place of Birth: Baghdad – Iraq

Nationality: Iraqi

Email: Orooba_alhammood@yahoo.com

2. Certificate

Oct. 1982-Jun. 1987 Primary school (Lebanon pri. school) Baghdad-Iraq

Oct. 1987-Jun. 1992 Secondary school (Al-Huda sec. school) Baghdad-Iraq

Oct. 1993-Jun. 1997 BSc in Microbiology from Department of Biology- College of Science, Al-Mustansiriya University – Iraq

Oct. 2006-Feb. 2010 MSc in Biotechnology from Department of Biotechnology- College of Science, Al-Nahrain University – Iraq

3. PhD studies

Since April 2015, PhD student in department Experimental Biophysics and Applied Nanoscience, (Pro. Dr Dario Anselmetti), faculty of physics, Bielefeld University, Germany

4. Publication

Teckentrup, Julia; Al-Hammood, Orooba; Steffens, Tim; Bednarz, Hanna; Walhorn, Volker; Niehaus, Karsten; Anselmetti, Dario (2017): Comparative analysis of different xanthan samples by atomic force microscopy. In *Journal of biotechnology* 257, pp. 2–8. DOI: 10.1016/j.jbiotec.2016.11.032.

5. Conferences

a. Poster presentation:

Julia Teckentrup, Orooba Al-Hammood, Tim Steffen, Hanna Bednarz, Volker Walhorn, Karsten Niehaus, and Dario Anselmetti (Exploring the secondary structure of xanthan by atomic force microscopy), DPG- Jahrestagung Meeting, 7th March 2016 Regensburg, Germany.

b. Poster presentation:

Julia Teckentrup, Orooba Al-Hammood, Tim Steffen, Hanna Bednarz, Volker Walhorn, Karsten Niehaus, and Dario Anselmetti (Exploring the secondary structure of xanthan by atomic force microscopy), NRW Nano-Conference Meeting, 7th December 2016 Münster, Germany.